The Dissertation Committee for Michael Mayes Robinson Certifies that this is the approved version of the following dissertation:

Applications of Micro-3D Printing to Microfluidic Cell Dosing

Committee:

Jason B. Shear, Supervisor

Adela Ben-Yakar

Richard M. Crooks

Xiaojing John Zhang

Vernita Gordon

Applications of Micro-3D Printing to Microfluidic Cell Dosing

by

Michael Mayes Robinson, B.S.; M.S.E.

Dissertation

Presented to the Faculty of the Graduate School of

The University of Texas at Austin

in Partial Fulfillment

of the Requirements

for the Degree of

Doctor of Philosophy

The University of Texas at Austin

August 2014

Dedication

This dissertation is dedicated to my wife, Shelli.

Acknowledgements

I would like to thank my advisor, Dr. Jason Shear, for his continued support and an unrestrictive environment for creative growth. I am also grateful to my committee members, Dr. Adela Ben-Yakar, Dr. Richard Crooks, Dr. John Zhang, and Dr. Vernita Gordon. I additionally would like to thank all current and former Shear Lab members. Dr. Samira Moorjani and Dr. Todd Hoppe patiently provided an introduction to microfluidics and cell culture. Dr. Eric Ritschdorff and Dr. Jodi Connell were kind enough to demonstrate multiphoton fabrication techniques and allow me access to delicate equipment that they always repaired after I finished experimenting. Dr. Eric Spivey answered an endless stream of questions and provided critical fabrication software and advice. I owe much gratitude for Maryam Ali for building and maintaining a multiphoton fabrication system and Derek Hernandez for Schwann cell supplies and advice. I thank Janine Elliott, Mindy Fitzpatrick, and Allison Myers for their positive energy, enthusiasm, and lip-syncing skills. I am grateful for Allison Meyers and Dr. Todd Hoppe for carefully editing and proofreading this dissertation. I thank Sarah Stuart, Kevin Eckes, Richard Hennessey, and many Austin and DC friends for their years of friendship and advice. My sincerest gratitude goes to my parents, family, and wife, whose patience and sacrifices can never be repaid.

Applications of Micro-3D Printing to Microfluidic Cell Dosing

Michael Mayes Robinson, PhD.

The University of Texas at Austin, 2014

Supervisor: Jason B. Shear

Cellular growth, development, differentiation, and death are mediated to some degree by the interaction of soluble factors with plasma membrane receptors. Traditionally the cellular response to chemical cues has been studied by exposing entire culture dishes to a desired reagent. While the addition of soluble reagents homogenously to cell culture dishes provides a basis for understanding much of cell biology, greater spatial resolution of reagent delivery is necessary in order to elucidate mechanisms on the subcellular scale. This dissertation explores techniques that may improve the quality and precision of delivering soluble factors to cultured cells in order to better understand the complex processes of cell biology. These advancements were made possible by applying high intensity, focused laser light to soluble materials to achieve microscopic three-dimensional (μ-3D) printing. In combination with a previously developed microfluidic cell dosing platform, microstructures were designed and μ-3D printed to hydrodynamically focus reagent streams for cell dosing. Structures were also μ-3D printed within micrometers of living cells from a solution of gelatin and bovine serum albumin with minimal cytotoxicity. When μ-3D printed, these proteins displayed both temperature and pH-responsive properties. In order to allow for on-the-fly control of reagent stream size and temporal pulse width, microstructures were μ-3D printed from temperature-responsive N-isoproplyacrylamide. To further improve the temporal

resolution of the system, a technique for cycling between reagents with millisecond exchange times using laminar flow microfluidics was developed. The utility of these techniques was demonstrated by staining rat Schwann cells and mouse neuroblastoma rat glioma hybrid cells (NG108-15) with focused streams of fluorescent dyes. These advancements may allow future experiments to determine the placement of soluble factors necessary for bacterial quorum sensing or stem cell differentiation.

Table of Contents

List of Figures

Chapter 1: Introduction

In the summer of 1675 Antonie van Leeuwenhoek created a microscope capable of detecting living organisms "no more than the 30th of an inch in diameter [1]." Though he had no formal education past the age of 16, his success in creating high magnification microscopes allowed him to become the first person to describe microorganisms, spermatozoa, and the vacuole of the cell [2]. Since Leeuwenhoek's time, major breakthroughs in the understanding of cell biology have often relied upon new techniques such as the electron microscope [3] and DNA sequencing [4]. It can be assumed that many questions of cell biology lurk beneath the surface waiting to be revealed with currently unimagined techniques. Without novel and more exacting tools, the biologist will never know the delicate precision of life cultivated at his fingertips yet beyond his grasp.

To date, biologists have discerned that cells respond to their environment and to signals sent by other cells via sensitive receptors. Cellular growth, development, differentiation, and death are mediated to some degree by the interaction of external cues with these plasma membrane receptors [5]. These cues, and their corresponding highly specialized receptors, come in the form of mechanical [6], topographical [7], electrical [8] and chemical signals. Furthermore, the same signaling molecule, such as acetylcholine, can have vastly different effects when received by a heart pacemaker cell, salivary gland cell, or skeletal muscle cell [5].

Critically, these chemically mediated processes are widely conserved in biology, with local microgradients of soluble factors interpreted by intracellular transduction pathways resulting in profound changes to cell motility [9], axonal pathfinding [10], immune response [11], and stem cell differentiation [12]. Traditionally, cellular responses

to chemical cues are studied by exposing entire culture dishes to the desired reagent. However, this method is not capable of fully mimicking the *in vivo* environment where gradients of soluble factors on the nanometer to micrometer scale result in profound changes to axonal guidance [10] and neutrophil migration [13]. This dissertation explores techniques that may improve the quality and precision of delivering soluble factors to cultured cells in order to better elucidate the complex processes of cell biology.

1.1 Laminar Flow Microfluidics

Microfluidics refers to any process for displacing fluid with a channel diameter less than 1 mm or fluid volume less than 1 mL, and the term has been applied generously to a wide variety of devices. The field of microfluidics has continued to capture advancements in miniaturization and photolithography brought about by the microprocessor industry since the 1970s [14]. The growth of microelectromechanical systems (MEMS) was born from the realization that microfabrication techniques used for silicon computer chips could be applied to mechanical sensors and transducers [15]. Another breakthrough was the work of Andreas Manz in 1990, demonstrating that microfluidic devices could be used to separate biological molecules [16]. Critically, Manz showed that techniques commonly used for detection of proteins in human blood could be scaled down so as to reduce sample volume and reagent usage without sacrificing detection limits. Furthermore, the separations could be done faster and in parallel, compared to traditional slower, single sample HPLC equipment [17].

Microfluidic technology has since allowed researchers to reduce sample volumes down to picoliter volumes in order to study single cells for performing PCR [18] or directed evolution studies [19] without cross contaminating samples. Others have put considerable effort into creating lab-on-a-chip devices that consist of an assembly of

miniaturized valves, pumps [20], and channels to direct samples for separation and analytical techniques [21][22]. Using these methods, a lab bench worth of equipment can be reduced to the size of a coin (~1 cm^2) [23].

Intriguingly, the physics of fluid flow at the micron scale cannot be assumed equivalent to that at larger scales. For example, if a capillary tube has a small enough inner diameter, the surface tension for a drop of water is greater outside the tube and the drop will climb the walls of the capillary tube to reduce its free energy [24]. However, this effect does not scale linearly with the diameter of the capillary and the water drop will flow due to gravitational forces if the capillary diameter is above a critical size.

Similarly, in a microfluidic device, viscous forces dominate and inertial forces can be assumed irrelevant. This if often referred to as low Reynolds number flow or laminar flow. Reynolds number (Eq. 1.1) is a dimensionless ratio of inertial to viscous force where ρ is defined as the liquid density, v is fluid velocity, L is the channel width, and μ is the fluid viscosity.

$$Re = \frac{\rho v L}{\mu} \qquad \text{(Eq. 1.1)}$$

Thus, in a microfluidic device with a very low Reynolds number mixing of two parallel flowing streams does not occur due to eddies or convective currents and relies solely on diffusion of chemical species [14]. The Peclet number (Eq. 1.2) is a dimensionless measure of the convective versus diffusive transport such that larger Peclet numbers are favorable for reducing diffusive broadening of a laminar stream under convective flow [25]. The Peclet number is calculated as the ratio of the channel width (L) and fluid velocity (v) to the diffusion coefficient of a species of interest (D).

$$Pe = \frac{Lv}{D} \qquad \text{(Eq. 1.2)}$$

1.1.1 Sheath Flow

Sheath flow, also referred to as hydrodynamic focusing, describes the fluid dynamics phenomenon that occurs when a laminar stream is constrained in its size by surrounding laminar streams. The effect of the outside (sheath) streams is to constrain the cross sectional area of the inside (sample) stream without disturbing laminar flow in the system. Sheath flow has been used to create narrow sample streams for analyte detection since the 1940's [26]. The width of the sample stream can be tightly controlled in a sheath cuvette by adjusting the ratio of volumetric flow rates of the sample and sheath streams such that a sample stream of 1 μm can be achieved [27]. Sheath flow has been used extensively in a range of microfluidic applications including photofabrication of microfibers [28], multiphase fabrication of metal wires [29], cell sorting [30], and various forms of flow cytometry [31].

A theoretical model for sheath flow can be created from a simplified 2D flow chamber with three inlets and a single outlet channel (Figure 1.1). Assuming that all streams are laminar, the fluids are Newtonian, and all fluids have equal densities and viscosities, a mass balance can be created so that the volumetric flow into the system (Q_i + $2Q_s$) and out of the system (Q_o) are equal. Additionally, the volumetric flow in the focused stream (Q_f) is equal to the inlet stream (Q_i). The velocity of the exit channel (v_o) is equal to the sum of all inlet flows (Q_i + $2Q_s$) divided by the height of the channel (h) multiplied by the width (w_o) of the channel (Eq. 1.3).

$$\bar{v}_o = \frac{2Q_s + Q_i}{w_o \times h} \qquad \text{(Eq. 1.3)}$$

The width of the focused stream can then be related to the width of the channel by Eq. 1.4. In order to maximize the focusing effect, the sample flow rate (Q_i) should be reduced or the sheath flow rate(Q_s) increased.

$$\frac{w_f}{w_o} = \frac{Q_i}{\frac{\bar{v}_f}{\bar{v}_o}(2Q_s + Q_i)} \qquad \text{(Eq. 1.4)}$$

For lab-on-a-chip applications, the sheath flow geometry is often planar with twin sheath streams on each side of a sample stream [32][31]. However, 3D sheath flow on a chip has been reported using techniques that make use of a third sheath stream above the plane of the sample stream [33]. In this way the stream is focused on both sides and from above in order to minimize the stream size in three dimensions. Alternatively, the sample can be injected in a flowing channel above the surface of the channel [34], or a chimney can be fabricated to delivery flow from a reservoir [35]. Using these methods the bulk flow in channel acts as a sheath flow stream around the chimney to reduce the stream width.

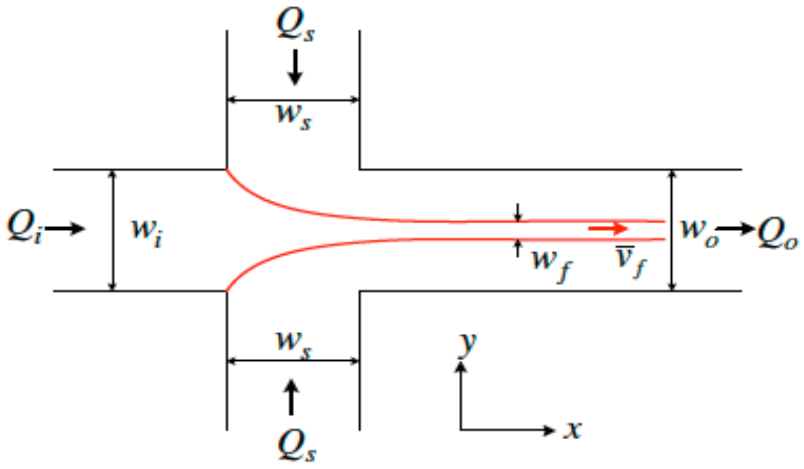

Figure 1.1: Illustration of a 2D symmetric sheath flow device. Q_i represents the volumetric flow from an inlet containing a sample species while perpendicular volumetric flow is given as Q_s. The width of the sample stream (w_f) is restricted by sheath flow (Q_s). Due to the incompressibility of the fluid and the conservation of mass, the velocity of the sample stream ($\overline{v_f}$) increases when sheath flow rates increase.

1.1.2 Applications of Microfluidics to Cell Dosing

Microfluidic devices allow the control of fluids on the scale of cell biology, 1-100 μm in length for most experiments. To properly study membrane receptors, sub-cellular resolution is required. That is, the stream of reagent must be more narrow than the cell at the point of dosing so that the cell's receptors experience minimal and maximal concentration values depending on their location. Due to the low Reynolds number (Re $\approx$ 0.1-100) and high Peclet number (Pe $>$ 10) flow of microfluidics, the laminar streams of reagents create sharp boundaries useful for subcellular dosing [36].

Specifically, the Whitesides flow chamber technique exploits these properties to achieve subcellular dosing resolution, albeit only along the boundary between two

laminar reagent streams orthogonal to flow [37][38]. To accomplish this, a microfluidic device was created with three inlets and one outlet port, allowing for control over the interfacial laminar flow boundary by means of variation in relative inlet flow rate. Subcellular resolution can be achieved in regard to the interfacial boundary, while reagent flow streams are generally confined to larger regions [38]. However, this technique does not allow for multiple parallel streams to be added after the device has been fabricated in order to target dynamic cellular processes. Additionally, the apparatus allows control over only one interfacial boundary, and thus only a single cell may be dosed at a single location during any period.

To date some progress has been made in establishing long lasting 3D gradients of soluble factors [39]. Using protein-loaded microsphere embedded in a hydrogel network, the release of reagents can be controlled in three dimensions and temporally. However, microsphere release techniques function on the scale of millimeters in length and do not allow for either rapid prototyping or *in situ* placement. Often these 3D gradients are created within hydrogel networks to encourage tissue formation on the scale of centimeters and over a period of days or weeks [40].

1.2 Finite Element Method

Engineers and scientists have long sought a method to simulate physical experiments in order to save time, reduce cost, and avoid potentially hazardous experimental conditions. Differential equations can describe an individual physical phenomenon but complex geometries and material properties result in problems with no closed form or exact solution [41]. For these problems, finite element methods (FEM) have become a popular tool for simulating a complex system and estimating a likely outcome for given initial conditions.

Many contributed to the development of finite element methods, including Olgierd Zienkiewicz, whose early work included a 1947 article modeling stress in gravity dams [42] and later a widely cited book detailing finite element methods for a range of engineering applications [43]. With the introduction of computers capable of executing complex algorithms, Zienkiewicz and others demonstrated that computational models could be used both for academic research and design of everyday objects. While originally developed for structural mechanics, FEM is now applied to fields including electrostatics [44], magnetics [45], heat transfer [46] and fluid dynamics [47].

Generally, FEM divides a complex problem into many sub-problems. The solutions to the sub-problems are integrated to obtain an estimate for the entire system. Typically a finite element model is created by dividing the system into many small triangles, known collectively as a mesh. Increasing the number of elements reduces the error introduced by a poorly fit model but also increases the computational time required to solve the model [41].

In the case of fluid dynamics models, the Navier-Stokes equation (Eq. 1.5) is used to estimate the fluid flow and pressure at each element by solving partial differential equations for each element's interfaces.

$$\rho\left(\frac{\partial \mathrm{v}}{\partial \mathrm{t}} + \mathrm{v}\cdot\nabla\mathrm{v}\right) = -\nabla\mathrm{p} + \mu\nabla^2\mathrm{v} \qquad \text{(Eq. 1.5)}$$

The equation requires knowledge of the density (ρ) and viscosity (μ) of the fluid. The velocity (v) or pressure (p) must be known at each boundary element at the initial time (t), or a steady state value can be assumed. Also, the same model can be used to simulate the diffusion and convection of chemical species from the previously solved velocity field assuming the conservation of mass equation [48]. The model simulates

diffusion using Fick's Law of Diffusion where the diffusion flux (J) is equal to the diffusion coefficient for the species in a given medium (D) and the partial derivatives of concentration (c) across spatial coordinates (Eq. 1.6).

$$J = -D\,\nabla c \qquad \text{(Eq. 1.6)}$$

1.3 MICROFABRICATION TECHNIQUES

1.3.1 Photolithography

Microfabrication techniques have been developed in the microelectronics industry to create complex electronic circuits with minimum feature sizes currently as small as 7 nm [49]. Techniques for creating the insulating or conducting features include physical vapor deposition, chemical vapor deposition, sputter coating, molecular beam epitaxy, and chemical beam epitaxy [50]. However, an integrated circuit is created using conductive areas of the device reserved for depositing resistors by a process known as photolithography.

The ability of photolithography to reliably create complex geometric patterns with small feature sizes has made it popular with researchers in microfluidics and lab-on-a-chip applications [51]. Photolithography is commonly performed using a material that is sensitive to light and a mask that specifies where the light is able to strike the material. Using conventional techniques, the minimum feature size that can be created is limited by the diffraction limit of light (Eq. 1.7).

$$d = \frac{\lambda}{2n\sin\theta} \qquad \text{(Eq. 1.7)}$$

The diffraction limit (d) is governed by the wavelength of light (λ) used, the index of refraction (n) and the half-angle of the light cone focusing upon a spot (θ). For these reasons ultraviolet (UV) light (248 nm) is commonly used with a photoresist material that responds to UV light to create features as small at 70 nm. A positive photoresist becomes soluble where it has been exposed to light, while a negative photoresist becomes insoluble where it has been exposed to light. After exposure to a light source filtered by a mask, the device is typically heated and treated with solvents to remove soluble photoresist and develop a hardened product [50].

For microfluidic applications, a variation known as soft photolithography is often used. The hardened product of standard photolithography is used as a master and elastomeric poly(dimethyl-siloxane) (PDMS) is poured over the master and cured resulting in a mold. The channels within the PDMS mold are used to direct the flow of reagents, where the width of the channel is determined by the photo-mask and the height of the channel is determined by the thickness of photoresist remaining on the master. PDMS is often chosen for chemical and biological experiments due to its low cost, high oxygen permeability, fast curing time, hydrophobicity, and low toxicity [52]. PDMS will form a water-tight seal to clean glass, allowing its use with high magnification inverted microscope objectives corrected for glass coverslips. In addition, PDMS forms a water-tight seal with other materials including polyimide and Mylar films when bound with a clamp [53]. However, while soft photolithography produces a product that is non-toxic, the fabrication process requires cytotoxic photoresists, solvents, and UV. Furthermore, most designs are limited to two-dimensional (2D) geometries; and three-dimensional (3D) control of features is generally limited to time consuming layer-by-layer methods that require realignment of photomasks between each layer [54].

1.3.2 Multiphoton Lithography (μ-3D Printing)

A molecule can be excited from an electronic ground state (E_o) to an electronic excited state (E_1) by the absorption of light. The energy imparted to the molecule by the photon of light can be lost due to nonradiative relaxation, fluorescence, or phosphorescence [55]. Because the energy of a photon is directly proportional to its frequency, the energy gap between E_o and E_1 can be crossed with two or more lower frequency photons in place of a single photon of higher frequency. This process is known as multiphoton excitation (MPE) and was first achieved in 1961 by Wolfgang Kaiser using a ruby laser [56]. Although it was theorized that MPE was possible before this time, no source of monochromatic light with high enough intensity to achieve MPE was available until the introduction of lasers in the 1960's.

The rate of excitation is described in Equation 1.8, where the intensity of the radiative source (I) must be increased exponentially (where n = 2 for two-photon excitation) for a given excitation cross-section (δ) to achieve promotion to an excited state. Due to the low probability of two photons being absorbed by a molecule nearly simultaneously, only molecules within the focal volume of a focused laser light source will experience MPE.

$$\frac{d[E_1]}{dt} = \delta I^n [E_0] \qquad \text{(Eq. 1.8)}$$

This unique property can be exploited for acquisition of 3D resolved multiphoton fluorescence images [57]. Because the MPE is confined to the focal volume of a focused laser, very low out-of-plane excitation occurs. The 3D isolation of excited molecules can be applied to photochemical reactions for fabrication of microstructures from a range of materials with both additive [58] and subtractive fabrication techniques [53].

The Shear group has demonstrated multiphoton lithography, referred to here as μ-3D printing, of hydrogel microstructures from biocompatible materials such as bovine serum albumin (BSA) and avidin [59]. Using photosensitizers that produce free radicals when excited using MPE, protein solutions can form cross-linked hydrogels with 3D resolution. Using a femtosecond pulsed laser and nano-positioning system, 3D objects with submicron resolution can be produced within seconds, allowing rapid prototyping of objects [60][61].

Additionally, this technique can be accomplished within the presence of living cells and the precursor solution washed away without inhibiting growth and survival of the cultured cells. For example, neuronal development has been guided by growth lanes, barriers, and pinning structures with multiphoton lithography [62]. However, Type I photosensitizers such as flavin adenine dinucleotide (FAD) were used in place of Type II photosensitizers that generate singlet oxygen ($^1O_2$) including Rose Bengal, methylene blue and eosin. Type I photosensitization occurs via excitation of the photosensitizer molecule to a triplet state capable of generating free radicals through hydrogen abstraction of an oxidizable species [63]. Type I photosensitizers have significantly lower cross linking efficiency and require either higher laser power or longer dwell times than Type II photosensitizers and are not suitable for creating complex 3D structures [64]. Type II photosensitizers are less useful with cultured cells due to lethal doses of singlet oxygen generated during μ-3D printing. However, recent work by Todd Hoppe has shown that when conjugated to protein molecules, Type II photosensitizers may be used without apparent toxic effects on mammalian cells.

1.3.3 Laser Ablation

Lasers light focused on a surface can be used to remove material through a process known as laser ablation. The mechanism of ablation depends on the timescale of the laser pulses. Longer pulse lasers ($\tau > 10$ ps) produce a heat-affected zone (HAZ) at the surface of the material where the laser light is focused. The size of the HAZ increases with the time scale of the laser pulse and the thermal diffusion coefficient of the material. Melting and vaporization of the material can occur on the order of nanoseconds and result in explosive ejection of material from the surface which may condense on the surface surrounding the ablation site [50].

Short-pulse lasers ($\tau < 10$ ps) generally do not create melting and the ablation is controlled by non-thermal processes [65]. In this case the material is transformed into plasma or otherwise ejected from the surface before heat can be generated or spread outside the focused laser spot. For example, glass has been shown to breakdown due to avalanche ionization when energized by focused femtosecond laser light [66].

The beam of a focused laser is often modeled using a Gaussian approximation. Although the spatial intensity of a focused optical system is best described by a point spread function, a Gaussian distribution is a close approximation commonly used with focused laser sources in TEM_{00} mode [67]. For a diffraction-limited Gaussian focus the beam waist (w_o) can be estimated from equation 1.9.

$$w_o = 0.61 \frac{\lambda}{NA} \qquad \text{(Eq. 1.9)}$$

The wavelength of the focused light (λ) and the numerical aperture of the objective (NA) are used to determine the beam waist. For a pulsed laser, the peak power (P_o) is determined from the average power (P_{avg}) measured at the back aperture of the objective,

the transmittance of the objective at the given wavelength (φ), the laser pulse width (τ), and the pulse repetition rate (ω) (Eq. 1.10).

$$P_o = \frac{P_{avg}\varphi}{\tau\omega} \qquad \text{(Eq. 1.10)}$$

The peak intensity is estimated assuming that the laser intensity profile consists of a square pulse lasting the entire duration of the pulse width. Thus, the peak intensity (I_o) can be found by dividing the peak power by the beam waist area (Eq. 1.11). To account for a Gaussian distribution spatially, the intensity is multiplied by a factor of 2 to obtain the peak intensity, both spatially and temporally.

$$I_o = \frac{2P_o}{w_o^2\pi} \qquad \text{(Eq. 1.11)}$$

For μ-3D printing a Ti:Sapphire laser is used with a peak intensity calculated to be 1.3 TW/cm^2 assuming a Gaussian focus with a 1.4 NA objective, 740 nm laser light, 80% objective transmittance, 150 fs pulse width, 76 MHz cycle, and 30 mW measured at the back aperture of the objective. This intensity was calculated from a beam waist of 322 nm and peak power of 2.6 kW assuming a Gaussian profile.

Rex Nielson, a former member of the Shear group, developed a microfluidic system using laser ablation within a flow chamber [53] that is the basis of the work detailed in this dissertation. The device consists of two flow chambers mated to each side of a thin impermeable polymer film such that one flow chamber serves as a reservoir for any desired dosing reagent, while the opposing flow cell serves as a cell culture chamber. A frequency-doubled (532 nm) Nd:YAG laser with a pulse width of ~600 ps and

repetition rate of 7.65 kHz is used to ablate pores 3-5 μm in diameter in a thin polymer film via a microscope objective. This process creates a stream of reagent from one chamber into another. The stream width varies between 15 and 45 μm depending on the flow rates in each chamber, the pressure in each chamber, and the size and shape of the pore created.

Although the Nd:YAG has a much longer pulse width than the Ti:Saphhire, the peak powers are similar at 3.3 kW and 2.6 kW, respectively. Using a 0.75 NA objective, the Nd:YAG delivers 8.9 TW/cm^2 with only 15 mW average power measured at the back aperture of the objective. Todd Hoppe determined that successful pore ablation and stream creation is achieved more frequently when the objective is under-filled by the laser [68]. Under-filling the objective results in a non-diffraction limited focus, spreading the laser power over a greater area of the ablation zone.

Because the pulse width of the Nd:YAG laser is longer than 10 ps it can be assumed that electrons transfer to the lattice structure of the substrate during the course of the pulse with enough time to create a heat affected zone. At the same time, significant ionization may occur in the gas or liquid adjacent to the surface of the polymer film via impact ionization due to electron ejections from the polymer surface [69]. Furthermore, scanning electron micrograph (SEM) images depict polymer material around the ablation site that appears to have melted and solidified, suggesting some thermal component to the ablation process (see Chapter 2).

1.4 Overview of the Chapters

The following chapters describe techniques to improve the quality and precision of delivering soluble factors to cultured cells. All of the techniques are designed and tested to be applied in concert with a microfluidic cell dosing system created by Rex

Nielson and refined by Samira Moorjani and Todd Hoppe (past members of the Shear group). This dissertation focuses primarily on improvements afforded by the application of μ-3D printing and finite element modeling to the cell dosing platform.

The first technique described (Chapter 2) describes a strategy for reducing the dosing stream width and controlling the three-dimensional (3D) profile of a reagent while dosing a cultured cell. These goals were achieved by developing a novel method of μ-3D printing within the microfluidic flow platform. Optimization of the printed structure geometries using finite element modeling is discussed along with analysis of stream width and cell dosing experiments.

Chapter 3 expands on the applications of μ-3D printing within a microfluidic system to include *it situ* μ-3D printing without deleterious effects on cultured cells. To minimize the toxicity of the photolithography steps on living cells, photoinitiator conjugation chemistries are evaluated and analyzed. Cell viability experiments with possible printing reagents are discussed in order to inform the applications of the technique. Finally, the results of long-term viability experiments after printing *in situ* are discussed.

Materials capable of swelling in response to environmental changes are evaluated for μ-3D printing applications in Chapter 4. Proteins and NIPPAm are assessed for thermal swelling characteristic at temperatures amenable to cellular life. Formulations optimal for μ-3D printing within a microfluidic system are judged using confocal microscopy. The geometry of a microfluidic valve is discussed, as well as the results of flow testing. The chapter also examines the application of pH-responsive μ-3D printed structures to the control of dosing streams. Structures were printed within the microfluidic system and actuated by changes in pH by application of solutions of

differing pH values. The results of these experiments and applications to cell culture are discussed.

The final chapter (Chapter 5) focuses on a technique to improve the temporal resolution of the dosing system. Neurons respond to changes in neurotransmitter concentration on the order of milliseconds and techniques are needed to reproduce these chemical cues *in vitro*. The technique discussed in Chapter 5 relies on the ability of two laminar flow streams to run parallel at low Reynolds number without mixing. The design and testing of this motorized, computer-controlled system for reagent switching is analyzed.

1.5 REFERENCES

1. Hogg, J. *The microscope: its history, construction, and applications*. (Illustrated London Library, 1854).
2. Dobell, C. *Antony van Leeuwenhoek and his 'Little animals'; being some account of the father of protozoology and bacteriology and his multifarious discoveries in these disciplines*. (Harcourt, Brace and company, 1932).
3. Huxley, H. E. Electron microscope studies on the structure of natural and synthetic protein filaments from striated muscle. *Journal of Molecular Biology* **7**, 281–IN30 (1963).
4. Wallace, D. C. Mitochondrial DNA sequence variation in human evolution and disease. *Proceedings of the National Academy of Sciences* **91**, 8739–8746 (1994).
5. Alberts, B. *et al*. *Essential Cell Biology, Fourth Edition*. (Garland Science, 2013).
6. Ingber, D. E. Mechanical signaling and the cellular response to extracellular matrix in angiogenesis and cardiovascular physiology. *Circulation Research* **91**, 877–887 (2002).
7. Boyan, B. D., Hummert, T. W., Dean, D. D. & Schwartz, Z. Role of material surfaces in regulating bone and cartilage cell response. *Biomaterials* **17**, 137–146 (1996).

8. Sun, S., Titushkin, I. & Cho, M. Regulation of mesenchymal stem cell adhesion and orientation in 3D collagen scaffold by electrical stimulus. *Bioelectrochemistry* **69**, 133–141 (2006).

9. Weiner, O. D. *et al*. Spatial control of actin polymerization during neutrophil chemotaxis. *Nature Cell Biology* **1**, 75–81 (1999).

10. Atkinson-Leadbeater, K. *et al*. Dynamic expression of axon guidance cues required for optic tract development is controlled by fibroblast growth factor signaling. *Journal of Neuroscience* **30**, 685–693 (2010).

11. Kumar, A. *et al*. CXCR4 Physically Associates with the T Cell Receptor to Signal in T Cells. *Immunity* **25**, 213–224 (2006).

12. Kratchmarova, I., Blagoev, B., Haack-Sorensen, M., Kassem, M. & Mann, M. Mechanism of Divergent Growth Factor Effects in Mesenchymal Stem Cell Differentiation. *Science* **308**, 1472–1477 (2005).

13. Li Jeon, N. *et al*. Neutrophil chemotaxis in linear and complex gradients of interleukin-8 formed in a microfabricated device. *Nature Biotechnolgy* **20**, 826–830 (2002).

14. Nguyen, N.-T. *Fundamentals and applications of microfluidics*. (Artech House, 2002).

15. Petersen, K. E. Silicon as a mechanical material. *Proceedings of the IEEE* **70**, 420–457 (1982).

16. Manz, A. *et al*. Design of an open-tubular column liquid chromatograph using silicon chip technology. *Sensors and actuators B: Chemical* **1**, 249–255 (1990).

17. Manz, A., Graber, N. & Widmer, H. Miniaturized total chemical analysis systems: a novel concept for chemical sensing. *Sensors and actuators B: Chemical* **1**, 244–248 (1990).

18. Sanchez-Freire, V., Ebert, A. D., Kalisky, T., Quake, S. R. & Wu, J. C. Microfluidic single-cell real-time PCR for comparative analysis of gene expression patterns. *Nature Protocols* **7**, 829–838 (2012).

19. Agresti, J. J. *et al*. Ultrahigh-throughput screening in drop-based microfluidics for directed evolution. *Proceedings of the National Academy of Sciences* **107**, 4004–4009 (2010).

20. Nguyen, N.-T., Huang, X. & Chuan, T. K. MEMS-micropumps: a review. *Journal of Fluids Engineering* **124**, 384–392 (2002).

21. Stroock, A. D. & Whitesides, G. M. Components for integrated poly (dimethylsiloxane) microfluidic systems. *Electrophoresis* **23**, 3461–73 (2002).

22. Ugaz, V. M., Elms, R. D., Lo, R. C., Shaikh, F. A. & Burns, M. A. Microfabricated electrophoresis systems for DNA sequencing and genotyping

applications: current technology and future directions. *Philosophical Transactions of the Royal Society of London. Series A: Mathematical, Physical and Engineering Sciences* **362**, 1105–1129 (2004).

23. Stone, H. A., Stroock, A. D. & Ajdari, A. Engineering flows in small devices: microfluidics toward a lab-on-a-chip. *Annual Review of Fluid Mechanics* **36**, 381–411 (2004).

24. Somorjai, G. A. & Li, Y. *Introduction to Surface Chemistry and Catalysis*. (John Wiley & Sons, 2010).

25. Stone, H. A., Stroock, A. D. & Ajdari, A. Engineering flows in small devices: Microfluidics toward a lab-on-a-chip. *Annual Review of Fluid Mechanics* **36**, 381–411 (2004).

26. Gucker, F. T., O'Konski, C. T., Pickard, H. B. & Pitts, J. N. A Photoelectronic Counter for Colloidal Particles1. *Journal of the American Chemical Society* **69**, 2422–2431 (1947).

27. Zarrin, F. & Dovichi, N. J. Sub-picoliter detection with the sheath flow cuvette. *Analytical Chemistry* **57**, 2690–2692 (1985).

28. Jeong, W. *et al*. Hydrodynamic microfabrication via 'on the fly' photopolymerization of microscale fibers and tubes. *Lab on a Chip* **4**, 576 (2004).

29. Kenis, P. J. A., Ismagilov, R. F. & Whitesides, G. M. Microfabrication inside capillaries using multiphase laminar flow patterning. *Science* **285**, 83–85 (1999).

30. Goranovic, G. *et al*. Three-dimensional single step flow sheathing in micro cell sorters. in *Modeling and Simulation of Microsystems* (2001).

31. Ateya, D. A. *et al*. The good, the bad, and the tiny: a review of microflow cytometry. *Analytical Bioanalytical Chemistry* **391**, 1485–1498 (2008).

32. Lee, G.-B., Chang, C.-C., Huang, S.-B. & Yang, R.-J. The hydrodynamic focusing effect inside rectangular microchannels. *Journal of Micromechanics and Microengineering* **16**, 1024 (2006).

33. Lin, S. C., Yen, P. W., Peng, C. C. & Tung, Y. C. Single channel layer, single sheath-flow inlet microfluidic flow cytometer with three-dimensional hydrodynamic focusing. *Lab on a Chip* (2012).

34. Simonnet, C. & Groisman, A. Two-dimensional hydrodynamic focusing in a simple microfluidic device. *Applied Physics Letters* **87**, 104–114 (2005).

35. Wolff, A. *et al*. Integrating advanced functionality in a microfabricated high-throughput fluorescent-activated cell sorter. *Lab on a Chip* **3**, 22–27 (2003).

36. Juncker, D., Schmid, H. & Delamarche, E. Multipurpose microfluidic probe. *Nature Materials* **4**, 622–628 (2005).

37. Takayama, S. *et al*. Subcellular positioning of small molecules. *Nature* **411**, 1016 (2001).

38. Takayama, S. *et al*. Selective chemical treatment of cellular microdomains using multiple laminar streams. *Chemistry & Biology* **10**, 123–130 (2003).

39. Peret, B. J. & Murphy, W. L. Controllable soluble protein concentration gradients in hydrogel networks. *Advanced Functional Materials* **18**, 3410–3417 (2008).

40. Choi, N. W. *et al*. Microfluidic scaffolds for tissue engineering. *Nature Materials* **6**, 908–915 (2007).

41. Ramamurty, G. *Applied Finite Element Analysis*. (I. K. International Pvt Ltd, 2010).

42. Zienkiewicz, O. C. The Stress-Distribution in Gravity Dams. *Journal of the ICE* **27**, 244–271 (1947).

43. Zienkiewicz, O. C. & Morice, P. B. *The Finite Element Method in Engineering Science*. (McGraw-hill London, 1971).

44. Shavezipur, M. *et al*. A finite element technique for accurate determination of interfacial adhesion force in MEMS using electrostatic actuation. *Journal of Micromechanics and Microengineering* **21**, 115025 (2011).

45. Coulomb, J.-L. A methodology for the determination of global electromechanical quantities from a finite element analysis and its application to the evaluation of magnetic forces, torques and stiffness. *IEEE Transactions on Magnetics* **19**, 2514–2519 (1983).

46. Cheng, H. H., Huang, D.-S. & Lin, M.-T. Heat dissipation design and analysis of high power LED array using the finite element method. *Microelectronics Reliability* **52**, 905–911 (2012).

47. Takizawa, K., Moorman, C., Wright, S., Christopher, J. & Tezduyar, T. E. Wall shear stress calculations in space–time finite element computation of arterial fluid–structure interactions. *Computational Mechanics* **46**, 31–41 (2010).

48. *COMSOL Multiphysics: Version 3.5a. User's guide*. (Comsol, 2008).

49. Chaudhari, A. *et al*. Formation of sub-7 nm feature size PS-b-P4VP block copolymer structures by solvent vapour process. in *SPIE Advanced Lithography* 905110–905110 (International Society for Optics and Photonics, 2014).

50. Jackson, M. J. *Microfabrication and Nanomanufacturing*. (CRC Press, 2005).

51. Kim, P. *et al*. Soft lithography for microfluidics: a review. *Biochip Journal* (2008).

52. Qin, D., Xia, Y. & Whitesides, G. M. Soft lithography for micro-and nanoscale patterning. *Nature Protocols* **5**, 491–502 (2010).

53. Nielson, R. & Shear, J. B. Parallel chemical dosing of subcellular targets. *Analytical chemistry* **78**, 5987–5993 (2006).

54. Yao, P., Schneider, G., Prather, D., Wetzel, E. & O'Brien, D. Fabrication of three-dimensional photonic crystals with multilayer photolithography. *Optics Express* **13**, 2370–2376 (2005).

55. Skoog, D., West, D., Holler, F. & Crouch, S. *Fundamentals of Analytical Chemistry*. (Cengage Learning, 2013).

56. Kaiser, W. & Garrett, C. G. B. Two-Photon Excitation in CaF2: Eu2+. *Physical Review Letters* **7**, 229–231 (1961).

57. Denk, W. *et al*. Anatomical and functional imaging of neurons using 2-photon laser scanning microscopy. *Journal of Neuroscience Methods* **54**, 151–162 (1994).

58. Seidlits, S. K., Schmidt, C. E. & Shear, J. B. High-Resolution Patterning of Hydrogels in Three Dimensions using Direct-Write Photofabrication for Cell Guidance. *Advanced Functional Materials* **19**, 3543–3551 (2009).

59. Kaehr, B. & Shear, J. B. Multiphoton fabrication of chemically responsive protein hydrogels for microactuation. *PNAS* **105**, 8850–8854 (2008).

60. Kaehr, B. *et al*. Direct-write fabrication of functional protein matrixes using a low-cost Q-switched laser. *Analytical chemistry* **78**, 3198–3202 (2006).

61. Nielson, R., Kaehr, B. & Shear, J. B. Microreplication and Design of Biological Architectures Using Dynamic-Mask Multiphoton Lithography. *Small* **5**, 120–125 (2009).

62. Kaehr, B., Allen, R., Javier, D. J., Currie, J. & Shear, J. B. Guiding neuronal development with in situ microfabrication. *PNAS* **101**, 16104–16108 (2004).

63. Spikes, J. D., Shen, H.-R., Kopečková, P. & Kopeček, J. Photodynamic Crosslinking of Proteins. III. Kinetics of the FMN- and Rose Bengal-sensitized Photooxidation and Intermolecular Crosslinking of Model Tyrosine-containing N-(2-Hydroxypropyl)methacrylamide Copolymers. *Photochemistry and Photobiology* **70**, 130–137 (1999).

64. Fairbanks, B. D., Schwartz, M. P., Bowman, C. N. & Anseth, K. S. Photoinitiated polymerization of PEG-diacrylate with lithium phenyl-2,4,6-trimethylbenzoylphosphinate: polymerization rate and cytocompatibility. *Biomaterials* **30**, 6702–6707 (2009).

65. Bloembergen, N. Laser-induced electric breakdown in solids. *IEEE Journal of Quantum Electronics* **10**, 375–386 (1974).

66. Pronko, P. P. *et al*. Avalanche ionization and dielectric breakdown in silicon with ultrafast laser pulses. *Physical Review B* **58**, 2387 (1998).

67. Scheggi, A. M. V. *Biomedical Optical Instrumentation and Laser-Assisted Biotechnology*. (Springer Science & Business Media, 1996).

68. Hoppe, T. J. *Laser-Based Techniques for Manipulating the Single-Cell Environment*. Dissertation, University of Texas at Austin (2013).

69. Phipps, C. *Laser Ablation and Its Applications*. (Springer, 2007).

Chapter 2: Applications of μ-3D Printing for Improved Cell Dosing

2.1 Introduction

Cellular growth, development, differentiation, and death are mediated to some degree by the interaction of external cues with plasma membrane receptors. Critically, chemically mediated signals are interpreted by intracellular transduction pathways resulting in profound changes to cell motility [1], axonal pathfinding [2], immune response [3], and cell differentiation [4]. Traditionally the cellular response to chemical cues has been studied by exposing entire culture dishes to a desired reagent. While the addition of soluble reagents homogenously to cell culture dishes provides a basis for understanding much of cell biology, greater spatial resolution of reagent delivery is necessary in order to elucidate mechanisms on the subcellular scale.

Several cell types are known to respond to subcellular cues. Neutrophils have been shown to respond to foreign material by re-orienting chemoattractant receptors within regions of the cell smaller than 10 μm in length [5]. In culture, hippocampal dendritic synapses are located on average 5 μm apart [6]. However, common techniques capable of maintaining steep concentration gradients cannot deliver streams of neurotropic factors smaller than 10 μm in width [7][8]. These low-resolution techniques result in the excitation of multiple synapses, confounding the source of the action potential and preventing the isolation of single synapses. Furthermore, it has been demonstrated that cellular processes including focal adhesions are present predominately at the basal cell surface in planar cell culture [9][10]. Dosing techniques with subcellular resolution with regard to the basal and dorsal cell regions are needed to probe these heterogeneities.

Subcellular reagent dosing has been demonstrated with the release of chemically caged neurotransmitters by two-photon mediated photoactivation [11][12]. This technique provides very high reagent delivery resolution (<1 μm^3) due to the nature of two-photon absorption, but requires the costly development of a two-photon caged molecule for each desired reagent to be used. Additionally, two-photon photoactivation suffers from diffusion of uncaged reagents and is not useful for dosing for extended time frames.

Micropipettes have been used extensively as a method to guide cellular processes such as neutrophil pathfinding [1], cardiomyocyte depolarization [13], and neuronal growth cone formation [14]. While this technique allows for a wide range of reagents to be delivered and diameters as small as 1 μm at the pipette tip, it is difficult to dose more than one cell at a time and sharp boundaries in reagent concentration are not possible. Streams from a micropipette are broadened due to diffusion, resulting in much wider dosing areas than the width of the pipette [15].

In order to address the need for high resolution subcellular dosing techniques, the Shear group has developed tools to deliver microgradients of reagents to arbitrary locations in a cell culture environment including neutrophil and neuronal cell models [16][7]. However, streams less than ~20 μm in width are not achievable without high linear flow rates, resulting in shear forces unamenable to cell culture. Furthermore, these techniques offer only 2D control and cannot provide a gradient of effector molecules above the cell culture surface. While it is known that many cellular processes occur differently between a 2D surface and a 3D scaffold [17], little is known about the difference in cell behavior due to 3D gradients of soluble factors in place of traditional 2D gradients.

The Shear group has demonstrated the flexibility of the microfluidic platform with multiple cell types and incorporated a valve system to allow for the 360° spatial control of the system during cell culture [16] and dosing with complex patterns of multiple reagents [8]. However, the cell dosing platform was only capable of directing flow within the 2D surface of the cell culture area, no more than ~9 μm from the surface, with a stream width of 15 - 45 μm [8].

Microscopic three-dimensional (μ-3D) printing has been employed within a microfluidic chamber in this dissertation. Using μ-3D printed structures, greater spatial control over the fluid dynamics within the flow chamber was achieved. Using high intensity laser light to achieve μ-3D printing, a technique developed in the Shear group, has been completed primarily on cover glass due to its optical transparency and wide use in cell culture. In order to incorporate μ-3D printing with the site-selective microfluidic dosing device, laser energy must be focused onto the surface of a 7.6 μm thick film. However, μ-3D printing has remained challenging on thin materials as the high laser intensity necessary for printing also promotes avalanche ionization that leads to ablation of the thin polymer film.

To overcome these limitations, materials with higher crosslinking efficiency have been used including 700 Da polyethylene glycol diacrylate (PEGDA). Higher crosslinking efficiency allows for a decrease in laser fluence and reduces the possibility of ablation of the polyimide film during printing. Furthermore, PEGDA has a reported low cytotoxicity as a photocrosslinking agent, with 95% human neonatal foreskin fibroblast survival in a hydrogel fabricated from PEGDA monomers [18].

In order to improve upon the subcellular dosing precision, this chapter explores a system capable of hydrodynamically focusing the dosing streams in a cell culture environment. Additionally, using μ-3D printing techniques to reduce the variability of the

stream width lower cost optics and lasers may be used without sacrificing stream size. These tools will allow researchers to probe cells with higher spatial precision in order to gain new insights into cellular mechanisms on a subcellular scale.

2.2 EXPERIMENTAL METHODS

2.2.1 μ-3D Printing

Micro-three-dimensional printing (μ-3D printing) was performed using a mode-locked Ti:sapphire laser tuned to 740 nm with a pulse duration < 130 fs and repetition rate of 76 MHz (Coherent, Mira 900F). Photomasks were displayed using the SVGA graphics output of a desktop computer displayed on an 800 x 600 pixel digital micromirror device (DMD) (BenQ, MP510) capable of modulating each mirror ~20° when switched from a white to black graphical input (Figure 2.1). Dual-axis galvanometer scan mirrors (Thor Labs) were used to raster the beam at 50 mHz and 100 Hz across the x- and y-axis, respectively. A series of relay lenses were used to focus the beam onto the DMD and collimate the beam into the back aperture of a 60x, 1.4 NA objective within a Nikon inverted microscope. The z-axis position was dictated by a digital piezo controller and multi-axis nanopositioning system with capacitive sensors (Physik Instrumente, E-710). Control of the stage, scan mirrors, and DMD was synchronized using custom routines created in LabView™ (National Instruments). Photomasks were displayed at each z-axis position and updated during z-axis steps while the raster scan was at a terminal position. The DMD photomask system was placed conjugate to the plane of printing, so that each mask corresponded to a single layer of printing. Laser power at the objective back aperture was attenuated to 22-30 mW with a beam splitting cube and half-wave plate. Microstructures were fabricated from a solution

consisting of 10 mM Rose Bengal, 20% (v/v) PEGDA, and 9.1% (w/w) BSA, unless otherwise noted.

To achieve μ-3D printing within a microfluidic device (described in section 2.2.2), 40 μL of printing solution was pipetted into the flow chamber and the polyimide film placed on #1 coverglass for printing with an oil immersion Nikon 60x, 1.4 NA microscope objective. Once printing was complete, excess printing solution was removed with 20 injections of 100 μL deionized water into the flow chamber. The reverse side of the polyimide film was cleaned with isopropanol and a second flow chamber adhered before reagents were pumped into the apparatus.

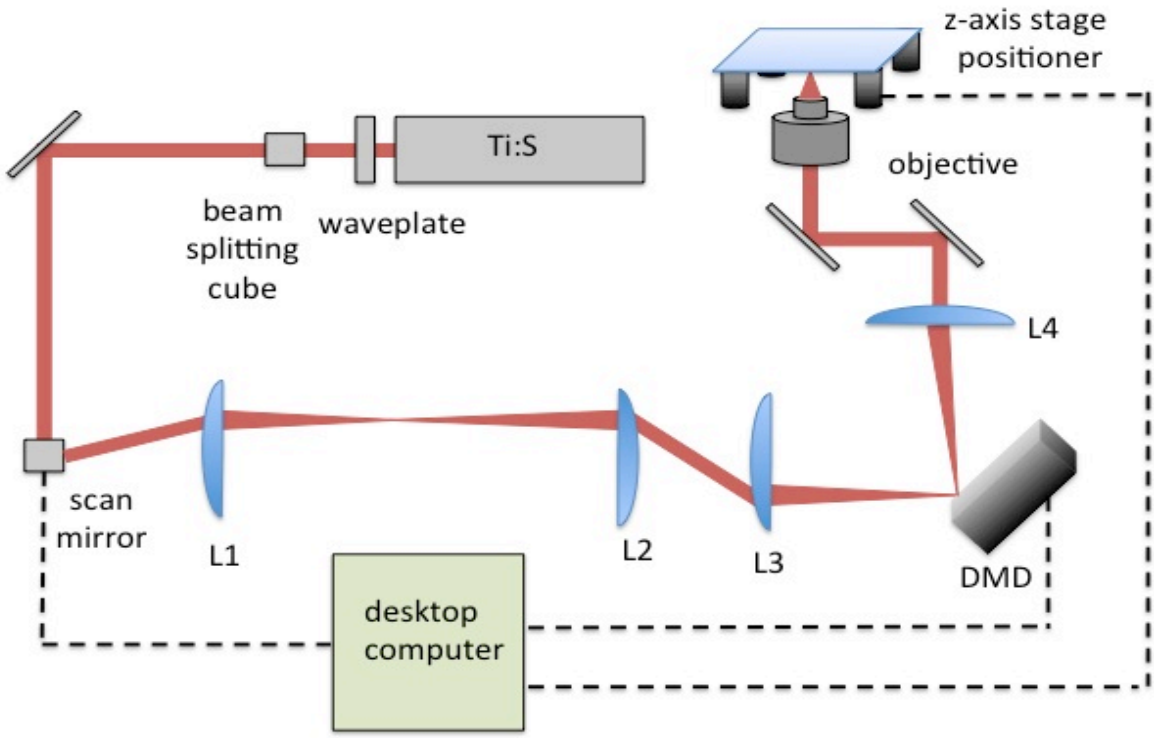

Figure 2.1: Schematic for μ-3D printing controlled by a desktop computer with Labview software. Photomasks were displayed on a digital micromirror device (DMD) in a conjugate plane to printing plane. The laser power delivered to the objective was attenuated with a polarizing beam splitting cube/half wave plate pair. A scan mirror translated the beam in two axes across the DMD surface. Lens pair L1 and L2 collimated and expanded the beam, while L3 focused the beam onto the DMD and L4 collimated the beam into the back aperture of the objective.

2.2.2 Device

The cell dosing apparatus consisted of two flow chambers (Grace Bio-Laboratories, 440889B) each with dimensions of 30 mm (length) × 2.5 mm (width) × 0.12 mm (height) enveloping a 7.6 μm-thick polyimide film (Dupont, Kapton 30HN). Reagents were delivered and drained for each flow chamber via press-fit tubing connectors (Grace BioLaboratories, 460003) and platinum-cured silicone tubing (Cole-Parmer, 95802-01) with syringes driven by electromechanical pumps (Braintree Scientific, BS-9000). The flow conditions were similar to those known to be compatible with cell culture within the system and capable of maintaining low Reynolds number laminar flow of 0.1 – 0.6 mL/min (0.6 – 3.3 cm/s). The flow rate was maintained 0.1 – 0.2 mL/min lower in the flow chamber in which cells were cultured, creating a pressure gradient across the polyimide film in order to drive flow through laser-ablated pores. The system operates in the laminar flow regime (Reynolds number $\approx$ 0.3) with minimal diffusion (Peclet number $\approx$ 3,300 for a 20 μm wide stream).

In order to assemble the device, the polyimide film was stretched with an 8 cm diameter spring tension hoop and applied to a plastic (poly-(oxymethylene)) frame (2 cm × 6 cm) with double-sided adhesive tape (3M, 66512900). The polyimide film was then cleaned with isopropyl alcohol and a single flow chamber was applied to each side using adhesive provided by the manufacturer (Grace Bio-Laboratories, 440889B) (Figure 2.2).

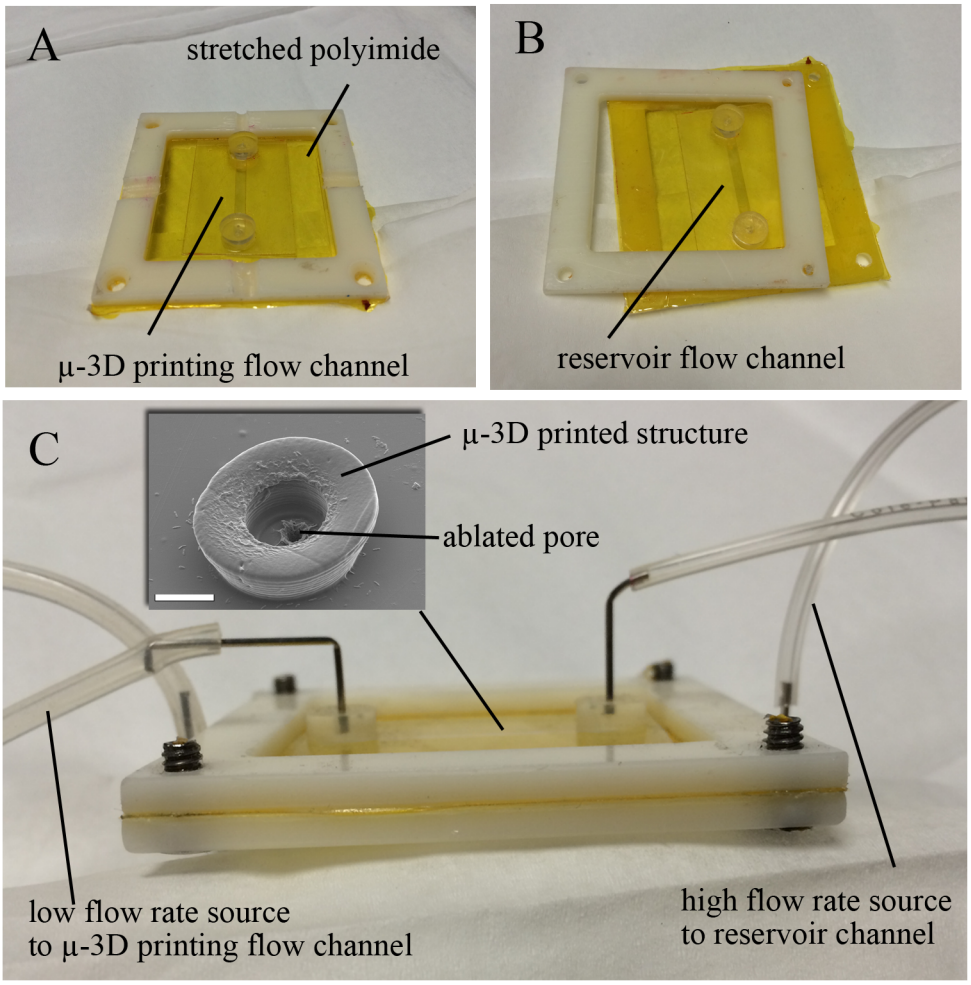

Figure 2.2: μ-3D printing within the microfluidic device. (a) A 7.6 μm-thick polyimide film was stretched and applied to a square frame before a flow chamber was adhered to the stretched film. This configuration was used for μ-3D printing. (b) After μ-3D printing, the reverse side of the polyimide film was cleaned with isopropanol and a second flow chamber adhered before reagents were pumped into the apparatus. (c) Screws were applied to the frame to ensure that tension was maintained across the polyimide film while syringe pumps were used to deliver flow into each flow channel. The inset SEM image depicts a μ-3D printed chimney structure and ablated pore. The sample was removed from the device and dried before imaging. Scale bar, 10 μm.

Fluorescein dye (10-20 μM) was used to image streams emitted from the pores to determine the effect microstructures have on laminar flow streams originating at each pore. Fluorescein (pK_a = 6.4) forms a monoanion in acidic solutions that exhibits roughly one third of the fluorescence emission obtained when the molecule forms a cation in basic solutions [19]. Fluorescein solutions titrated with HCl and unbuffered (pH 4) were used to minimize fluorescence signal in the out of plane optical axis, while a chamber flowing 200 mM Tris (pH 9) generated higher fluorescence signal where the dye was received. Wide-field fluorescence images of this process were acquired using a Zeiss Axiovert 135 inverted microscope, Zeiss HBO 100 mercury arc lamp, and Hamamatsu Orca II charge-coupled device (CCD) camera (C4742-98) controlled by MetaMorph imaging software (Molecular Devices) using a Zeiss 20x, 0.5 NA objective.

2.2.3 Chemicals and Materials

Bovine serum albumin (BSA; BAH64) was purchased from Equitech-Bio (Kerrville, TX). MitoTracker Green FM (M7514) and Syto 13 (S7575), DAPI (D1306), CellTracker Green CMFDA (C2925), and Alexa Fluor 568 phalloidin (A12380) were purchased from Molecular Probes (Eugene, OR). Tris(hydroxymethyl)aminomethane (Tris; 252859) and 700 Da polyethylene glycol diacrylate (PEGDA; 455008) were purchased from Sigma-Aldrich (St. Louis, MO). Fluorescein (119241000) was purchased from Acros Organics (Geel, Belgium).

2.2.4 Cell Culture

NG108-15 cells purchased from American Type Culture Collection were cultured in Dulbecco's modified Eagle's medium (DMEM; Corning Cellgro) supplemented with 10% (v/v) fetal bovine serum (HyClone, AVJ82746), 1% (v/v) penicillin/streptomycin (MP Biomedicals), and 1x HAT (1 x 10^{-4} hypoxanthine, 2x 10^{-7} aminopterin, 1.6 X

10^{-4} thymidine). 50x HAT solution was purchased from MediaTech. Polystyrene flasks (25 cm^2) were maintained at 37° C in a 5% CO2 incubator at 100% relative humidity. The cells were passaged at 1:10 dilution every 3 days using only mechanical shaking to dislodge adherent cells.

After microstructure printing within the flow chamber, the fully assembled flow chamber apparatus was incubated in a solution of 30% ethanol/water, 1.0 mg/mL rat-tail collagen (354249, BD Biosciences) overnight. The flow chamber was then equilibrated with 20 injections of 100 μL of Leibovitz (L-15) medium (SH30525, HyClone).

For seeding within flow chambers, NG108-15 cells were removed from the flask mechanically, centrifuged for 3 min at 1000 rpm, and suspended in 1% FBS L-15 media at 1-3 $\times$ 10^6 cells/mL. The flow chamber was incubated in a 37 ° C incubator for 3-5 hours before pumping reagents into the flow chamber. If cell adherence was low, additional injections of 1-3 $\times$ 10^6 cells/mL into the flow chamber were completed after a 1 hr incubation to ensure high density of cells within the chamber.

Rat Schwann cells (RSC) isolated from neonatal Sprague-Dawley rat sciatic nerves were donated by Shalu Suri and Christine Schmidt after following a protocol described by Kleitman and colleagues [20]. Suri and Schmidt reported that sciatic nerve pieces were enzymatically digested, centrifuged, and resuspended in cytosine arabinoside to minimize fibroblast proliferation. After 3 days, cytosine arabinoside was removed, and the remaining fibroblasts were killed via complement-mediated lysis by mouse anti-rat CD90/Thy1.1 (Accurate, Westbury, NY). RSC obtained from this method were found to be >99% pure by Suri and Schmidt as confirmed by immunostaining using anti-S100 antibody (Dako, Carpinteria,CA) [21].

RSC were cultured in DMEM media with 10% (v/v) fetal bovine serum (FBS), 30 mg/mL bovine pituitary extract, and 2 mM forskolin. To passage, all media was

removed from the culture flask and the cells were incubated in 0.25% trypsin, 0.53 mM EDTA (MediaTech) for 5 minutes before quenching with culture media. For cell dosing experiments the cells were resuspended at 1 M cells/mL in 1% FBS L-15 media and incubated at 37 ° C for 3-5 hr before dosing.

2.2.5 Cell Dosing

Pores were created using focused light from a frequency-doubled (532 nm), microchip Q-switched Nd:YAG laser with a pulse width of ~600 ps and repetition rate of 7.65 kHz. The laser output was attenuated with a half-wave plate and polarizing beam splitter to 10 - 20 mW at the back aperture of a 20x, 0.5 NA objective in a Zeiss Axiovert inverted microscope (Figure 2.3). The laser beam was collimated so as to underfill the back aperture of the objective and create a Gaussian focus in order to stretch the focal spot in the optical axis. Each pore was created with a pulse train of 10 exposure periods of 10 ms in length (~77 pulses) with a 50 ms delay between pulses controlled by a Uniblitz UHS1 shutter (Vincent Associates, VMMT1).

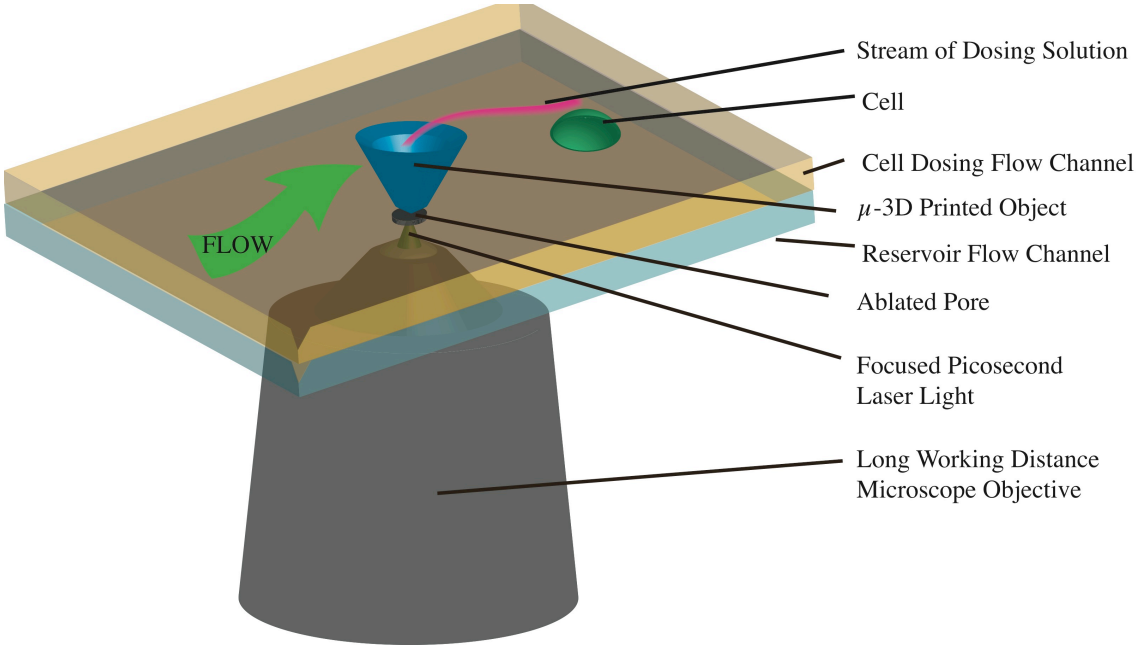

Figure 2.3: Cell dosing with a μ-3D printed structure. After a structure has been printed within the flow chamber, a second flow chamber was applied to the reverse side of the polyimide film. A pore was ablated into the film using an Nd:YAG (532 nm) laser with a picosecond pulse width focused using an under-filled 20x 0.5 NA microscope objective. The pore allows a narrow stream of reagent from the reservoir flow channel to enter the cell dosing flow channel. The position and size of the flow stream was determined by the placement of the μ-3D printed structure.

2.2.6 Confocal Imaging

Confocal fluorescence microscopy (Zeiss, LSM 710) was used to image microstructures and flow patterns using fluorescein dye. The laser scanning microscope (LSM) system was controlled by Zen software (Zeiss; Jena, Germany) including objective lenses, stage position, pinhole size, PMT gain, and excitation lasers. Detection wavelengths were selected based on dye emission spectra using the 34-channel Zeiss QUASAR detector, also controlled by the Zen software. The QUASAR detector uses a diffraction grating to disperse the emitted fluorescence light across a detector array.

Confocal fluorescence microscopy was used to obtain green fluorescence signal from streams of unbuffered 10 μM fluorescein (pH 4) within a flow chamber of 200 mM Tris (pH 9). Fluorescein dye fluorescence was imaged using an Argon laser (488 nm) and detected between 493-556 nm. The fluorescence signal from microstructures (containing residual Rose Bengal) was excited with a DPSS laser (561 nm) and detected at 566-711 nm. The fluorescence of nucleic acid stain DAPI was imaged with a diode laser (405 nm) and detected from 410-516 nm. Alexa Fluor 568 phalloidin was imaged with a DPSS laser (561 nm) and detected at 585-733 nm. CellTracker Green CMFDA fluorescence was imaged with an Argon laser (514 nm) and detected between 515-602 nm.

Confocal imaging on glass substrates was completed with a Zeiss plan-apochromatic 63x, 1.4 NA oil immersion objective (190 μm working distance), while confocal imaging within polyimide flow chambers required at longer working distance Zeiss plan-apochromatic 20x, 0.8 NA air objective (550 μm working distance).

The stream width for streams focused by chimney structures and unmodified streams was determined from the plane with greatest signal intensity. The stream width of control pores ablated near each structure was paired with the stream width of chimney structures. Triangle-shaped structures were paired with a nearby unmodified pore for stream width analysis including a paired t-test.

2.2.7 Sample Preparation for Electron Microscopy

Samples were prepared for scanning electron microscopy (SEM) after μ-3D printing by washing away excess printing solution 20 times with phosphate buffered saline (PBS, pH 7.4). To ensure structural integrity, the printed microstructures were incubated for 15 minutes at room temperature in 15% (w/v) glutaraldehyde in PBS. Five exchanges were then completed with each of the following solutions sequentially with a

15 minute incubation period: 100% deionized water, 50% deionized water/50% ethanol, 100% ethanol, 100% methanol. The specimen was dried overnight in a desiccated chamber and mounted to SEM pin stub mount (Ted Pella, 16111). The specimen was then sputter coated using a Pt/Pd target to a nominal thickness of 12 nm and imaged with a Carl Zeiss SUPRA 40 SEM.

2.2.8 Stream Width Analysis

All streams were included in the analysis unless the signal was below detectable levels or debris caused stream deviations more than 15 degrees from parallel with regard to bulk flow in the flow chamber. An orthogonal line scan was taken 200 μm downstream of the stream source (ablated pore) and the stream width was determined from the full-width half max (FWHM) of a Gaussian fit created by Matlab 7.7.0 software (MathWorks; Natick, Massachusetts) with the provided "gauss1" fitting routine. Goodness of fit was determined to be greater than 0.95 for R^2 or the fit was rejected. A t-test was used to compare stream widths for all structures.

2.2.9 Finite Element Modeling

In order to determine geometries that have effective flow properties, finite element modeling was employed using COMSOL Multiphysics 4.2.1 (Comsol, Inc.; Los Angles, California). The model was based on average ablated pore size from SEM images (3 μm) and flow rates (0.1 and 0.3 ml/min) set for positive displacement electromechanical syringe pumps (Braintree Scientific, BS-9000). The boundary conditions for the walls of the flow chamber and exterior of μ-3D printed structures were assumed to be impermeable and no slip. The model first completed a simulation of laminar flow assuming incompressible flow governed by the Navier-Stokes equation (see Chapter 1) and the viscosity and density of liquid water at room temperature. Next, the

model simulated the diffusion and convection of fluorescein dye from the previously solved velocity field, assuming the conservation of mass. The diffusion coefficient of fluorescein in water was set to a reported value of 0.64 x 10^{-9} m^2/s [22]. These numerical simulations were validated with physical data from confocal fluorescence microscopy.

2.2.9.1 Mesh Size Optimization

For 3D finite element modeling, a small mesh size was critical to maintaining an accurate model. However, due to the limitations of the computer hardware (32 GB installed memory), a mesh size of 2 μm per side (maximum value per triangle side) resulted in overflow of available memory and hard disk swapping. While mesh sizes larger than 2 μm were solved in under an hour, a mesh size of 2 μm resulted in too many elements for the 32 GB of memory to store and several days were required to solve each model (Figure 2.4). The model could not be scaled down without modifying the diffusion coefficient and other physical properties to account for the change in length scale. Instead, a high resolution (low mesh size) and low resolution (high mesh size) region of the model was demarcated. The area of interest (pore, μ-3D printed structure, and cell) were set to 2.75 μm maximum mesh size, while the rest of the flow chamber was set to a higher 50 μm mesh size. An area 250 μm downstream of the pore and structure were included in the high resolution region and all stream data were analyzed in this high resolution region. The mesh algorithms included in Comsol Multiphysics created a gradual increase in mesh size at points of contact between the high and low resolution mesh regions. This resulted in model completion times of one hour, allowing for rapid geometry optimization over a single day.

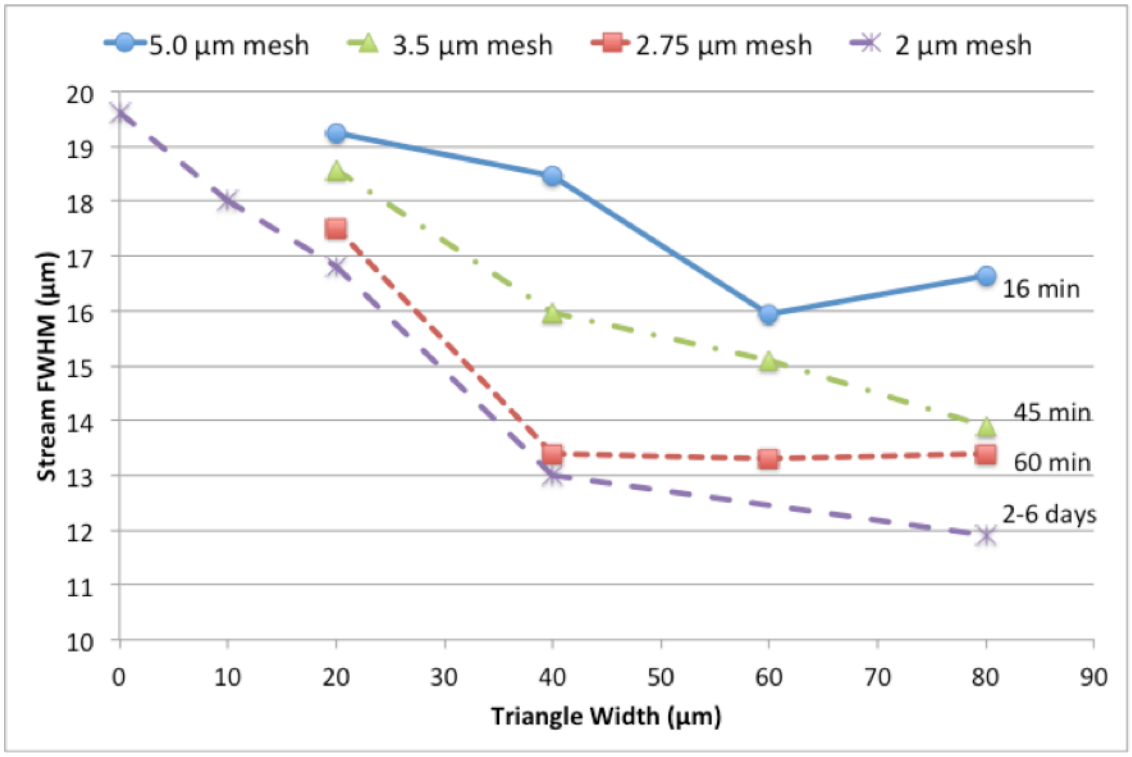

Figure 2.4: Mesh size optimization. The 3D finite element mesh size was varied using a model of a 3D printed triangle placed downstream of a pore. The full-width-half-max (FWHM) stream size 200 μm downstream of a pore was measured using a z-axis linescan. The isosceles triangle width at the side closest to the pore was varied while the triangle length (60 μm) and height (20 μm) were maintained. The time required to solve each model in Comsol Multiphysics is noted next to each dataset.

In fact, a 2.75 μm mesh size is not ideal for studying the effects of streams 10–20 μm in size. Ideally, the mesh size would be small enough to have no effect on the model results. However, the results obtained with the 2.75 μm mesh size were useful in informing the optimal design geometry due to the consistent trends apparent in the model results regardless of mesh size. That is, for a given mesh size the model was optimized to find the smallest stream width and this geometry was 3D printed.

2.2.9.2 Geometry Optimization

The geometries of fabricated microstructures were optimized though iterative numerical modeling using the FWHM of the simulated stream emitted from a pore and the spatial location of the dye field. FWHM was determined from linescan values automated with a Matlab script created to determine the baseline value, subtract the baseline from the dataset, fit the data to a Gaussian curve, and output regression statistics. The FWHM was then determined from the Gaussian curve, not the raw data, to reduce noise created by a choosing a single maximum value from the raw data.

2.3 RESULTS AND DISCUSSION

The ability to fabricate objects of any 3D shape in the path of flow opens a myriad of applications previously not achievable with this site-specific dosing system. The geometry of the fabricated structure perturbs flow lines away from parallel laminar flow and the resulting downstream realignment of flow mimics hydrodynamic focusing. It is thus possible to fabricate a microstructure downstream of a flow opening or to fabricate a structure that encompasses the opening so as to direct flow away from the surface of the flow chamber. Applying the principles of hydrodynamic focusing to the microfluidic platform, the reagent flow emanating from an ablated pore can be guided and focused by flow lines around microstructures. To take advantage of this phenomenon, microstructures were designed and 3D printed to create narrow streams for cell dosing.

2.3.1 Physical Demonstration of Stream Width Reduction

The inner diameter of the pore is only ~3 μm, but this source results in streams 15-45 μm in width in both the finite element models and physical experiments. The stream width can be reduced both in simulations and physically using a triangle μ-3D printed directly downstream of the pore. In order to study this effect, a control pore was

created both in simulations and in physical experiments 150 μm away from the triangle pore. SEM images of a representative pore and μ-3D printed triangle are depicted in Figure 2.5. A representative triangle-focused stream and control stream is shown with a linescan of fluorescence signal 200 μm downstream overlaid for reference (Figure 2.5, c).

A finite element model of triangle geometry and a parallel control stream suggests that local flow rates are decreased around the triangle, as represented by vectors with proportional length to the flow rate at each point in the model (Figure 2.5, d). Because this image only represents a single xy-plane of a 3D model, the dye stream location above the plane in the z-axis is not shown. Although the triangle-focused stream is elevated to a higher z-plane with corresponding faster flow rates, assuming a no-slip boundary condition. The residence times for the control stream and triangle-focused stream are equivalent at ~250 μm downstream as measured within the model (data not shown). This is because the triangle-focused dye is entrained in slower flow at the surface of the triangle.

2.3.2 Triangle Optimization

Many shapes were tested to find the optimal geometry to focus a stream. An equilateral triangle μ-3D printed within a flow chamber produced a strong focusing effect when placed directly downstream of a pore. The dimensions of the triangle in the x-, y-, and z-axes were optimized using 3D finite element modeling (Figure 2.6). An acute isosceles triangle with a base of 60 μm and sides of 50 μm created the narrowest stream of dye, as determined by the FWHM of the simulated concentration profile at 250 μm downstream.

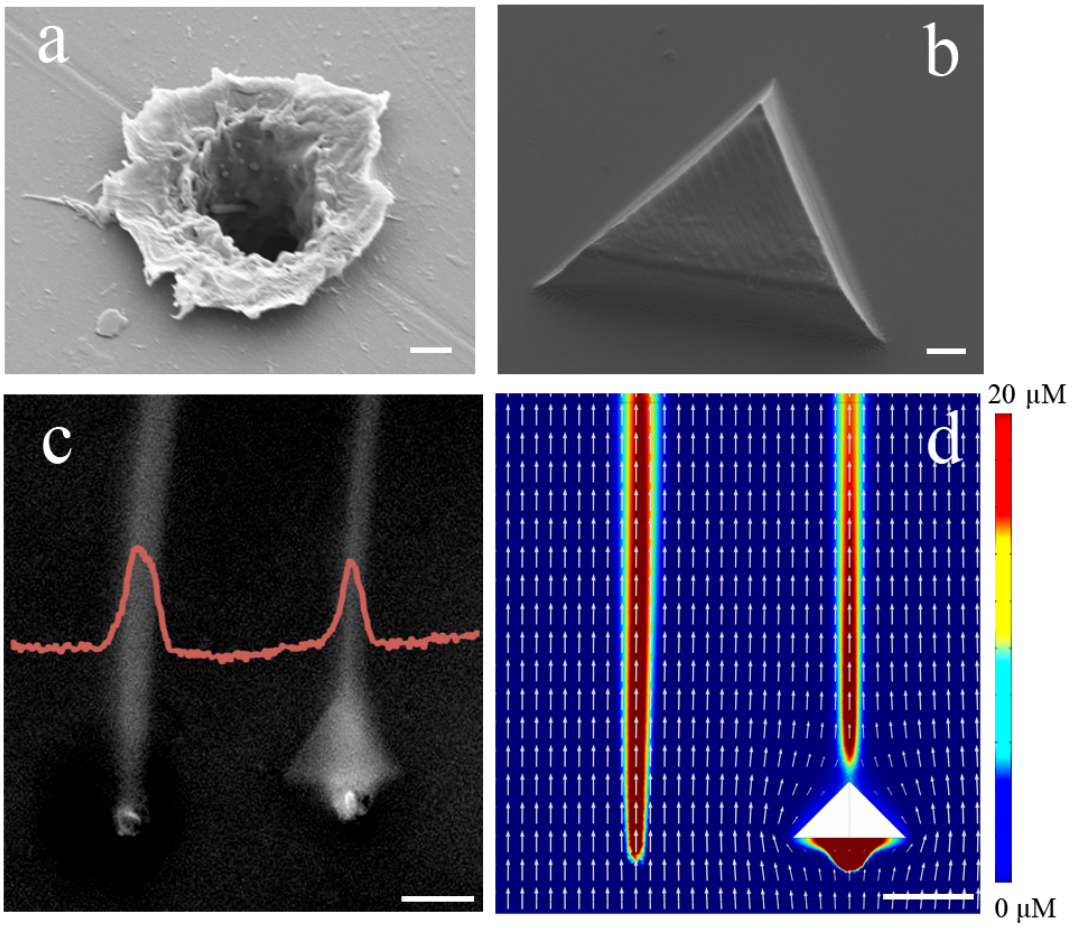

Figure 2.5: Microstructure effect on stream width. (a) Scanning electron micrograph of a representative pore ablated within polyimide film. Scale bar, 2 μm. (b) Scanning electron micrograph of a representative microstructure used for stream focusing, μ-3D printed to a nominal height of 20 μm. Scale bar, 10 μm. (c) Triangle-shaped microstructure pore (right) and unperturbed control pore (left) emitting a solution of 10 μM fluorescein into a chamber flowing 200 mM Tris buffer (pH 9). The fluorescence intensity at a distance 200 μm downstream of each pore is overlaid. Scale bar, 50 μm. (d) A finite element model of a control stream (left) and a triangle-focused stream (right). Simulated dye concentration and proportional flow vectors are displayed. Scale bar, 50 μm.

Physical data and simulations confirmed that structure height (z-axis) was a critical parameter in determining if streams emanating from a pore are directed around the structure or over. Simulations suggested that minimal stream width and maximal hydrodynamic focusing could be achieved when the dye stream is split and directed both around the structure and over it. As suggested by sheath flow theory, simulations return maximal focusing when the reagent stream flow rate is reduced while increasing the bulk flow rate of the flow channel [23]. Thus, focusing is maximized when the reagent stream is entrained in relatively slower boundary flow at the structure surface while impinging the reagent with bulk flow directed around the structure. However, there appeared to be a counteracting effect if the stream is forced to flow over the surface of a larger structure. The stream width was minimized to 12.5 μm with a triangle width of 60 μm. With a larger triangle, the flow lines were not ideal for hydrodynamic focusing and spread the reagent into the bulk flow with wider flow lines.

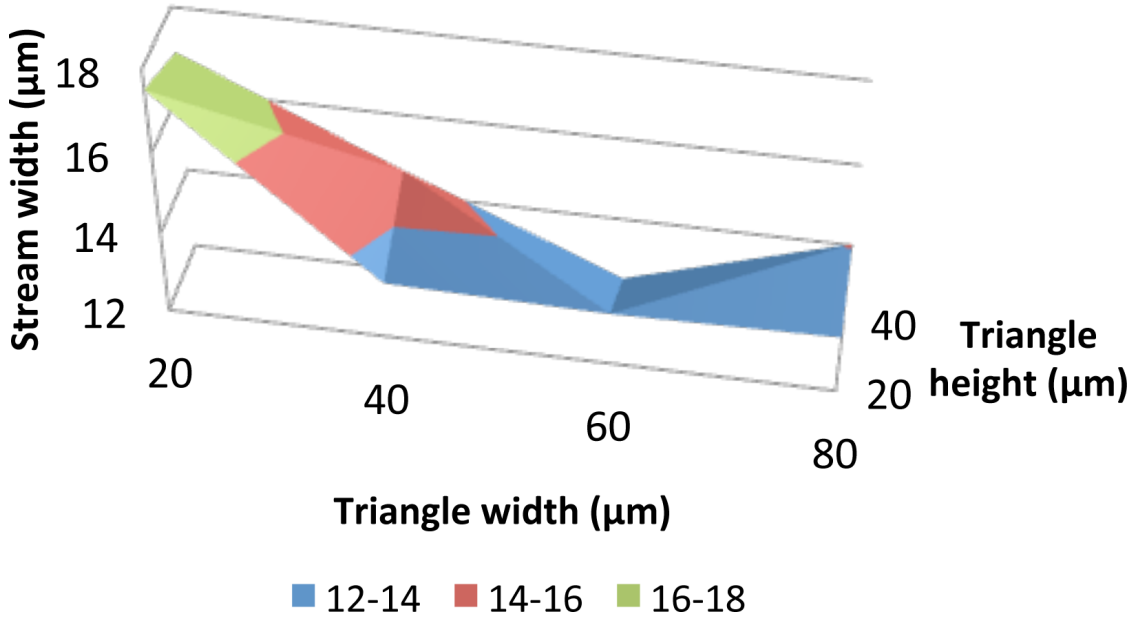

Figure 2.6: Optimization of triangle size using finite element modeling. Triangle height and width are varied individually in order to minimize the width of a simulated focused stream. Stream width was determined by FWHM of simulated dye concentrations 200 μm downstream of the source pore. A triangle width of 60 μm results in minimal stream width at either 20 or 40 μm in height. These parameters were used to create μ-3D printed replicas for cell dosing.

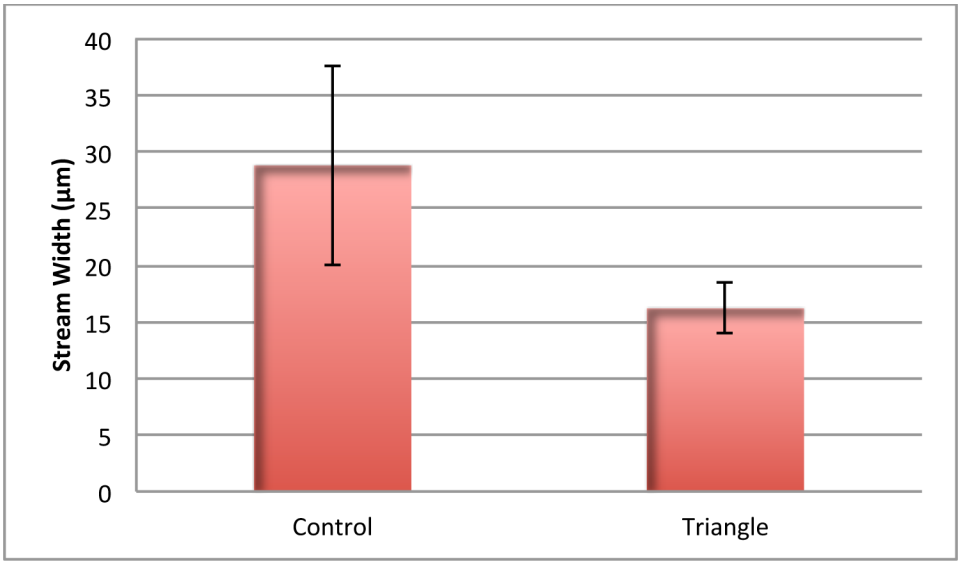

Figure 2.7: Stream width (FWHM) was reduced by hydrodynamic focusing from 29 μm to 16 μm ($p < 0.009$) as determined by wide field fluorescence signal of 10 μM fluorescein. Error bars represent standard deviation (n =5). To increase contrast, the 10 μM fluorescein solution was not buffered while 200 mM Tris (pH 9) flows in the opposing flow chamber. To reduce variability in peak height measurements, stream FWHM was determined using Gaussian curve fitting.

In order to elucidate the effect of the microstructure on the resulting downstream width of the emitted stream, FWHM fluorescence signal intensity was compared between triangle-shaped microstructure streams and parallel streams emitted from unperturbed pores. Stream width was reduced by hydrodynamic focusing from 29 μm to 16 μm ($p< 0.009$) as determined by widefield fluorescence signal of 10 μM fluorescein (Figure 2.7).

2.3.3 High Resolution Cell Dosing within Sheath Flow Streams

Previous work in the Shear lab has shown that laminar streams of reagent can be formed by laser ablation of polyimide films at arbitrary locations within a laminar flow chamber and delivered to cultured cells within the chamber. However, streams less than

~20 μm in width were not achievable without linear flow rates resulting in shear forces unamenable to cell culture [7]. For cells such as neutrophils, the stream width was approximately equal to the cell width and subcellular resolution was not possible unless the flow path could be constricted.

To demonstrate the efficacy of triangle-shaped microstructures on subcellular dosing, Schwann cells were cultured on polyimide film after μ-3D printing microstructures (Figure 2.8). Membrane-permeant stain Syto 13 was used as a marker for cell dosing. Syto 13 is a nucleic acid stain and appears to bind to the DNA in the nucleus of only Schwann cells within the path of the stream. Although there were at least 45 cells visible under bright field imaging (Figure 2.8, a), only 9 cells appear fluorescent due to a focused stream of Syto 13.

2.3.4 3D Characteristics of Streams

Three-dimensional stream characteristic were investigated in order to provide uniquely focused reagent streams above the cell culture plane. Finite element modeling (Figure 2.9) was applied to determine the optimal shape of a chimney structure to deliver streams at a desired height above the surface of the flow chamber. In addition, the stream width in the x- and z-axis was optimized to be of minimal size so as to maintain precise dosing.

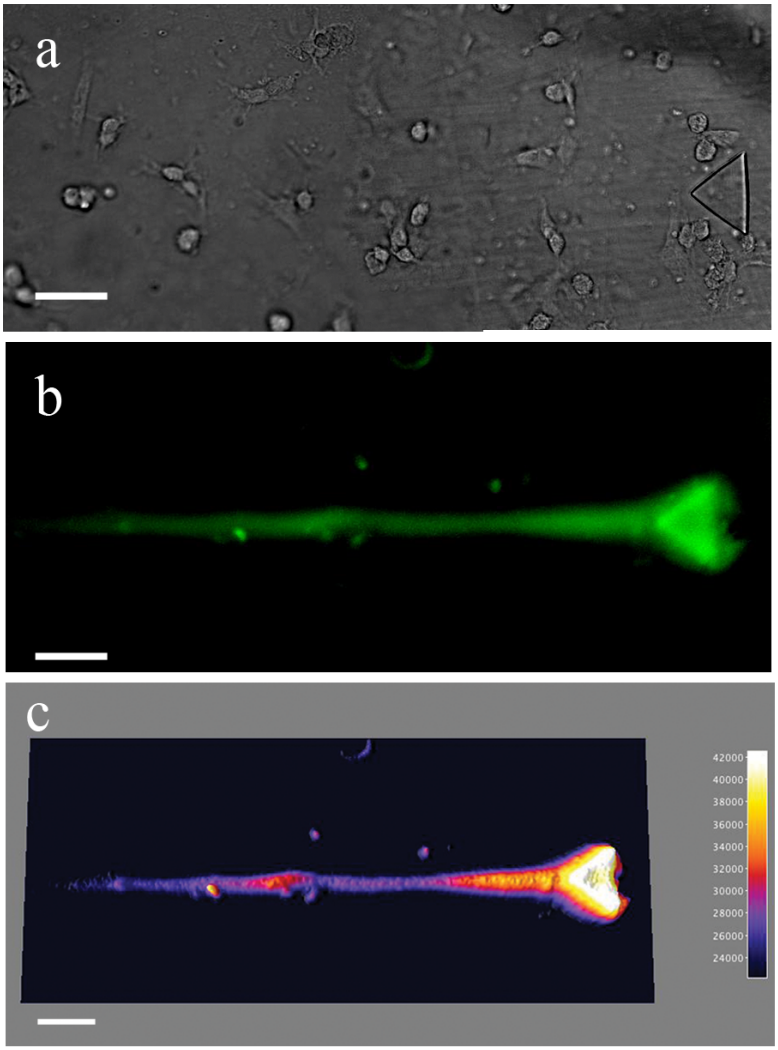

Figure 2.8: Subcellular dosing using sheath flow microstructures. Schwann cells were cultured on a polyimide film after microstructure μ-3D printing within a flow chamber. Schwann cells were dosed with a stream of 5 μM Syto 13 green fluorescent stain and 20 μM fluorescein (for stream visualization). Dye emanates from a pore upstream of the dosed cells so that bulk flow around a triangle-shaped microstructure focuses the stream. (a) The microstructure and cells under wide field illumination before laser ablation (b) Green fluorescence signal from both stained Schwann cells and the dye stream 5 minutes after pore creation. (c) The microstructure and stream are depicted in a fluorescence intensity surface plot. Scale bars represent 50 μm in all images.

An initial funnel design failed to focus the stream in either the z-axis or x-axis according to simulations (Figure 2.9, a). Modeling suggested that peak broadening might be reduced by replacing the large diameter chimney with a narrow, nozzle-shaped exit port (Figure 2.9, c). However, 3D printing and flowing media through these geometries often leads to chimney clogging or leaking due to high back pressures generated by narrow openings. Thus, the inverted funnel design (Figure 2.9, b) was chosen for cell dosing. Stream widths were measured as FWHM at 200 μm downstream of the inlet pore. The y-axis is labeled as the direction of laminar flow, the x-axis as orthogonal to the flow and parallel to bottom of the flow chamber. The z-axis is defined as orthogonal to both the flow direction and the bottom of the flow chamber.

Further analysis of simulation data reveals that the larger diameter opening at the top of the structure retards bulk flow while the narrow diameter base allows relatively faster local flow rates to pass. When the dye stream emerged from the chimney structure it was focused by parallel flow streams above and below, as well as on each side. This allows for highly precise dosing compared to a control stream, as illustrated by the dye concentration maps on the surface of simulated cell somas (Figure 2.10). With μ-3D printing, chimney height could be controlled on-the-fly during cell culture so as to target specific cellular processes. Using methods for *in situ* μ-3D printing discussed in the Chapter 3, the location and chimney design could be chosen minutes before dosing and would allow an experimenter to target a neuron soma without considerable dosing of neighboring dendritic or axonal processes.

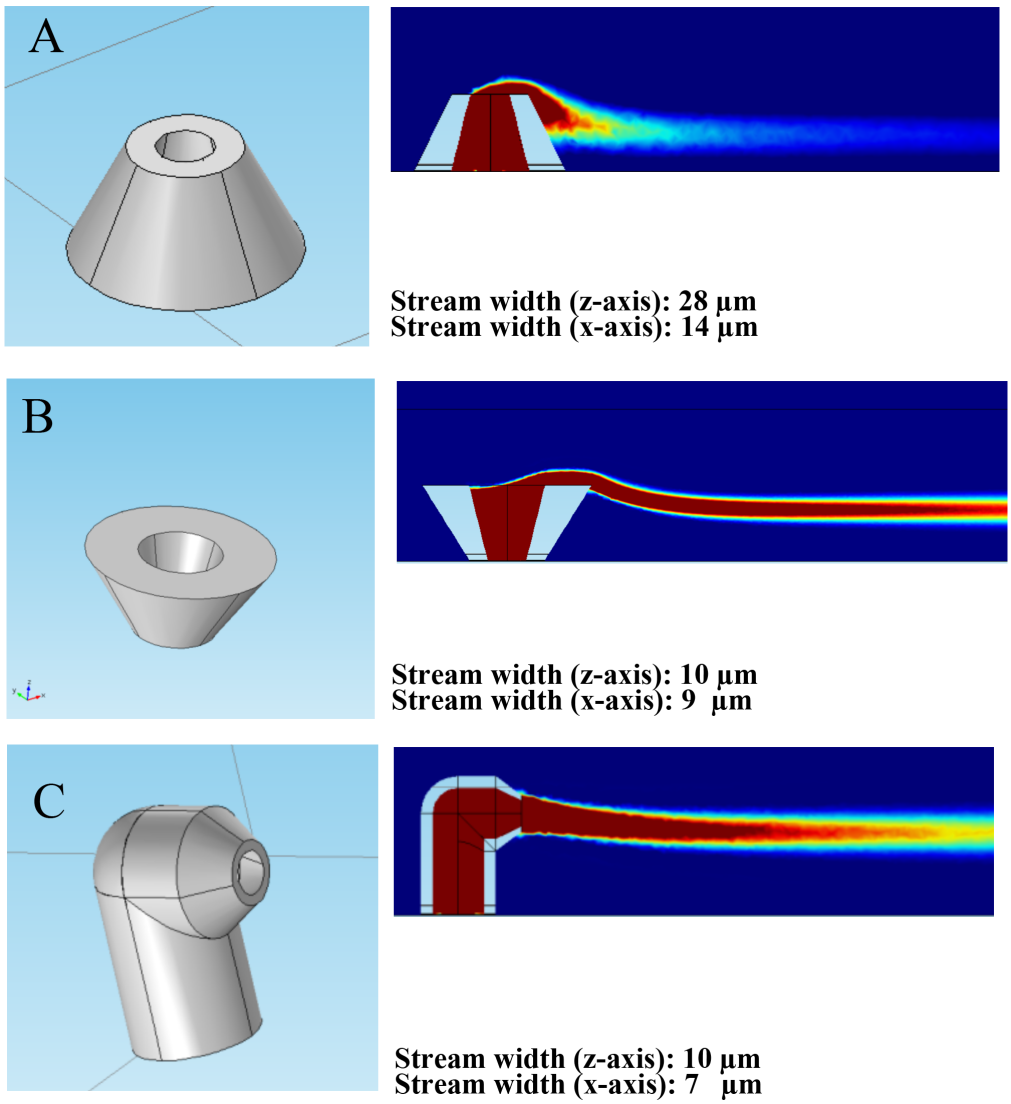

Figure 2.9: Finite element simulations for refinement of chimney geometry. Full-width-half-maximum stream widths are displayed for measurements taken 200 μm downstream of the source. Highest dye concentrations are depicted in red on the longitudinal slice of each 3D model. (a) An inverted-funnel-shaped chimney resulting in poor stream width and little elevation from the surface. (b) A funnel-shaped chimney resulting in decreased stream width and elevated position. (c) A chimney with a nozzle that resulted in minimal stream width but suffered from clogging during experiments.

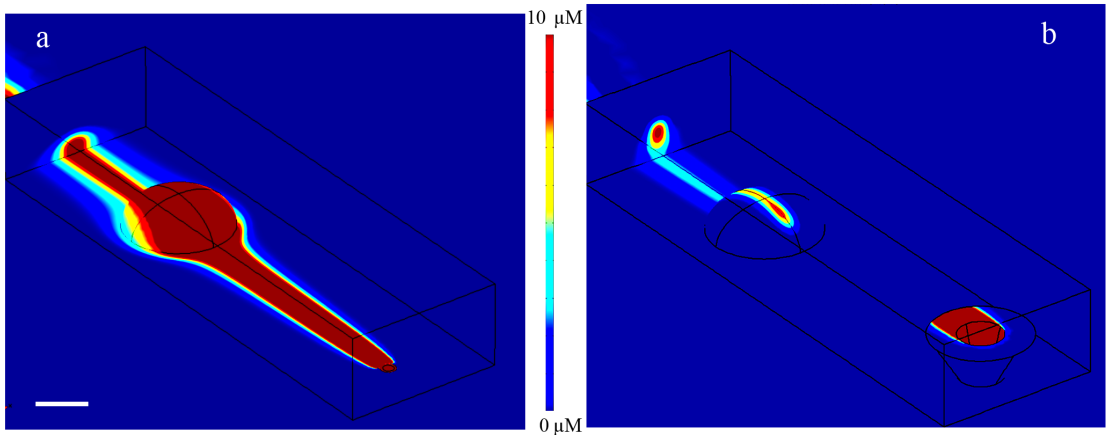

Figure 2.10: μ-3D printed funnel-shaped microstructures for 3D hydrodynamic focusing. (a) Finite element model of a pore and 15 μm tall cell without a structure. (b) Finite element model of a microstructure 40 μm in height directing a stream of dye toward a simulated cell 15 μm in height. Concentration is displayed for the surface of the microstructure and cell in addition to an xz-plane slice 300 μm downstream of the dye source. Scale bar equal to 50 μm applies to both images.

As a demonstration, the height of the chimney was optimized through iterative finite element simulations to deliver dye streams to the dorsal region of the soma of an NG108-15 cell without targeting neurites or basal portions of the cell membrane. The average NG108-15 soma height was determined from confocal microscopy to be 15 μm (Figure 2.11) and a chimney 40 μm in height was μ-3D printed to effectively target the soma. A stream consisting of 1 μM Mitotracker Red CMXRos (for cellular staining) and 75 μM rhodamine B (for stream visualization) was delivered to the cells (Figure 2.12, a).

In order to verify the 3D control of the chimney design, 20 μm tall microstructures were fabricated with a solution of 10 mM Rose Bengal, 20% (v/v) PEGDA, and 9.1% (w/w) BSA in HBS pH 7.4. After removal of uncrosslinked printing solution, 10 μM fluorescein, 20 mM acetate (pH 4) was flowed in a parallel flow chamber, while 200 mM Tris (pH 9) was flowed in the flow chamber in which pipe structures were fabricated (Figure 2.13). Critically, the chimney-shaped focusing allowed for the narrowest stream widths (Figure 2.13, b) and steeper concentration gradients as measured in the horizontal x-axis. Confocal fluorescence microscopy confirms that the stream width is reduced on average 56% (n=3) with a reduction of stream FWHM from 18 μm to 8 μm ($p < 0.023$) when compared to control pores within the same flow chamber (Figure 2.13, c). In comparison to control streams, the z-axis placement was higher and more symmetrical when measured with confocal microcopy (Figure 2.13, a). However, diffusive broadening of the stream within the vertical z-axis dimension appeared greater in the chimney-focused stream as measured by confocal microscopy.

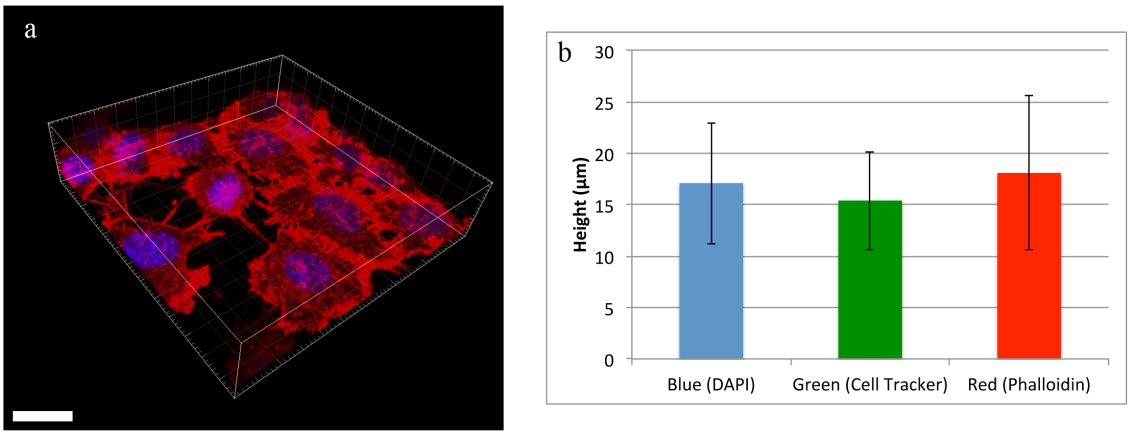

Figure 2.11: Confocal microscopy for cell height measurement. NG108-15 cells were incubated on untreated coverglass with 10% FBS media supplemented as described above. Cells were stained with DAPI, CellTracker Green CMFDA, and Alexa Fluor 568 phalloidin before imaging with a 63x 1.4 NA Zeiss objective with a 1.0 μm z-axis step size. (a) Signal from the DAPI (blue) and phalloidin (red) fluorescence signal were displayed in a 3D projection. Scale bar, 50 μm. (b) Cell height is determined from the point of maximum fluorescence signal in the z-axis for each cell and stain. An average cell height of 15 μm (n=24) is apparent from CellTracker Green, a cytoplasmic stain. Nucleic acid stain (DAPI) and actin stain (phalloidin) displayed heights of 17 μm and 18 μm, respectively (n=24). Error bars represent standard deviation.

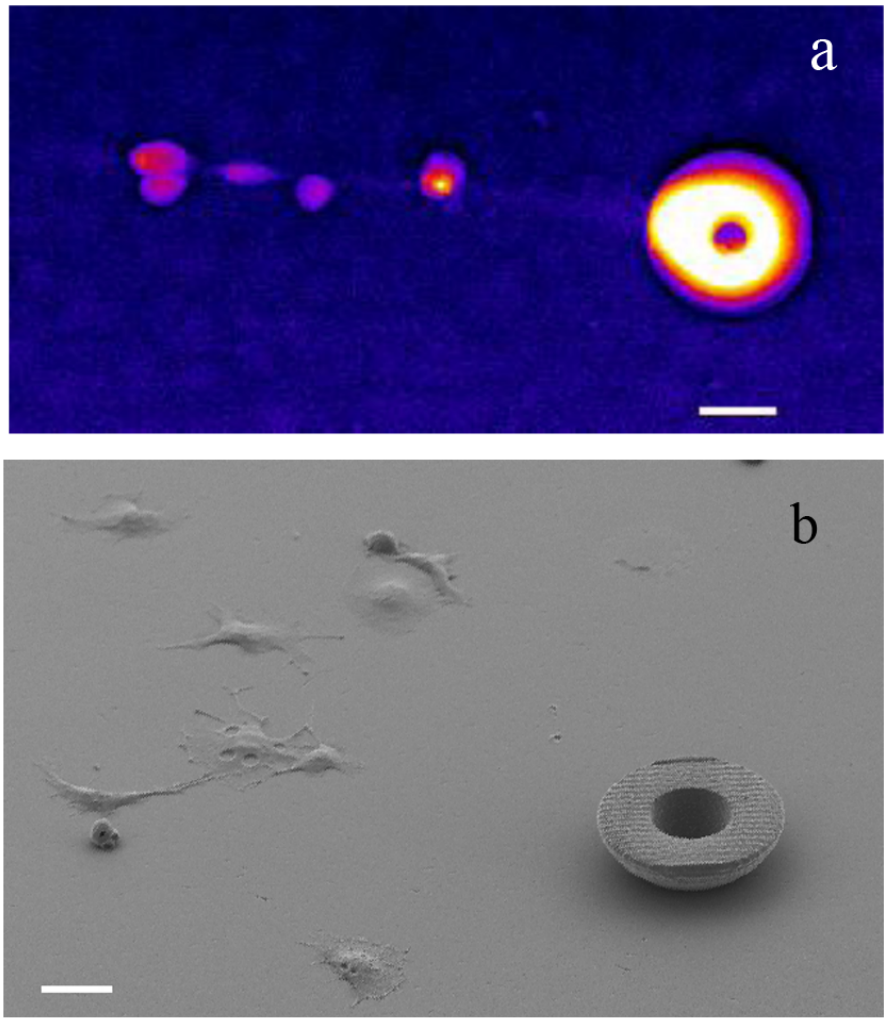

Figure 2.12: 3D cell dosing. (a) NG108-15 cells dosed with a stream consisting of 1 μM Mitotracker Red CMXRos (for cellular staining) and 75 μM rhodamine B (for stream visualization). A color lookup table was applied to the red fluorescence signal imaged with wide field microscopy. Scale bar, 20 μm. (b) A scanning electron micrograph of a representative funnel-shaped PEGDA microstructure 40.5 μm in height 3D printed on polyvinyl before plating NG108-15 cells. The cells were cultured for 3 days before fixing with 5% glutaraldehyde. Scale bar, 30 μm.

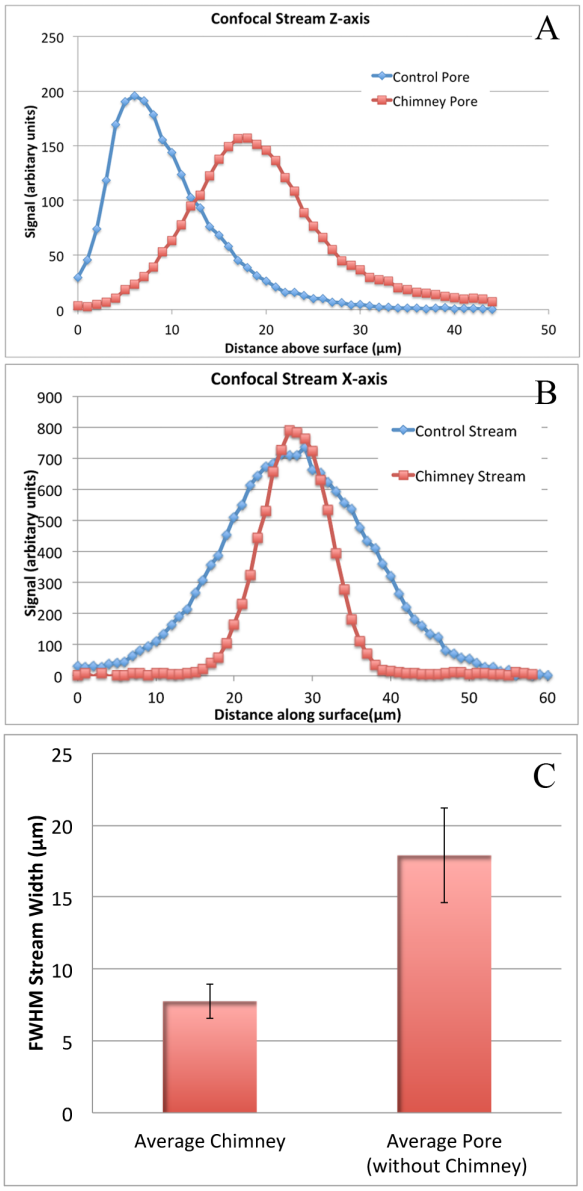

Figure 2.13: Confocal imaging of 3D streams (a) The green fluorescence confocal microscopy signal from streams of 10 μM fluorescein is plotted along the z-axis measured from the surface of the flow chamber. Signal from a stream originating from an unmodified pore is shown for comparison. (b) Green fluorescence confocal microscopy signal is compared along the x-axis for a chimney stream and control stream. (c) The average x-axis stream width as measured by confocal microscopy at the z-axis plane of highest signal is shown for stream originating from within a chimney and those without a chimney (n=3). Error bars represent standard error ($p < 0.023$).

2.3.5 Laser Ablation

Laser ablation of the polyimide film does not appear to occur at sub-threshold laser intensity. By modulating the laser intensity during μ-3D printing, ablation can be avoided while still achieving high enough intensities for the multiphoton excitation necessary for printing. This threshold intensity was calculated as 1.3 TW/cm^2 assuming a Gaussian focus with a 1.4 NA objective, 740 nm laser light, 80% objective transmittance, 150 fs pulse width, 76 MHz cycle, and 30 mW measured at the back aperture of the objective. This intensity was calculated from a beam waist of 322 nm and peak power of 2.6 kW, assuming a Gaussian profile.

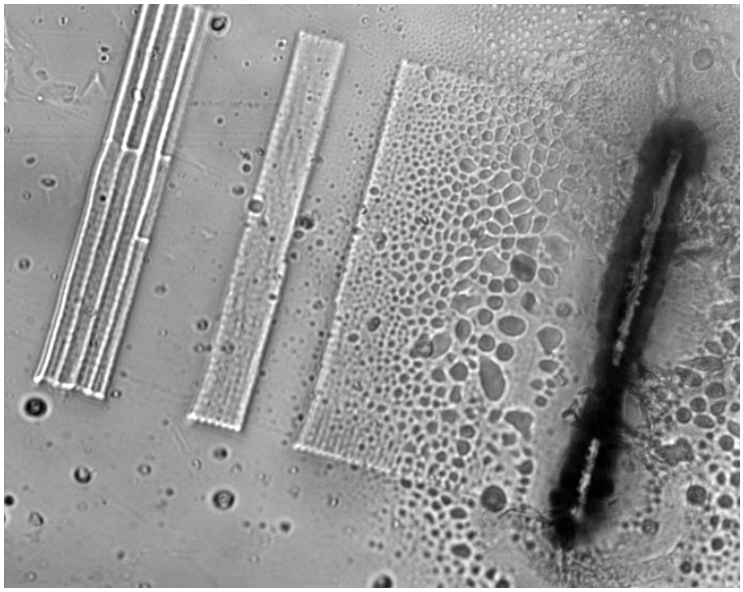

Figure 2.14: Ablation of polyimide during μ-3D printing. A solution of 6.4 mM Rose Bengal, 4% (w/v) BSA, 20% (v/v) PEG (700 Da) was μ-3D printed on polyimide film using a 40x, 0.60 NA Nikon objective. The Ti:Sapphire laser power was maintained at 40 mW and scan speed 50 μm/s. Although the z-axis stage position was unchanged, slight changes in focal distance resulted in ablation of the polyimide during scanning.

Although the z-axis stage position was controlled by a nano-positioning system during printing, slight changes in z-axis position may have occurred during x-axis scans, resulting in ablation of the polyimide. The change in the z-axis position may have been due to unlevel mounting of the entire substrate by only a few micrometers. Therefore, careful control of the focal plane of the laser must be maintained to avoid ablation during printing (Figure 2.14).

In contrast, when ablation was desired for cell dosing purposes it failed in some instances (Figure 2.15). When focused light from an Nd:YAG laser (532 nm) struck the polyimide barrier, functional pores did not form, possibly due to sub-threshold laser fluence delivered to the polyimide film. 3D printed structures may reduce the failure rate by allowing high laser fluence and confining stream width downstream of the resulting larger pore. Increasing the laser power from 10 to 20 mW has been shown to increase the success rate from 23% to 87% for a 40x, 0.75 NA objective. However, higher laser intensity results in larger pore sizes measured by SEM. A larger diameter pore creates a larger stream width (Figure 2.16). In fact, doubling of laser power results in nearly double the stream width (15 to 29 μm).

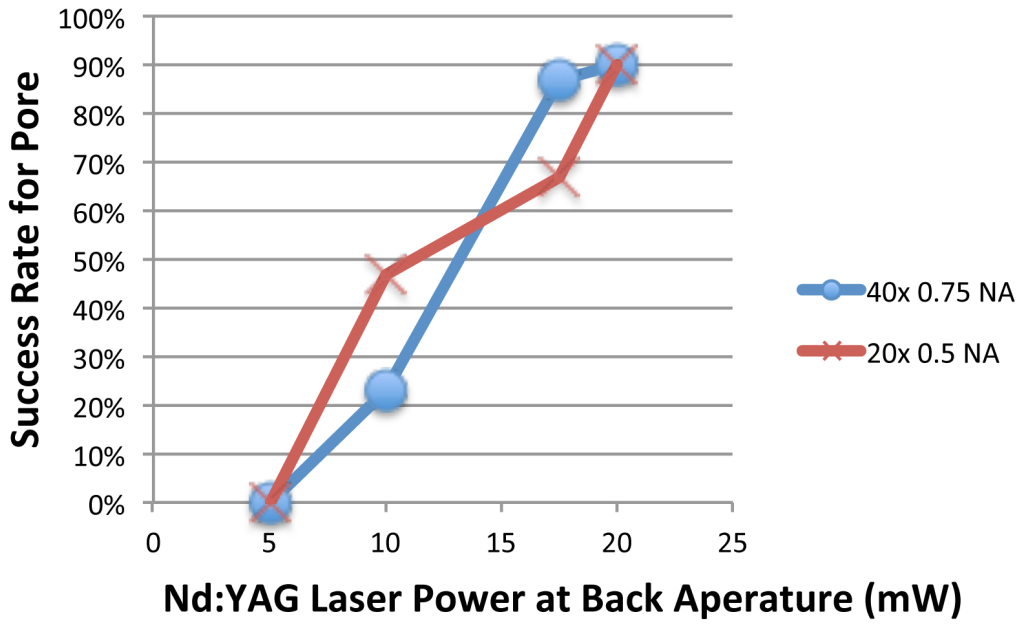

Figure 2.15: Pore creation was dependent on the threshold phenomenon of ablation. Partially ablated pores may form at lower laser intensity, resulting in apertures too narrow for fluid flow at given pressure gradients. Success rate for each pore was determined by imaging of 10 μM fluorescein dye streams emitted from pores (n= 10 or greater for each objective and laser power). Ablation was achieved with a 20x 0.5 NA and a 40x 0.75 NA Zeiss objective under-filled by a Nd:YAG (532 nm) laser light, as previously described.

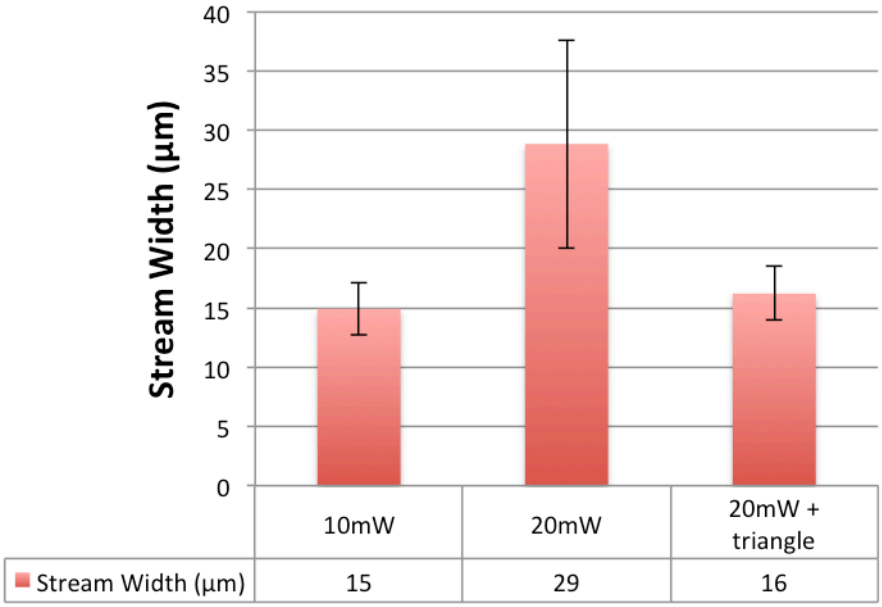

Figure 2.16: Stream width due to ablation power and microstructure. Stream width was determined from 10 µM fluorescein dye streams emitted from pores (n =5 for each condition). Nd:YAG laser power at the back aperture was varied for the 10 mW and 20 mW streams. 3D printed triangles within the same flow chamber were used to focus streams from pores ablated with 20 mW. Error bars represent standard deviation for each condition, $p < 0.008$ for a t-test comparing 20 mW pores and 20 mW pores with a triangle.

The increase in pore diameter can be compensated if a sheath flow triangle is μ-3D printed downstream, reducing the average stream width down to 16 μm (Figure 2.16). This technique allows for lower failure rates without compromising cell dosing resolution. Furthermore, inexpensive lower quality optics or lasers could be used to ablate larger pores with smaller streams if these were the best tools available to researchers.

2.4 CONCLUSION

The techniques described in this chapter provide methods to reduce the dosing stream width and control the 3D profile of a reagent while dosing a cultured cell. These goals were achieved by developing a novel method of μ-3D printing within the microfluidic flow system. Refinement of the printed structure geometries using finite element modeling allows the possibility of placing dosing streams at a range of heights with narrowly focused dimensions. These advancements will allow future experiments including tracking neutrophil receptor expression with 3D specificity and higher dosing precision. The use of μ-3D printing structures allows users with lower quality optics or lasers to ablate larger pore sizes but still obtain narrow stream widths. These advancements should allow the dosing system to find new applications and users.

Future improvements to the geometry of 3D dosing chimneys are possible through the refinement of finite element models. With advances in computing power and lower costs for hardware, 3D models with submicron resolution should be possible in the near future. These models would allow the refinement of the hydrodynamic focusing geometry to create streams narrower than 6 μm. Additional improvements may be possible using materials with greater tensile strength or higher surface adhesion when μ-3D printed, such as acrylic resins. However, the toxicity of materials must be considered for applications with cultured cells. Chapter 3 discusses the use of protein-photoinitiator conjugates so that structures can be placed on-the-fly within microns of culture cells without significant effects to cell viability or morphology.

2.5 REFERENCES

1. Weiner, O. D. *et al*. Spatial control of actin polymerization during neutrophil chemotaxis. *Nature Cell Biology* **1**, 75–81 (1999).
2. Atkinson-Leadbeater, K. *et al*. Dynamic expression of axon guidance cues required for optic tract development is controlled by fibroblast growth factor signaling. *Journal of Neuroscience* **30**, 685–693 (2010).
3. Kumar, A. *et al*. CXCR4 Physically Associates with the T Cell Receptor to Signal in T Cells. *Immunity* **25**, 213–224 (2006).
4. Kratchmarova, I., Blagoev, B., Haack-Sorensen, M., Kassem, M. & Mann, M. Mechanism of Divergent Growth Factor Effects in Mesenchymal Stem Cell Differentiation. *Science* **308**, 1472–1477 (2005).
5. Gómez-Moutón, C. *et al*. Dynamic redistribution of raft domains as an organizing platform for signaling during cell chemotaxis. *Journal of Cell Biology* **164**, 759–768 (2004).
6. Boyer, C., Schikorski, T. & Stevens, C. F. Comparison of Hippocampal Dendritic Spines in Culture and in Brain. *Journal of Neuroscience* **18**, 5294–5300 (1998).
7. Nielson, R. & Shear, J. B. Parallel chemical dosing of subcellular targets. *Analytical chemistry* **78**, 5987–5993 (2006).
8. Hoppe, T. J., Moorjani, S. G. & Shear, J. B. Generating Arbitrary Chemical Patterns for Multi-Point Dosing of Single Cells. *Analytical chemistry* (2013).
9. Celedon, A. *et al*. A distinctive role for focal adhesion proteins in three-dimensional cell motility. *Nature Cell Biology* **12**, 598 (2010).
10. Cukierman, E., Pankov, R., Stevens, D. R. & Yamada, K. M. Taking Cell-Matrix Adhesions to the Third Dimension. *Science* **294**, 1708–1712 (2001).
11. Denk, W. Two-photon scanning photochemical microscopy: mapping ligand-gated ion channel distributions. *PNAS* **91**, 6629–6633 (1994).
12. Soeller, C. & Cannell, M. B. Two-photon microscopy: imaging in scattering samples and three-dimensionally resolved flash photolysis. *Microscopy Research and Technique* **47**, 182–195 (1999).
13. Klauke, N., Smith, G. & Cooper, J. M. Microfluidic systems to examine intercellular coupling of pairs of cardiac myocytes. *Lab on a Chip* **7**, 731–739 (2007).
14. Wang, G. X. & Poo, M. Requirement of TRPC channels in netrin-1-induced chemotropic turning of nerve growth cones. *Nature* **434**, 898–904 (2005).

15. Nauen, D. W. & Bi, G.-Q. Measuring action potential-evoked transmission at individual synaptic contacts. *Journal Neural Engineering* **9**, 036014 (2012).

16. Moorjani, S., Nielson, R., Chang, X. A. & Shear, J. B. Dynamic remodeling of subcellular chemical gradients using a multi-directional flow device. *Lab on a Chip* **10**, 2139–2146 (2010).

17. Tibbitt, M. W. & Anseth, K. S. Hydrogels as extracellular matrix mimics for 3D cell culture. *Biotechnology and Bioengineering* **103**, 655–663 (2009).

18. Fairbanks, B. D., Schwartz, M. P., Bowman, C. N. & Anseth, K. S. Photoinitiated polymerization of PEG-diacrylate with lithium phenyl-2,4,6-trimethylbenzoylphosphinate: polymerization rate and cytocompatibility. *Biomaterials* **30**, 6702–6707 (2009).

19. Martin, M. M. & Lindqvist, L. The pH dependence of fluorescein fluorescence. *Journal of Luminescence* **10**, 381–390 (1975).

20. Kleitman, N., Wood, P. M. & Bunge, R. P. Tissue culture methods for the study of myelination. *Culturing Nerve Cells* 337–377 (1991).

21. Suri, S. & Schmidt, C. E. Cell-Laden Hydrogel Constructs of Hyaluronic Acid, Collagen, and Laminin for Neural Tissue Engineering. *Tissue Engineering Part A* **16**, 1703–1716 (2010).

22. Galambos, P. & Forster, F. K.in *Micro Total Analysis Systems* (Harrison, D. J. & Berg, A. van den) 189–192 (Springer Netherlands, 1998).

23. Lee, G.-B., Chang, C.-C., Huang, S.-B. & Yang, R.-J. The hydrodynamic focusing effect inside rectangular microchannels. *Journal of Micromechanics and Microengineering* **16**, 1024 (2006).

Chapter 3: *In situ* μ-3D Printing for Biological and Microfluidic Applications

3.1 Introduction

To allow for on-the-fly cell dosing with high precision, μ-3D printed structures need to be placed within approximately 100 μm of a cultured cell without affecting the cell in any substantial way. The main limitation of μ-3D printing within cell cultures is the known cytotoxicity of many of the reagents used. As discussed in Chapter 1, photosensitizers used to initiate μ-3D printing reactions can have deleterious effects on living cells.

Both Type I photosensitizers, such as flavin adenine dinucleotide (FAD), and Type II photosensitizers including Rose Bengal, eosin, and methylene blue have been used successfully for μ-3D printing by Shear group members [1][2][3]. Type I photosensitization occurs via excitation of the photosensitizer molecule to a triplet state capable of generating free radicals through hydrogen abstraction of an oxidizable species [4]. Type I photosensitizers have significantly lower crosslinking efficiency and require either higher laser power or longer dwell times than Type II photosensitizers. These limitations make Type I photosensitizers unsuitable for creating complex 3D structures [5].

Type II photosensitizers generate singlet oxygen ($^1O_2$) which can promote efficient chemical crosslinking. However, Type II photosensitizers must be used carefully with cultured cells due to the ability of singlet oxygen to cause cell death by reacting with proteins, lipids, and nucleic acids [6]. The lifetime of singlet oxygen in cells is estimated to be ~50 μs with a diffusion length of ~100 μm when created in the nucleus of a neuron via laser light [7]. Therefore, the generation of singlet oxygen must be carefully contained when μ-3D printing within the presence of cells.

To prevent any single oxygen generation within cells, Todd Hoppe conjugated the small eosin molecule (648 Da) to much larger gelatin fragments (~50 kDa). Eosin can no longer cross the cell membrane and enter the cytoplasm once bound to a molecule as large as gelatin. This experiment demonstrated that Type II photosensitizer-protein conjugates may be used to μ-3D print cages around mammalian cells with minimal toxic effects and a 79% survival rate [3]. Furthermore, the walls of the μ-3D printed cages were printed within 10 μm of living cells and very little cytotoxicity was observed from this process. This chapter demonstrates that with lower molecular weight gelatin and properly buffered printing solutions, *in situ* μ-3D printing can be achieved in a microfluidic dosing platform, as a means improve the cell dosing precision.

3.2 Experimental Methods

3.2.1 Chemicals and reagents

Leibovitz (L-15) medium (SH30525) was purchased from HyClone (Logan, Utah). LIVE/DEAD® Viability/Cytotoxicity Kit (L3224) was purchased from Molecular Probes (Eugene, OR). The kit contained 4 mM Calcein AM (live stain) in anhydrous DMSO and 2 mM Ethidium homodimer-1 (dead stain) in DMSO/H_2O 1:4 (v/v). A staining solution of 1 μM Calcein AM and 2 μM Ethidium homodimer-1 was created by diluting stock solutions with Dulbecco's phosphate buffered saline. Bovine serum albumin (BSA; BAH64) was purchased from Equitech-Bio (Kerrville, TX). Eosin-5-isothiocyanate (E-18) was purchased from Molecular Probes (Eugene, OR). Type A gelatin (Bloom number ~300) from porcine skin (G2500) and L-ascorbic acid (95210) were purchased from Sigma-Aldrich (St. Louis, MO). Type A gelatin (Bloom number ~60) from porcine skin (16560) was purchased from Electron Microscopy Sciences (Hatfield, PA).

3.2.2 Cell Culture

HL-60 cells, a neutrophil precursor cell line, were cultured in RPMI-1640 (22400) supplemented with 10% (v/v) fetal bovine serum (FBS, 10082), both purchased from Invitrogen. Flasks were maintained at 37 °C in a 5% CO_2 atmosphere and diluted 1:10 in fresh media once per week. HL-60 cells are not adherent to polystyrene flasks and have a doubling time of 36-48 hours. All HL-60 cells used in this dissertation were provided by Dr. O. D. Weiner (Department of Biochemistry, University of California at San Francisco).

Rat Schwann cells (RSC) isolated from neonatal Sprague-Dawley rat sciatic nerves were donated by Shalu Suri and Christine Schmidt (University of Texas at Austin; Austin, TX). The isolation of RSC from rat tissue is described in detail in Chapter 2. RSC were cultured in DMEM media with 10% (v/v) fetal bovine serum (FBS), 30 mg/mL bovine pituitary extract, and 2 mM forskolin. To passage, all media was removed from the culture flask and the cells were incubated in 0.25% trypsin, 0.53 mM EDTA, and Hank's buffered salt solution (MediaTech) for 5 minutes before quenching with culture media.

For cell viability experiments the cells were resuspended at 1 x 10^6 cells/mL in culture media and incubated at 37 ° C for 3-7 days within the microfluidic device before μ-3D printing. The partially assembled flow chamber apparatus was incubated in a solution of 30% ethanol/water, 1.0 mg/mL rat-tail collagen (354249, BD Biosciences) overnight. The flow chamber was then equilibrated with 20 injections of 100 μL of culture media before seeding with RSC.

To control temperature within the microfluidic device an environmental chamber was placed around the flow chambers and positioned on the microscope stage. The environmental chamber was constructed from 6.3-mm plexiglass for the walls and lid,

with a 1.6-mm-thick aluminum base fit to a Prior stage insert. Beneath the chamber a conductive heating element (Brook Industries) was used to maintain the stage temperature. Additionally, air was heated and forced into the environmental chamber with a heat gun (Westward, 4HWK1), 3.8-cm-diameter polyethylene tubing, and a fan. The heat gun was cycled on and off to maintain a set temperature with a thermocouple and PID controller (Red Lion, T1620000). The relative humidity was increased to prevent evaporation of small volumes of reagent by placing a dish of distilled water within the chamber.

3.2.3 Protein-photosensitizer Conjugation

Eosin-5-isothiocynate (a Type II photosensitizer) was conjugated to proteins (BSA and gelatin) using a standard amine labeling protocol. A solution of 10 mg/mL protein solution in 100 mM sodium bicarbonate buffer (pH 9) was combined with a solution of 10 mg/mL eosin-5-isothiocyanate in DMSO in a 10:1 (v/v) ratio. After mixing for 24 hrs, the solution was dialyzed with a cellulose ester dialysis cassette (8-10 kDa molecular weight cutoff) (G235067; Spectrum Laboratories, Inc.) in 3 L of 100 mM sodium bicarbonate buffer (pH 9) for 48 hrs. To remove residual salts, the protein-photosensitizer solution was dialyzed in deionized water for 24 hrs before lyophilization at -50°C and 0.10 mbar for ~72 hours in a FreeZone® 4.5-liter benchtop freeze dry system (Labconco Corp., Kansas City, MO).

3.2.4 μ-3D Printing

Micro-three-dimensional printing (μ-3D printing) was performed using a mode-locked Ti:sapphire laser tuned to 740 nm with a pulse duration < 130 fs and repetition rate of 76 MHz (Coherent, Mira 900F). Photomasks were displayed using the SVGA graphics output of a desktop computer displayed on an 800 x 600 pixel digital

micromirror device (DMD) (BenQ, MP510) capable of modulating each mirror ~20° when switched from a white to black graphical input. Dual-axis galvanometer scan mirrors (Thor Labs) were used to raster the beam at 50 mHz and 100 Hz across the x- and y-axis, respectively. A series of relay lenses were used to focus the beam onto the DMD and collimate the beam into the back aperture of a 60x, 1.4 NA objective within a Nikon inverted microscope. The z-axis position was dictated by a digital piezo controller and multi-axis nanopositioning system with capacitive sensors (Physik Instrumente, E-710). Control of the stage, scan mirrors, and DMD was synchronized using custom routines created in LabView™ (National Instruments). Photomasks were displayed at each z-axis position and updated during z-axis steps while the raster scan was at a terminal position. The DMD photomask system was placed conjugated to the plane of printing, so that each mask corresponded to a single layer of printing. Laser power at the objective back aperture was attenuated to 22-30 mW with a beam splitting cube and half-wave plate.

To achieve μ-3D printing within a microfluidic device, 40 μL of printing solution was pipetted into the flow chamber and the polyimide film placed on #1 coverglass for printing with an oil immersion Nikon 60x, 1.4 NA microscope objective. When noted, μ-3D printing within the microfluidic device was achieved by partially assembling the device and filling the upper flow chamber with printing solution before mounting on a #1 glass coverslip. Excess printing solution was washed out of the flow chamber using L-15 media containing 10% (v/v) fetal bovine serum (FBS).

3.3 Results and Discussion

3.3.1 BSA-eosin Conjugation

To enable on-the-fly placement of μ-3D printed objects for cellular dosing, a method of printing *in situ* without toxic effects to cultured cells was explored. Initially, a

protocol developed by Todd Hoppe was followed, calling for gelatin Type A (Bloom number 200) conjugated to eosin to be used for μ-3D printing. Gelatin Type A (Bloom number 200) at concentrations greater than 200 mg/mL forms a hydrogel at room temperature and a very high viscosity fluid (> 150 cP) when heated above 35-40 °C. The high pressure required for the removal of high viscosity printing solutions containing gelatin necessitated the replacement of gelatin Type A (Bloom number 200) with another protein for use in microfluidics. BSA remained at a low enough viscosity that it could be flowed into a microfluidic device even at high concentrations (> 200 mg/mL) and low temperatures (< 20 °C). Solutions consisting of BSA, PEGDA, and Rose Bengal were used to μ-3D print robust structures within microfluidic chambers (Chapter 2). However, the presence of free Rose Bengal in solution resulted in apparent apoptosis of cultured HL-60 cells (Figure 3.1).

To determine the effects of Rose Bengal and PEGDA on cell viability, HL-60 cells were incubated in a solution containing each for 60 minutes. Although staining with Trypan Blue showed no cells with compromised membranes, cell size appeared to reduce after incubation with either 5 mM Rose Bengal or 10% (v/v) PEGDA. This may have been due to hypertonic solutions created by high concentrations of solutes added to an isotonic cell culture media (L-15). However, Apoptosis (programmed cell death) also proceeds by a reduction in cell volume and hypertonic solutions have been shown to cause both apoptosis and necrosis in mammalian cell lines [8]. Therefore it is difficult to determine the pathway of cell shrinking without specific stains for apoptotic markers.

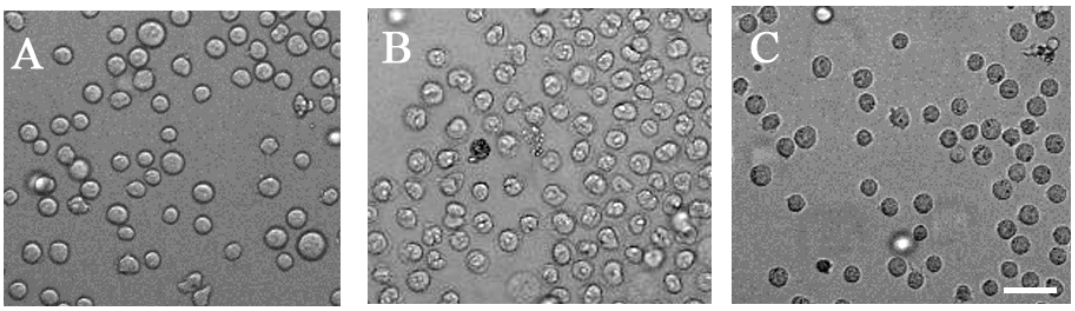

Figure 3.1: Printing solution cell viability testing with HL-60 cells. (a) Control sample plated in standard cell culture media for 60 min. (b) HL-60 cells incubated with standard media supplemented with 5 mM Rose Bengal. (c) HL-60 cells incubated with standard media supplemented with 10% PEGDA. Scale bar, 25 μm.

In order to reduce the osmolality of the printing solution and prevent uptake of photosensitizer by cells, eosin-5-isothiocynate (a type II photosensitizer) was conjugated to BSA. The amine-reactive eosin-5-isothiocynate forms a stable covalent bond with the ε-amine of lysine residues [9]. The BSA molecule has a molecular weight of 67 kDA with 59 lysine residues [10], while gelatin Type A fragments range in size but have a lysine residue at 2.7% of all residues [11]. Therefore, there are ~10 lysine residues per 50 kDa fragments of gelatin (Bloom number ~200). Thus, BSA exhibits a significantly higher number of lysine residues per fragment than gelatin of similar molecular weight. However, BSA exhibits a highly ordered tertiary protein structure with large hydrophobic regions where 32-37 of the 59 lysine residues are inaccessible to aqueous reagents [12].

Eosin was conjugated to BSA, the reaction solution was dialyzed and lyophilized, and the product was tested for reaction yield by absorbance at 630 nm of reconstituted samples. Although pure solutions of eosin exhibit a maximal absorbance at 520-530 nm, solutions of eosin-BSA conjugates show reduced absorption at 520 nm and increased absorption between 590 and 690 nm. This phenomenon has also been recorded for

eosin–ovalbumin conjugates by other researchers [13]. Furthermore, eosin that is not covalently bonded to BSA may be retained within the hydrophobic pockets of the BSA molecule. This effect has been shown to red shift the absorption spectrum of eosin-human serum albumin solutions [14]. A standard curve for free eosin in concentrations between 1 and 7 mM in a solution with 192 mg/mL BSA resulted in a molar extinction coefficient of 31 M^{-1} cm^{-1} at 630 nm (Figure 3.2). Using this standard curve, the product was found to have 6% (w/w) eosin/BSA and ~3 molecules of eosin per molecule of BSA in the product. This compares closely with a reported ~5 eosin molecules per gelatin fragment by Todd Hoppe [3].

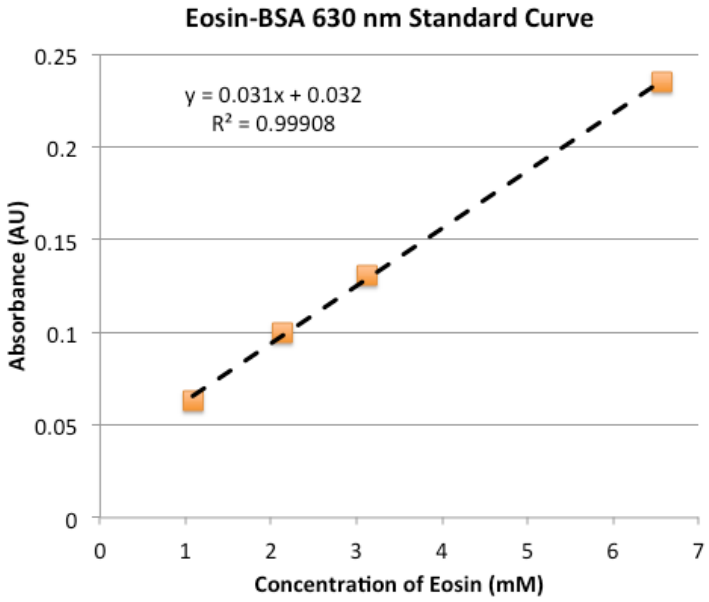

Figure 3.2: Eosin-BSA standard curve. Solutions with variable amounts of eosin were made with 192 mg/mL BSA per solution. A blank containing only 192 mg/mL eosin was used. The absorption (AU) for each sample at 630 nm is plotted.

Eosin-BSA conjugates proved to be useful in creating robust μ-3D printed structures, but Schwann cell death was apparent after printing (Figure 3.3). Ascorbate (Vitamin C) was used as an antioxidant both before and after μ-3D printing, but almost every Schwann cell imaged appeared to undergo apoptosis or necrosis within 1 hour of printing. Compared to eosin-gelatin conjugates, eosin-BSA is a liquid at room temperature, possibly allowing for higher diffusivity of singlet oxygen. Gelatin hydrogels exhibit a diffusion coefficient of only 0.25×10^{-10} m^2s^{-1} for water at 25 °C [15]. Oxidative stress by singlet oxygen diffusion may damage the cells during printing. Furthermore, BSA allows non-covalent binding of eosin more readily than gelatin. Eosin forms an electrostatic complex with BSA with a reduced binding affinity at pH values lower than 9 [16]. When the eosin-BSA conjugate was reconstituted in a neutral pH solution it may have released eosin into the printing solution. As demonstrated in Figure 3.1, free photosensitizer in solution can be toxic to cells.

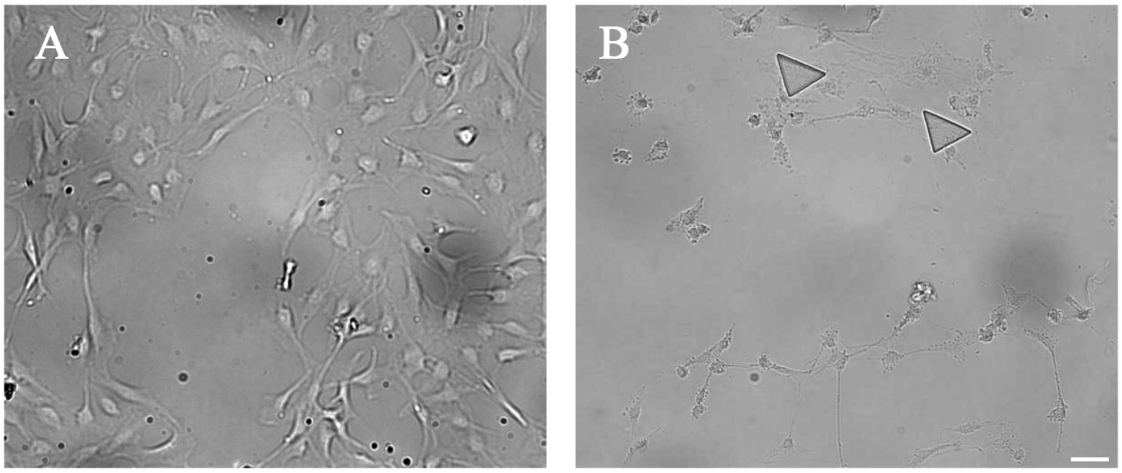

Figure 3.3: μ-3D printing with eosin-BSA conjugates. (a) Schwann cells imaged after incubation overnight in 50 μM ascorbate and 10% FBS in DMEM media before application of printing solution. (b) The same region is imaged immediately after printing two triangles (20 μm in height) from a solution of 200 mg/mL eosin-BSA and washing printing solution away with 10% FBS in L-15. Scale bar, 50 μm.

3.3.2 Acidity of Printing Solutions

The cytotoxicity of printing solutions was further investigated using a pH probe to measure the pH of printing solutions after the addition of soluble protein. The addition of 55 mg/mL BSA to 1.8 mM phosphate buffered L-15 media (pH 7.20) resulted in a modest acidification of the solution by ~0.2 pH units (Figure 3.4). However, the subsequent addition of 173 mg/mL gelatin Type A to the BSA solution resulted in an acidification of 1.7 pH units. To prevent cytotoxic effects of the acidic solution, the pH was titrated to 7.20 using 2 M NaOH, resulting in a 35 mM increase in NaOH concentration in the printing solution. All printing solutions in this chapter were neutralized to a final concentration of 35 mM NaOH to ensure neutral pH and minimize cell toxicity. However, pH probe measurements were not possible with eosin-gelatin

conjugates due to the high cost of reagents. Instead, the addition of 35 mM NaOH was assumed equivalent to titrating to neutral pH after the addition of BSA and gelatin.

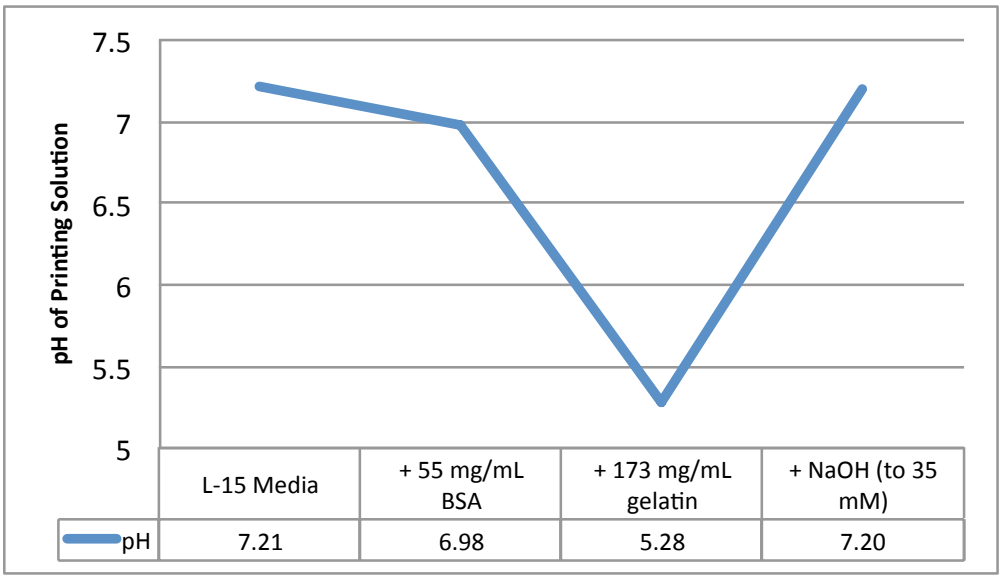

Figure 3.4: Printing solution pH titration. Stepwise additions of protein (BSA and gelatin Type A) resulted in acidification of the printing solution. Although 1.8 mM phosphate L-15 media is buffered, protein additions lower the solution pH and 2 M NaOH was used to titrate the solution to pH 7.20. The final concentration of NaOH in the μ-3D printing solution was 35 mM.

3.3.3 Eosin-gelatin Conjugation

Eosin-gelatin conjugates were explored after observing the poor cell viability of eosin-BSA conjugates. To create a solution compatible with a cell culture device, gelatin with a lower molecular weight and bloom number was conjugated to eosin. Bloom number is a measure of the strength of gelatin hydrogels, with higher Bloom number corresponding to a higher average molecule weight of gelatin fragments. Above the melting point of gelatin (35-40 °C), lower Bloom number gelatin solutions exhibit lower viscosity at equivalent concentrations in comparison to higher Bloom number gelatin

solutions [17]. Previous work by Todd Hoppe used gelatin-eosin conjugates with a gelatin Bloom number of 300 (50-100 kDa). This work was done in cell culture dishes and the uncrosslinked printing solution was removed by diffusion over several hours in warm media [3]. For application to a flow chamber, gelatin with bloom number 60 (20-25 kDa) was conjugated to eosin and reconstituted in a printing solution with additional gelatin of the same bloom number. All gelatins described here are of Type A and derived from porcine skin by acid treatment.

Eosin-gelatin (Bloom number 60) was created using the protein-photosensitizer conjugation method described in section 3.2.3. The conjugate was reconstituted in L-15 buffer and titrated with 2M NaOH to create a solution of 58 mg/mL eosin-gelatin, 86 mg/mL gelatin, and 49 mg/mL BSA. This solution was applied to Schwann cells that were cultured on glass for 3 days in 10% FBS, DMEM media in a CO_2 incubator. All of the media was removed by aspiration before applying ~40 μL of printing solution to the cultured cells. After printing a 20 μm tall triangle within microns of several Schwann cells, 3 mL of 10% FBS, L-15 media was added to the glass-bottom culture dish and the printing area imaged (Figure 3.5). The result was promising; the eosin-gelatin printing solution was highly successful in creating triangle-shaped structures within microns of cells without apparent harm to cell morphology.

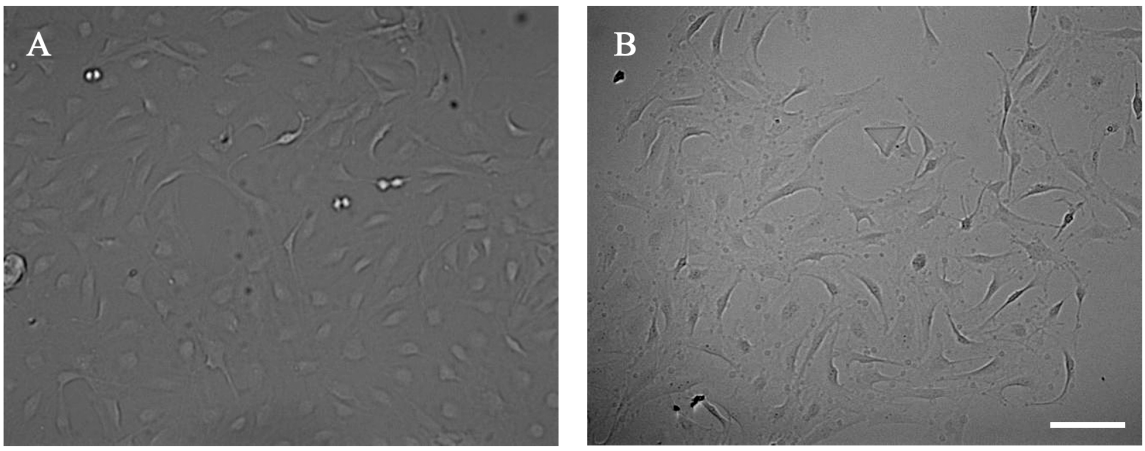

Figure 3.5: Cell viability during *in situ* μ-3D printing. (a) Before μ-3D printing Schwann cells were cultured on glass for 3 days in 10% FBS DMEM media. (b) Cells were imaged immediately after μ-3D printing with a solution of 58 mg/mL eosin-gelatin (Bloom number 60), 86 mg/mL gelatin (Bloom number 60), and 49 mg/mL BSA and washing with 10% FBS L-15 media. Scale bar, 100 μm.

To better understand if the printing process resulted in immediate or lasting effects to cell morphology or viability, cells were imaged overnight at 37 °C within an environmental chamber after μ-3D printing. Triangles (20 μm in height) were printed within microns of Schwann cells and monitored for 18 hours using time-lapse microscopy (Figure 3.6). The gelatin/BSA microstructure appeared to begin to degrade after 90 minutes at 37 °C. This property may reduce the ability to control the dosing streams for experiments longer than 90 minutes, but could also be exploited for timed release of cells from μ-3D printed cages. All cells imaged during this time were motile and several underwent mitosis within 500 μm of μ-3D printed structures, suggesting that cell viability was generally unharmed due to printing. Although the mitosis rate was about 1 in 50 cells, this is not a large deviation from the reported doubling time for Rat Schwann Cells of 3-7 days in culture [18].

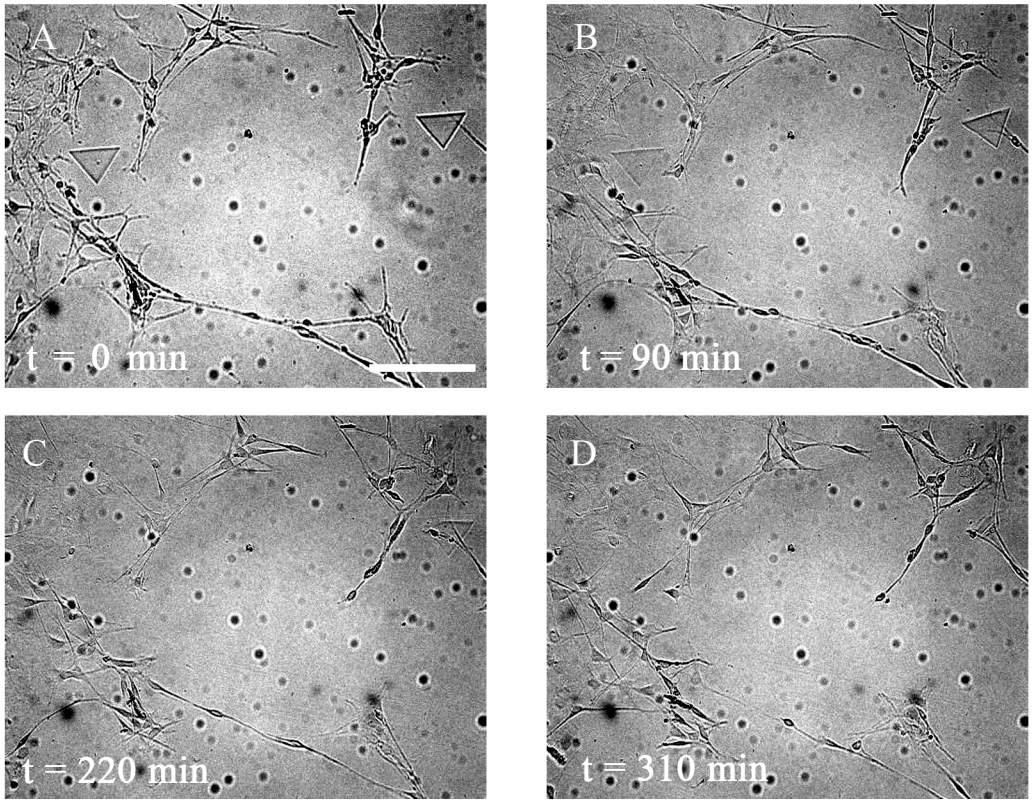

Figure 3.6: Cell viability after *in situ* μ-3D printing. Schwann cells were plated on glass and cultured for 10 days before use. A printing solution of 58 mg/mL eosin-gelatin (Bloom number 60), 86 mg/mL gelatin (Bloom number 60), and 49 mg/mL BSA was added after removal of culture media. (a) Triangles within 10 μm of cells are shown immediately after the printing solution was removed and replaced with 10% FBS L-15 media. (b) 90 minutes after the printing solution was removed the triangles begin to degrade. (c) 220 minutes after printing, one triangle was no longer visible due to degradation and the other appeared to be moved by the force of a Schwann cell pseudopod. (d) After 310 minutes no printed objects were visible. Scale bar, 100 μm.

3.3.4 Compatibility with laminar flow device

To ensure that *in situ* μ-3D printing is compatible with the microfluidic laminar flow device, printing was tested after plating cells on polyimide film within the flow chamber of the device. This setup was identical to that used for cell dosing (Chapter 2), except that the cells were cultured within the device before printing instead of after printing. By heating the printing solution and flow chamber to 37 °C before injecting the printing solution into the chamber, it was possible to flow solutions containing low molecular weight gelatin at low pressure without disturbing Schwann cells cultured within the chamber. A solution containing of 58 mg/mL eosin-gelatin (Bloom number 60), 86 mg/mL gelatin (Bloom number 60), and 49 mg/mL BSA was used to achieve the lowest viscosity possible while retaining low cytotoxicity and effective photosensitizer concentration. To remove the printing solution after μ-3D printing, the flow chamber was placed in an environmental chamber heated to 37 °C and media warmed to 37 °C was slowly pipetted into the chamber. The cells were exposed to printing solution for no more than 20 minutes to reduce cytotoxicity, allowing for about 10 structures to be μ-3D printed. These method allowed the removal of printing solution with minimal harm to the Schwann cells cultured within the chamber.

Live/dead staining both before and after printing demonstrated that cell death was not dramatically increased by μ-3D printing (Figure 3.7). Although the increase in cell death from 0.7% to 3.5% was statically significant ($p < 0.003$), the vast majority of cells showed no apparent harm (Figure 3.8). Most cells appeared intact, as measured by enzymatic activation of Calcein AM, even after high intensity laser ablation of the polyimide substrate within microns of cells (Figure 3.7, b). Furthermore these cells did not allow the "dead" stain, ethidium homodimer-1, to enter the nucleus and bind to DNA. These results imply that μ-3D printing for purposes of cell dosing can be accomplished

on-the-fly within microns of cultured cells without significant harm to viability or morphology for 96.5% of cells.

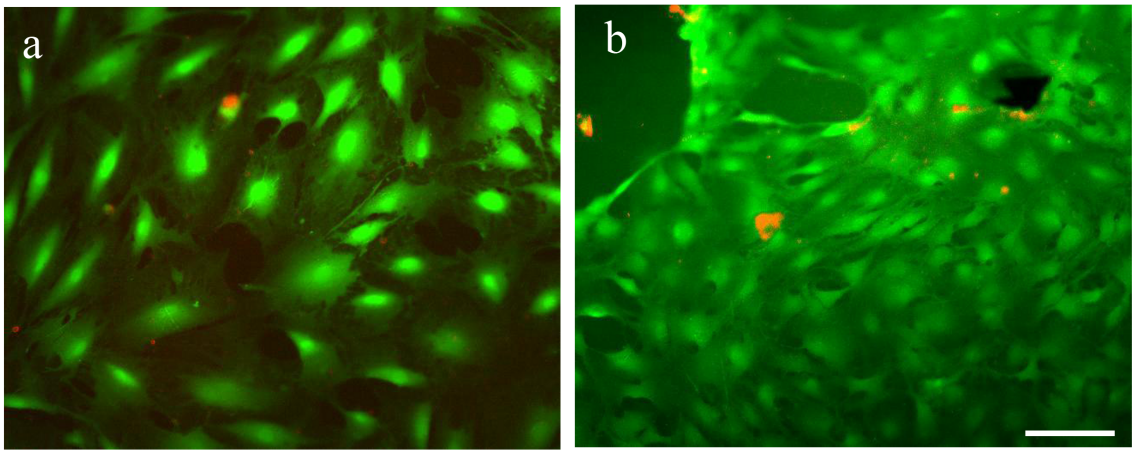

Figure 3.7: Cell viability after *in situ* μ-3D printing. (a) Live (green) and dead (red) stain before μ-3D printing on polyimide is shown for cultured Schwann cells. (b) Live/dead staining after μ-3D printing for a nearby region within the flow chamber. The black region in the shape of a triangle in the upper-right corner was the result of an ablation event during μ-3D printing. Triangles (20 μm in height) were μ-3D printed to the left of this ablation region. Scale bar, 100 μm.

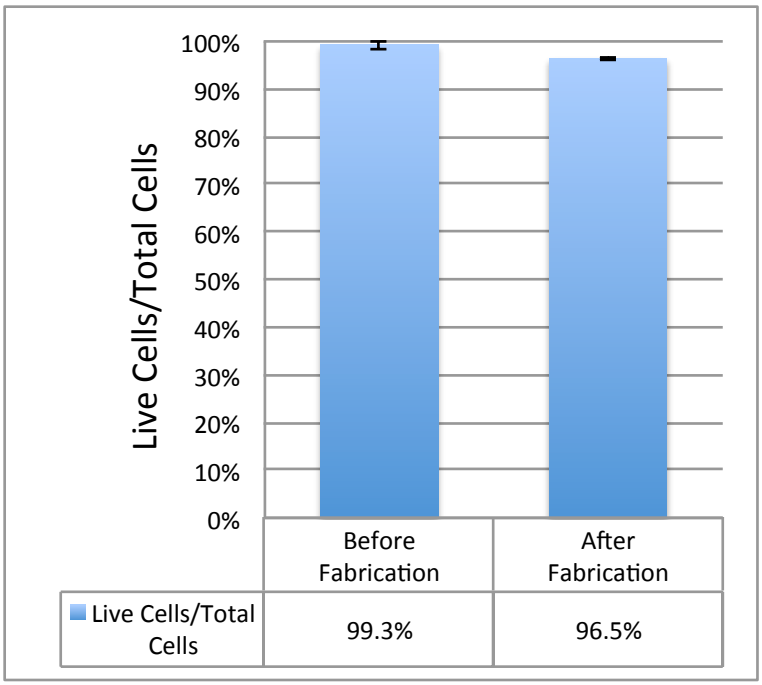

Figure 3.8: Cell viability analysis after *in situ* μ-3D printing. Live rat Schwann cells were counted before and after *in situ* μ-3D printing for three locations. The cells were exposed to printing solution for approximately 20 minutes. Error bars represent the standard deviation for cell counts between locations imaged.

3.4 Conclusion

This chapter presents a technique for *in situ* μ-3D printing of microstructures within microns of cultured cells for use with a microfluidic chamber. Adaptation of *in situ* μ-3D printing to microfluidics required further experimentation and the development of custom reagents with both low cytotoxicity and low viscosity. This advancement allows the μ-3D printing step to be completed *in situ* within microns of cultured cells without apparent effects on cell viability or morphology for over 96% of rat Schwann cells.

Although previous work implied that ascorbate may be useful in preventing oxidative damage of cultured cells during μ-3D printing, experimentation in this chapter revealed that antioxidants may not be necessary. Further experimentation demonstrated that free photosensitizer was cytotoxic, while photosensitizer-protein conjugates reduced cytotoxicity to negligible levels. This implies that the osmolality of printing solutions might be critical in reducing cell death during μ-3D printing. Additionally, the printing solution appears to acidify substantially when protein is added, and care should be taken to maintain neutral pH for *in situ* printing.

Following the protocol outlined in this chapter, *in situ* μ-3D printing can be applied to novel cell dosing experiments. A chimney could be printed within tens of microns of a cultured cell in order to dose the cell with 3D resolution. This technique could be further applied to trapping bacteria or somatic cells using μ-3D printed cages for the purpose of cell dosing. Cell dosing experiments with caged cells may, for example, provide new information about soluble factors necessary for bacterial quorum sensing or stem cell differentiation.

3.5 REFERENCES

1. Nielson, R., Kaehr, B. & Shear, J. B. Microreplication and Design of Biological Architectures Using Dynamic-Mask Multiphoton Lithography. *Small* **5**, 120–125 (2009).
2. Connell, J. L., Ritschdorff, E. T., Whiteley, M. & Shear, J. B. 3D printing of microscopic bacterial communities. *Proceedings of the National Academy of Sciences* (2013).
3. Hoppe, T. J. *Laser-Based Techniques for Manipulating the Single-Cell Environment*. Dissertation, University of Texas at Austin (2013).
4. Spikes, J. D., Shen, H.-R., Kopečková, P. & Kopeček, J. Photodynamic Crosslinking of Proteins. III. Kinetics of the FMN- and Rose Bengal-sensitized Photooxidation and Intermolecular Crosslinking of Model Tyrosine-containing N-

(2-Hydroxypropyl)methacrylamide Copolymers. *Journal of Photochemistry and Photobiology* **70**, 130–137 (1999).

5. Fairbanks, B. D., Schwartz, M. P., Bowman, C. N. & Anseth, K. S. Photoinitiated polymerization of PEG-diacrylate with lithium phenyl-2,4,6-trimethylbenzoylphosphinate: polymerization rate and cytocompatibility. *Biomaterials* **30**, 6702–6707 (2009).

6. Weishaupt, K. R., Gomer, C. J. & Dougherty, T. J. Identification of singlet oxygen as the cytotoxic agent in photo-inactivation of a murine tumor. *Cancer Research* **36**, 2326–2329 (1976).

7. Skovsen, E., Snyder, J. W., Lambert, J. D. C. & Ogilby, P. R. Lifetime and Diffusion of Singlet Oxygen in a Cell. *Journal of Physical Chemistry B* **109**, 8570–8573 (2005).

8. Horio, M. *et al*. Apoptosis induced by hypertonicity in Madin Darley canine kidney cells: protective effect of betaine. *Nephrology Dialysis Transplantation* **16**, 483–490 (2001).

9. Hermanson, G. T. *Bioconjugate Techniques*. (Academic Press, 2013).

10. Erlanger, B. F., Borek, F., Beiser, S. M. & Lieberman, S. Steroid-protein conjugates I. Preparation and characterization of conjugates of bovine serum albumin with testosterone and with cortisone. *Journal of Biological Chemistry*. **228**, 713–728 (1957).

11. Podczeck, F. & Jones, B. E. *Pharmaceutical Capsules*. (Pharmaceutical Press, 2004).

12. Huang, B. X., Kim, H.-Y. & Dass, C. Probing three-dimensional structure of bovine serum albumin by chemical cross-linking and mass spectrometry. *Journal of the American Society for Mass Spectrometry* **15**, 1237–1247 (2004).

13. Cherry, R. J., Cogoli, A., Oppliger, M., Schneider, G. & Semenza, G. A spectroscopic technique for measuring slow rotational diffusion of macromolecules. 1: Preparation and properties of a triplet probe. *Biochemistry (Moscow)* **15**, 3653–3656 (1976).

14. Youtsey, K. J. & Grossweiner, L. I. Optical Excitation of the Eosin-Human Serum Albumin Complex. *Journal of Photochemistry and Photobiology*. **6**, 721–731 (1967).

15. Gerlach, G. & Arndt, K.-F. *Hydrogel Sensors and Actuators: Engineering and Technology*. (Springer Science & Business Media, 2009).

16. Gao, D. *et al*. Investigation on the pH-dependent binding of Eosin Y and bovine serum albumin by spectral methods. *Journal of Luminescence*. **127**, 515–522 (2007).

17. Schrieber, R. & Gareis, H. *Gelatine Handbook: Theory and Industrial Practice*. (John Wiley & Sons, 2007).

18. Baron-Van Evercooren, A., Kleinman, H. K., Seppä, H. E., Rentier, B. & Dubois-Dalcq, M. Fibronectin promotes rat Schwann cell growth and motility. *Journal of Cell Biology* **93**, 211–216 (1982).

Chapter 4: Characterization of μ-3D Printed Stimuli-responsive Materials as Microactuators

4.1 Introduction

Stimuli-responsive materials, often known as "smart materials", have been widely studied for their unique ability to swell or change shape due to changes in environmental pH, temperature, ion concentration, or photo-irradiation [1][2]. These materials have been used to create micron-scale mechanical actuators. Microactuators made of stimuli-responsive hydrogels are advantageous because of a short chemical diffusion time, providing fast response to changes in the environmental pH or ion concentration. In contrast to electronic microactuators, hydrogels can rapidly change size or shape without external power sources or wiring. Specifically, applications to microfluidics include pH-responsive hydrogels [3], temperature-responsive hydrogels [4], and light-responsive hydrogels [5] placed within channels to manipulate flow paths or serve as valves.

The pH response of μ-3D printed BSA, avidin, and lysozyme hydrogels was demonstrated by former Shear group member Bryan Kaehr [6]. Kaehr demonstrated that BSA hydrogels swell up to 1.5 times their initial area in solutions of pH 12, compared to solutions of pH 7. Furthermore, Kaehr demonstrated that μ-3D printed BSA hydrogels could be used as microactuators and trap bacteria using the pH responsiveness and micron-scale resolution of μ-3D printed cell enclosures [7]. Jodi Connell further demonstrated that μ-3D printed BSA hydrogels swell when exposed to increased temperature or focused light. However, the temperature and light responsiveness of μ-3D printed BSA hydrogels was either irreversible or non-cyclic.

When thermoresponsive or photo-thermoresponsive materials are desired, N-isopropylacrylamide (NIPAAm) is commonly polymerized with other materials to make a hydrogel capable of cyclic swelling at physiological temperatures. Polymerized

NIPAAm exhibits a transition from a hydrophilic state to a hydrophobic state at a lower critical solution temperature (LCST) of 32 °C. This transition temperature can be increased with co-polymerization of hydrophilic monomers such as *n*-butyl methacrylate [8], and decreased with hydrophobic monomers including N-tert-butyl acrylamide [9]. When incorporated into a hydrogel in aqueous solution, NIPPAm can illicit a 50 fold shift in swelling ratio as measured by mass at the LCST [10]. For applications as diverse as microlenses [11] to drug delivery nanoparticles [1], NIPPAm has been incorporated into materials for its dramatic shift in swelling behavior at a temperature close to that of the human body.

Due to the fact that the stretching and bending vibrational frequencies of water can be accessed by infrared light, a hydrogel valve consisting of NIPPAm can be actuated remotely with an infrared laser (1480 nm). The molecular vibrations of water within the NIPPAm hydrogel raise the hydrogel temperature above 32° C. This system was effective at producing hydrogel response times as short as 3 ms and microfluidic switching times of 120 ms [8]. However, this system is not ideal for use in close proximity of cells due the cytotoxicity of heating the cytoplasm of cultured cells by high intensity infrared laser light.

In order to modulate a NIPPAm valve with light in the visible spectrum (390-700 nm), a chromophore must be integrated into the hydrogel structure to convert irradiated light into heat. Researchers have combined thermoresponsive materials with chromophores as exotic as spirobenzopyran, and as common as carbon black [4]. While carbon black is low cost, it requires high light intensity (1600–2700 mW/cm^2) to generate heat, which may damage cells and proteins in the vicinity of the hydrogel. The more expensive custom spirobenzopyran chromophore conjugated to a NIPAAm polymer requires only 30 mW/cm^2 of light intensity to generate enough heat to deswell the

hydrogel and open a microfluidic valve [5]. Alternatively, Suzuki and Tanaka used trisodium salt of chlorophyllin as a chromophore to heat NIPPAm hydrogel with a 488 nm argon laser, resulting in swelling response times as low as 5 ms [12]. NIPPAm has also been combined with the UV sensitive chromophore bis(4-(dimethylamino)phenyl)(4-vinylphenyl)methyl leucocyanide in order to swell hydrogels using a mercury lamp [13].

Although NIPPAm is a very popular hydrogel material, there appears to be only a single published account of creating NIPPAm hydrogels with 3D features and micron scale resolution [14]. Jhaveri and colleagues applied multiphoton lithography (μ-3D printing) to create square-shaped pads consisting of NIPPAm and PEG. Although the pads demonstrated no unique 3D properties or features, the placement of each pad was varied within three dimensions. However, the authors did not demonstrate any applications for these pads to microfluidics or cell culture. This chapter explores the application of μ-3D printed, temperature-responsive NIPPAm structures with 3D shapes and micron scale features to a microfluidic cell culture platform.

4.2 Experimental Methods

4.2.1 Chemicals and Reagents

N-isoproplyacrylamide (NIPPAm; I0401) was purchased from Tokyo Chemical Industry Company (Tokyo, Japan). Bovine serum albumin (BSA; BAH64) was purchased from Equitech-Bio (Kerrville, TX). Tris(hydroxymethyl)aminomethane (Tris; 252859) and 700 Da polyethylene glycol diacrylate (PEGDA; 455008) were purchased from Sigma-Aldrich (St. Louis, MO). Fluorescein (119241000) was purchased from Acros Organics (Geel, Belgium).

4.2.2 μ-3D Printing

Micro-three-dimensional printing (μ-3D printing) was performed using a mode-locked Ti:sapphire laser tuned to 740 nm with a pulse duration < 130 fs and repetition rate of 76 MHz (Coherent, Mira 900F). Photomasks were displayed using the SVGA graphics output of a desktop computer displayed on an 800 x 600 pixel digital micromirror device (DMD) (BenQ, MP510) capable of modulating each mirror ~20° when switched from a white to black graphical input. Dual-axis galvanometer scan mirrors (Thor Labs) were used to raster the beam at 50 mHz and 100 Hz across the x- and y-axis, respectively. A series of relay lenses were used to focus the beam onto the DMD and collimate the beam into the back aperture of a 60x, 1.4 NA objective within a Nikon inverted microscope. The z-axis position was dictated by a digital piezo controller and multi-axis nanopositioning system with capacitive sensors (Physik Instrumente, E-710). Control of the stage, scan mirrors, and DMD was synchronized using custom routines created in LabView™ (National Instruments). Photomasks were displayed at each z-axis position and updated during z-axis steps while the raster scan was at a terminal position. The DMD photomask system was placed conjugated to the plane of printing, so that each mask corresponded to a single layer of printing. Laser power at the objective back aperture was attenuated to 22-30 mW with a beam splitting cube and half-wave plate.

Structures were printed from a solution of 13% wt PEGDA, 40% wt NIPAAm, and 12.5 mM Rose Bengal in a solvent of 15% (v/v) PEGDA, 25% (v/v) H_2O, and 60% (v/v) DMSO, unless otherwise noted. The microfluidic device was partially assembled and the upper flow chamber was filled with printing solution before mounting on a #1 glass coverslip for μ-3D printing. Excess printing solution was washed out of flow chambers using 50% (v/v) DMSO/H_2O followed by several rinses with 100% deionized H_2O.

4.2.3 Imaging Swelling Characteristics

Fluorescein dye (10-20 μM) was used to image streams emitted from the pores to determine the effects that microstructures had on laminar flow streams originating at each pore. Fluorescein solutions contained 20 mM acetate (pH 4) to minimize fluorescence signal in optical axis originating from the dye solution in the reservoir flow chamber while a chamber flowing 200 mM Tris (pH 9) generated higher fluorescence signal where the dye was received. The increase in fluorescence signal was achieved due to the greater fluorescence of the conjugate base form of fluorescein dye that is dominant in basic solutions. Wide-field fluorescence images of this process were acquired using a Zeiss Axiovert 135 inverted microscope, Zeiss HBO 100 mercury arc lamp, FITC filter set, and Hamamatsu Orca II charge-coupled device (CCD) camera (C4742-98) controlled by MetaMorph imaging software (Molecular Devices) using a Zeiss 20x, 0.5 NA objective.

To control temperature within the microfluidic device an environmental chamber was placed around the flow chambers and positioned on the microscope stage. The environmental chamber was constructed from 6.3-mm plexiglass for the walls and lid, with a 1.6-mm-thick aluminum base fit to a Prior stage insert. Beneath the chamber a conductive heating element (Brook Industries) was used to maintain the stage temperature. Additionally, air was heated and forced into the environmental chamber with a heat gun (Westward, 4HWK1), 3.8-cm-diameter polyethylene tubing, and a fan. The heat gun was cycled on and off to maintain a set temperature with a thermocouple and PID controller (Red Lion, T1620000). The relative humidity was increased to prevent evaporation of small volumes of reagent by placing a dish of distilled water within the chamber.

A confocal fluorescence laser scanning microscopy (LSM; Zeiss, LSM 710) was used to image microstructures. Components of the LSM system were controlled by Zen

software (Zeiss; Jena, Germany) including objective lenses, stage position, pinhole size, PMT gain, and excitation lasers. Detection wavelengths were selected based on dye emission spectra using the 34-channel Zeiss QUASAR detector, also controlled by the Zen software. The QUASAR detector uses a diffraction grating to disperse the emitted fluorescence light across a detector array. Fluorescence signal from microstructures (containing residual Rose Bengal) was excited with a DPSS laser (561 nm) and detected at 566-711 nm. Confocal imaging on glass substrates was completed with a Zeiss plan-apochromatic 63x, 1.4 NA oil immersion objective (190 μm working distance).

4.3 Results and Discussion

4.3.1 Temperature Response of μ-3D Printed NIPPAm

In order to develop microstructures capable of reversibly swelling and modulating the flow of reagent in real time during cell culture, μ-3D printing was attempted with thermoresponsive NIPPAm. Although the photo-crosslinking of 700 Da PEGDA in the presence of Rose Bengal using the Ti:Sapphire laser (740 nm) resulted in hydrogel microstructures, solutions of NIPPAm and bis-acrylamide did not demonstrate this behavior under similar irradiation and Rose Bengal concentrations. Although NIPPAm and bis-acrylamide are commonly used to create hydrogels, the low molecular weight of each monomer requires photo-irradiation of 30 minutes or more to create polymers of high enough molecular weight to form a hydrogel.

In order to create hydrogels with the μ-3D printing system, 700 Da PEDGA was used as a cross-linking reagent in place of bis-acrylamide. This PEDGA stock contained on average 13.6 ethylene glycol monomers per polymer chain before cross-linking. When NIPPAm was combined with PEGDA and Rose Bengal in solution the resulting structures demonstrated thermoresponsive swelling behavior. Data in Figure 4.1 confirm

that when square-shaped NIPPAm/PEGDA pads were heated from 18 to 38° C up to 30% reduction in area was observed, as measured by bright field images. The ability of this solution to create thermo-responsive hydrogels may be due the crosslinking of PEGDA and NIPPAm monomers into a network that allows polar and nonpolar side chains of NIPPAm to rotate within the network (Figure 4.2). Furthermore, it has been reported that the addition of PEGDA to a solution containing NIPPAm created hydrogels with faster swelling kinetics due to increased porosity [10].

In order to evaluate the effect of porosity on μ-3D printed NIPPAm/PEGDA structures, the step size between fabrication planes was varied from 0.5 to 1.5 μm/step (Figure 4.1). The increased space between fabrication planes may result in greater porosity or areas of lower cross-linking. In fact, the larger step sizes resulted in greater swelling than the 0.5 μm/step, although this effect was not seen between 1.0 and 1.5 μm/step.

Zhuo and Li demonstrated that increased porosity of NIPPAm/PEGDA hydrogels corresponds to a four-fold increase in swelling ratio. Their work was performed with one-photon promoted photopolymerization crosslinked hydrogels, but appears to correlate well with the multiphoton μ-3D printed hydrogels presented here. Furthermore, work by previous Shear group members has demonstrated that increasing μ-3D printing step size resulted in larger pH and temperature swelling effects for BSA/gelatin structures [7].

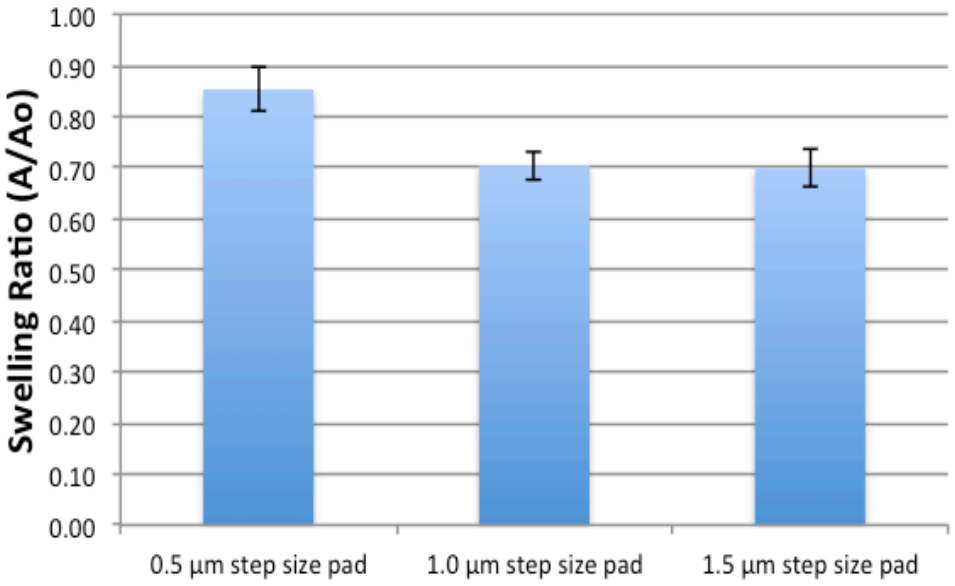

Figure 4.1 Data obtained from the change in observable area in bright field images when μ-3D printed structures were heated from 18 to 38° C. Error bars represent the standard deviation of area measurements taken from 8 samples per condition. The square-shaped structures were fabricated from a solution of 13% wt PEGDA, 40% wt NIPAAm, and 12.5 mM Rose Bengal in a solvent of 15% (v/v) PEGDA, 25% H_2O, and 60% DMSO. The step size between fabrication scans was varied while all other parameters were unchanged including a 6.25 s scan per plane and 20 μm nominal height above untreated #1 cover glass. Printing was completed on an inverted Nikon microscope with 30 mW delivered to the back aperture of a 60x 1.4 NA objective from a Ti:Sapphire laser (740 nm).

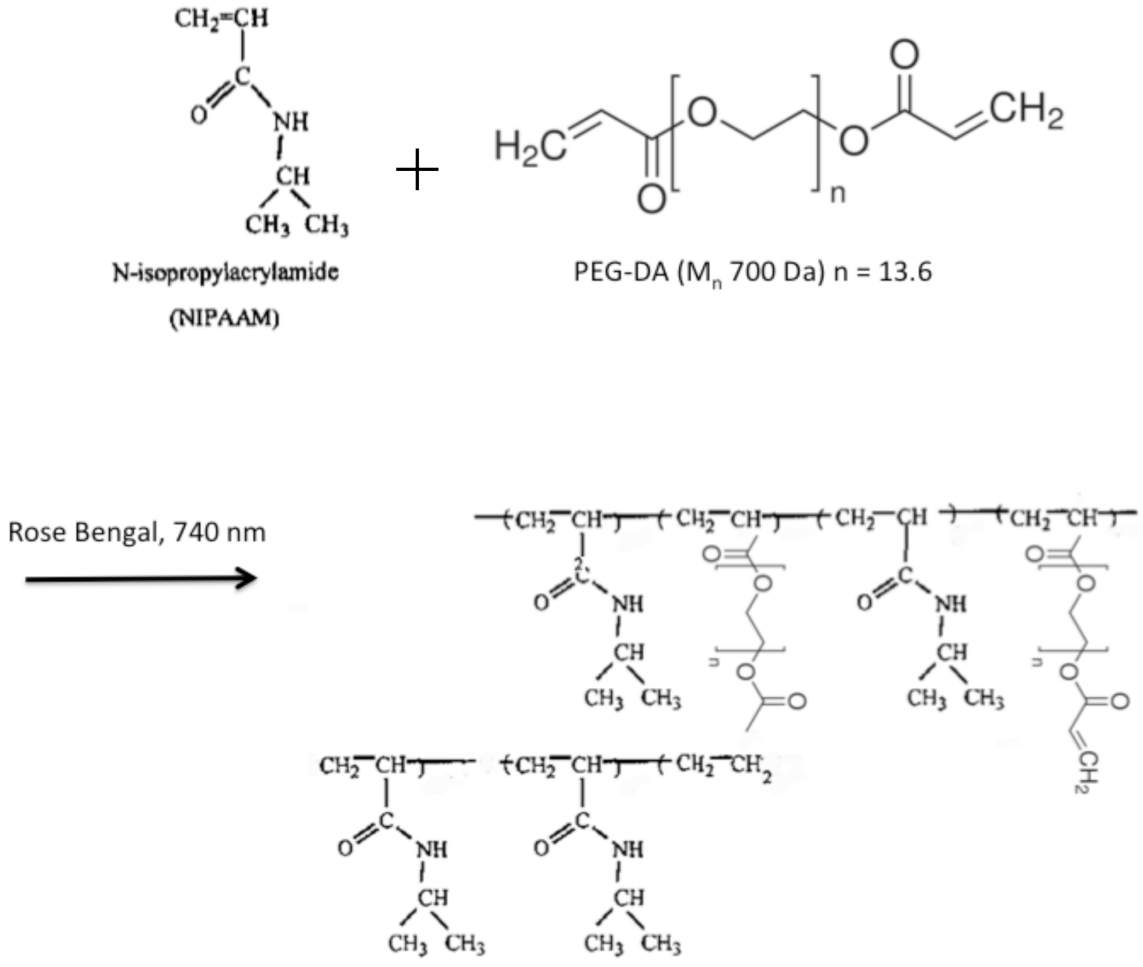

Figure 4.2: Diagram of possible crosslinking sites for a hydrogel composed of NIPPAm and PEGDA (700 Da) when polymerized and crosslinked in the presence of Rose Bengal and tightly focused Ti:Sapphire laser light (740 nm). The longer chains of PEGDA may provide spatial hindrance between NIPPAm monomers, allowing faster swelling kinetics.

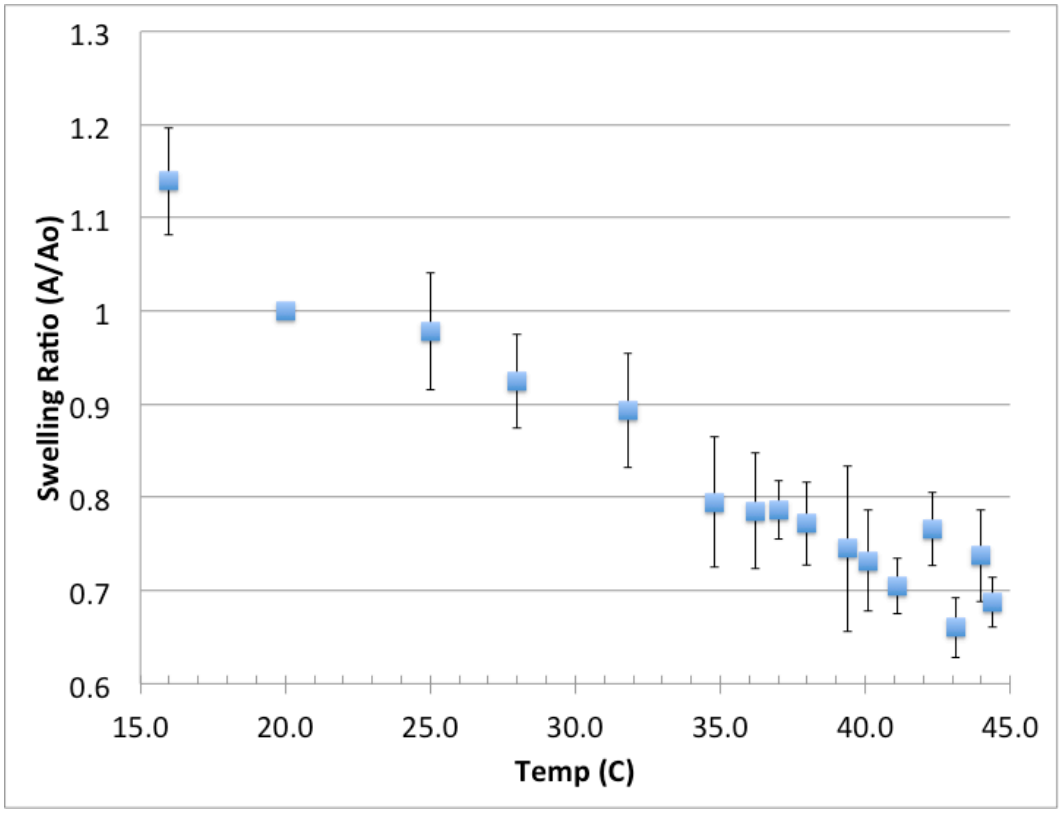

Figure 4.3 Temperature response of NIPPAm/PEG. The swelling response was measured for four square-shaped structures while increasing the ambient temperature in an environmental chamber. Error bars represent the standard deviation of four samples. Each temperature point was maintained for 10 minutes while monitoring ambient water temperature within the Petri dish containing the structures with a thermocouple. Each temperature and swelling point was taken after the temperature was stable and no change in area was apparent. Swelling ratios were determined from bright field images captured with a 40x, 0.75 NA objective. Structures were μ-3D printed from a solution of 62% wt NIPAAm and 23 mM Rose Bengal in a solvent of 6% (v/v) PEGDA, 24% H_2O (v/v), and 70% (v/v) DMSO. The structures were printed with 29 mW of laser power at the back aperture of a 60x, 1.4 NA Nikon objectives. The structures were printed to a nominal height of 20 μm using 0.5 μm/step between planes.

The temperature response of NIPPAm/PEGDA structures was further explored across a range of temperatures from 16 to 45 °C (Figure 4.3). In addition to a general trend of deswelling at increased temperature, there is a 10% loss in area between 31 and 35 °C. This corresponds with a reported NIPPAm LCST of 32 °C. The general trend of linear deswelling across a range of temperatures comports with published swelling data for single-photon crosslinked NIPPAm/PEGDA hydrogels. For example, Zhuo and Li reported that higher ratios of PEGDA:NIPPAm result in a more porous structures with an increased and more linear swelling response over a temperature range of 25 to 35 °C [10].

4.3.2 Confocal Imaging of NIPPAm Structures

In order to ensure the fidelity of the NIPPAm/PEGDA in reproducing μ-3D printed shapes, confocal images were obtained of printed structures. The x-axis and z-axis signal from residual Rose Bengal within the structures was used to determine the fidelity of the structure relative to μ-3D printing parameters of 20 μm in height (z-axis) and 12.5 μm in width (x-axis) (Figure 4.4). All structures were imaged at room temperature (19 °C). Both the height and width of the structures appeared to swell to a size slightly larger than the photomask if the step size was less than 1.0 μm/step. It appeared that increased laser intensity per volume of the structure resulted in hydrogel formation beyond the edges of the laser focal volume. Conversely, step sizes 1.0 μm or greater resulted in measured heights less than the nominal height desired. Because 0.5 μm/step NIPPAm/PEGDA structures exhibited reduced swelling when heated and larger size than nominal size, it can be concluded that higher crosslinking of polymer chains occurred when a shorter step size was used. This higher crosslinking may have reduced the average pore size and reduced the capacity of water necessary for deswelling and swelling.

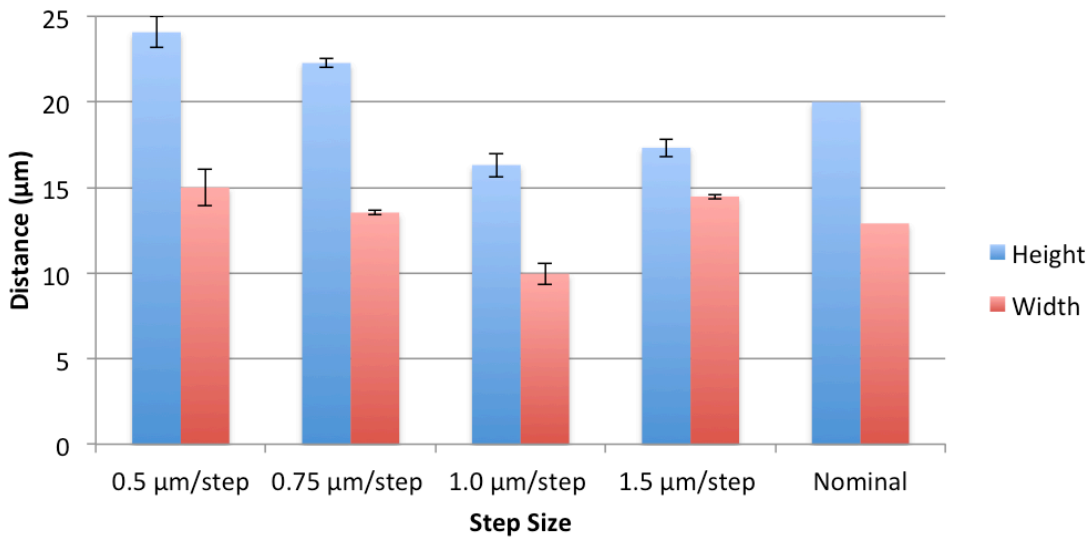

Figure 4.4: Confocal validation of NIPPAm/PEGDA structures. Square-shaped structures nominally 20 μm tall and 12.5 μm in width were μ-3D printed from a solution of 62% wt NIPAAm, 23 mM Rose Bengal in a solvent of 6% (v/v) PEGDA, 24% H_2O (v/v), and 70% (v/v) DMSO. The step size was varied from 0.5 to 1.5 μm/step and confocal measurements were used to determine height and width at room temperature (~19 °C). The structures were μ-3D printed and washed at ~19 °C. Error bars represent the standard deviation of four pads per condition.

4.3.3 Thermoresponsive Valve Design and Function

Using knowledge of the effect of μ-3D printing parameters and on structure thermoresponsiveness, it was possible to create structures with reproducible swelling behavior in order to examine the microfluidic functionality. A valve was chosen for its applications to cell dosing. Although the flow rate of the entire microfluidic system can be controlled, the flow through each pore cannot be individually varied. For cell dosing studies it may prove useful to provide a single cell with two streams of reagent consisting

of an equal concentration but unequal flow rate of reagent. To study control of flow through individual pores, a valve was μ-3D printed around an ablated pore from thermoresponsive NIPPAm/PEGDA.

A valve was designed and the valve geometry was improved in an attempt to not fully occlude flow at deswelled/open states (< 32 °C) and prevent leakage in the swelled/closed state (> 32 °C). A circular valve with a rectangular opening was μ-3D printed over pre-ablated pores (Figure 4.5, a). This design would have allowed chimney flow and valve control of the pore. However, it did not function in the open state, possibly due to clogging or high backpressure generated by the narrow opening.

A pair of right triangles with a 5 μm gap between the triangles at room temperature (~19 °C) was created to ensure flow in the open state (Figure 4.5, b). The triangle sized was varied in the z-axis with smaller triangles forming a base and larger triangles forming a bridge over the pore. As the temperature decreased, the NIPPAm/PEGDA triangles swelled closer together, enclosing the pore (Figure 4.5, d). However, no detectable reduction in flow was acquired by fluorescence imaging of the stream emitted by the valve. Using confocal microscopy it may be possible to determine if the flow of the pore is constrained by the swelling behavior of the valve.

To improve upon this swelling, laser light was applied to heat the structure. However, no infrared laser was available for this study and the high intensity pulses of the Nd:YAG (532 nm) laser resulted in destruction of the NIPPAm/PEGDA hydrogel. However, images acquired of μ-3D printed NIPPAm/PEDGDA square-shaped pads reveals a reproducible swelling ratio of 0.55 (area/initial area) (Figure 4.6). The cyclic behavior of this material when μ-3D printed would be useful in a creating a functioning valve.

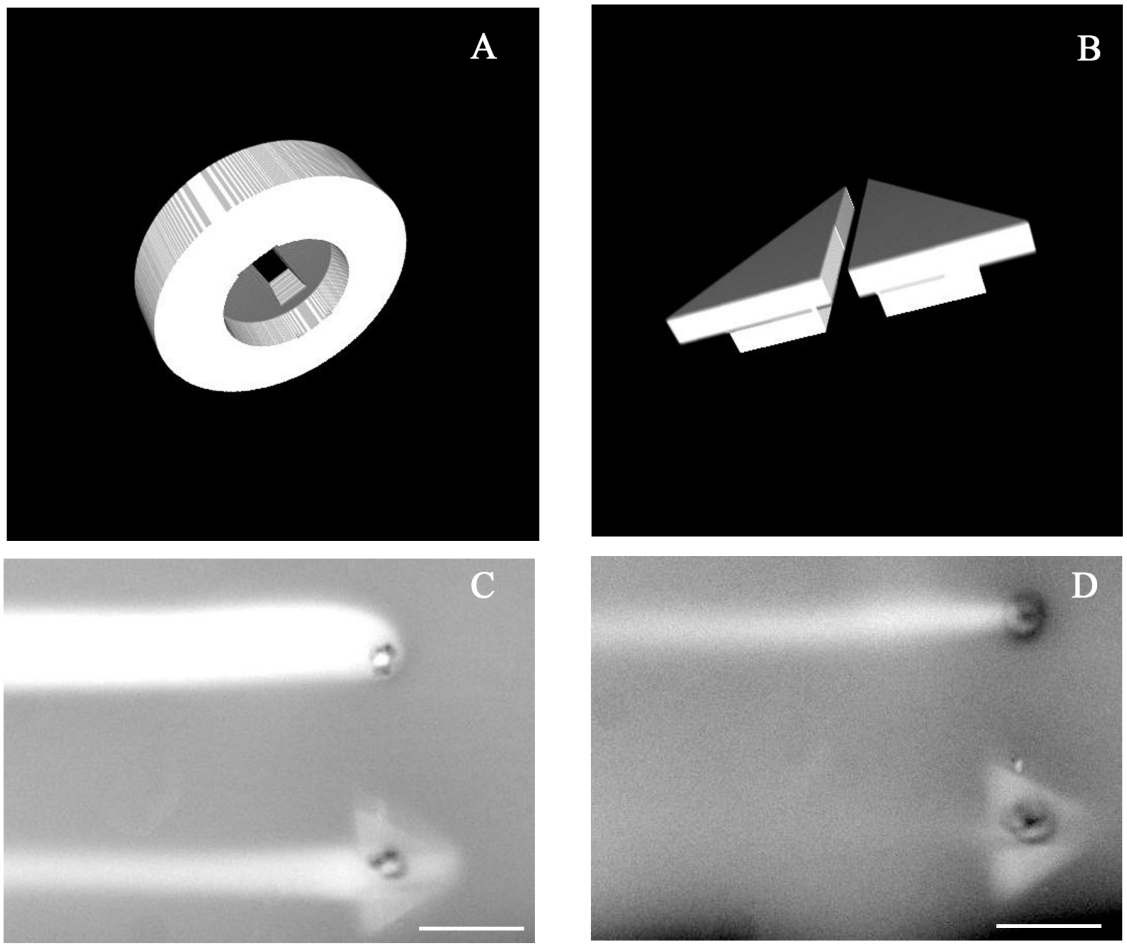

Figure 4.5: Thermoresponsive valve testing. (a) A circular valve design was created with a rectangular slit to encolose an ablated pore but failed to deliver flow in the open state. (b) A pair of larger triangles with smaller triangles beneath allowed flow in both open and closed state. (c) A pore with no obstruction (top) and a pore with a μ-3D printed NIPPAm/PEGDA valve (bottom, geometry shown in panel b) were tested in parallel. The triangle-shaped valve was μ-3D printed to a nominal hieght of 20 μm using 0.5 μm/step. At 40 °C the hydrogel allowed a stream of 10 μM fluorescein to emerge from the pore. (d) At room temperature (19 °C) the valve contiued to flow. Scale bar of 50 μm applies to images (c) and (d).

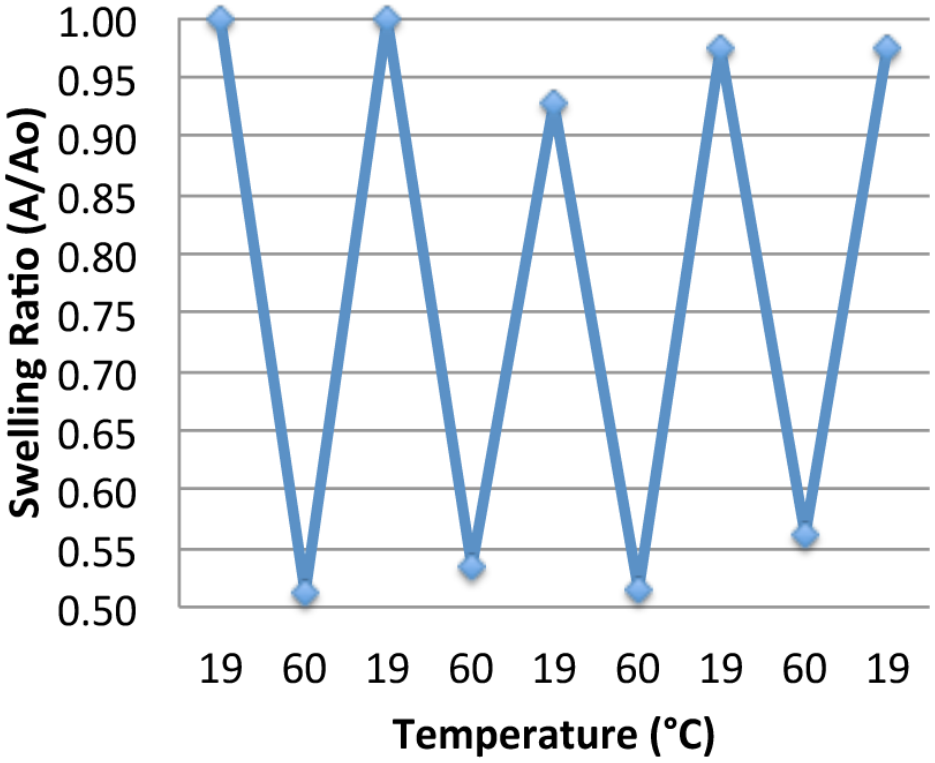

Figure 4.6: NIPPAm swelling cycle testing. A square-shaped pad μ-3D printed from a solution 62% wt NIPAAm, 23 mM Rose Bengal in a solvent of 6% (v/v) PEGDA, 24% H_2O (v/v), and 70% (v/v) DMSO was heated to 60 °C and cooled to 19 °C repeatedly to evaluate the thermal cycling properties of the material. Swelling ratios were determined from the area observed in bright field images.

4.3.4 Temperature Response of BSA/Gelatin

In order to apply the benefit of *in situ* μ-3D printing described in Chapter 3, the temperature responsiveness of gelatin/BSA structures was tested. As demonstrated in Chapter 3, these materials does not display detectable cytotoxicity as measured by live/dead staining and can be μ-3D printed around living cells without detectable harm. Although NIPPAm structures do not prevent cell adhesion and growth [15], the precursor solution must contain organic solvents such as DMSO at concentrations toxic to cells.

Gelatin/BSA structures were μ-3D printed from a solution similar to that used in Chapter 3, but without covalent conjugation of the photosensitizer to the protein due to reagent cost. The printing solution consisted of 301.5 mg/mL gelatin (Type A), 25 mg/mL BSA, and 10 mM Rose Bengal. The first heat cycle of these structures resulted in a swelling ratio (area/initial area) of 1.33. However, subsequent heating cycles failed to reproduce this effect (Figure 4.7). The non-cyclic temperature swelling of BSA structures has been described by former Shear group member Jodi Connell [7]. The reason for this effect is not clear, but may involve thermal deformation of the hydrogel so that it does not maintain its elastic properties. This may be due to physical crosslinking or protein denaturation. Regardless of the cause, the non-cyclic properties exclude BSA/gelatin as a useful material for thermal-responsive applications such as valves. However, Connell was able to apply the non-cyclic thermal swelling of BSA/gelatin to trap bacteria for quorum sensing experiments [16]. After loading each μ-3D printed structure she was able to seal the exit by heating to 37 °C. With advancements in *in situ* μ-3D printing described in this dissertation (Chapter 3), thermoresponsive BSA/gelatin could be applied to experiments with mammalian cells.

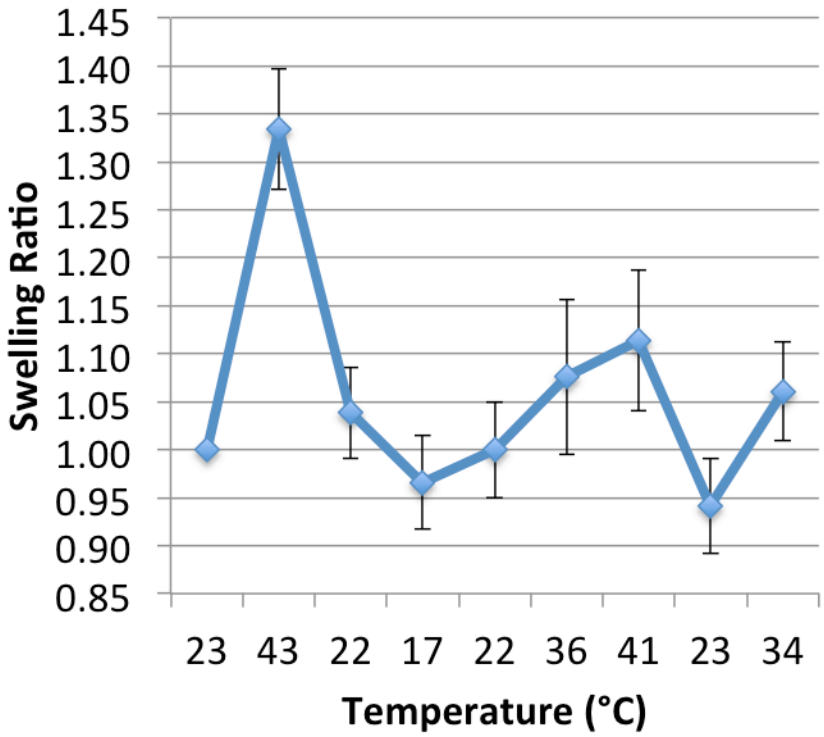

Figure 4.7: The temperature responsiveness of μ-3D printed gelatin/BSA. The swelling ratio is displayed for four structures heated sequentially from left to right on the x-axis of the plot. The structures were printed from a solution of 301.5 mg/mL gelatin (Type A), 25 mg/mL BSA, 10 mM Rose Bengal. The printing step size was 1.0 μm/step. Error bars represent standard deviation.

4.3.5 pH Response of μ-3D Printed Hydrogels

The response of μ-3D printed hydrogels to solutions of differing pH was explored to better understand if these materials could function as microactuators. As demonstrated in Chapter 3 of this dissertation, solutions of BSA and gelatin can be μ-3D printed in the presence of mammalian cells with minimal cytotoxic effects. In comparison to BSA alone, BSA-gelatin mixtures exhibit less pH response at a range of pH values as determined by changes in observable area under bright field illumination (Figure 3.8).

Furthermore, mixtures of BSA and PEGDA resulted in less observed swelling at equivalent pH values than BSA alone. Reduced BSA content in the hydrogel network may reduce the pH response due the reduction in ionizable groups. Bryan Kaehr demonstrated that μ-3D printed protein hydrogels reach a minimum swelling area when exposed to a solution of equal pH to the known isoelectric point of the protein [17]. The isoelectric point of BSA is ~4.7 [18], the isoelectric point of gelatin Type A is 7-9 [19], and PEGDA does not ionize in aqueous solutions. Mixtures of proteins with different isoelectric points may mitigate the swelling effect across a range of pH values.

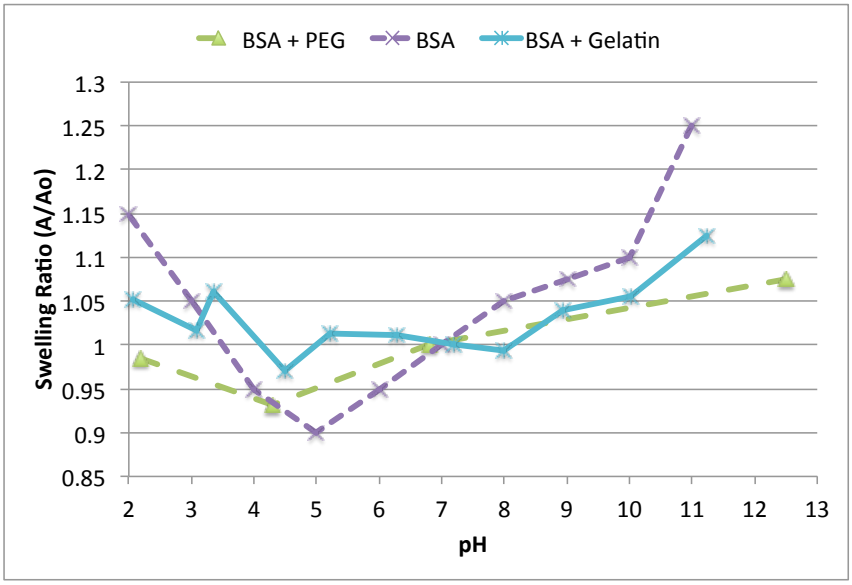

Figure 4.8: The swelling ratio of μ-3D printed structures was explored for a range of pH values. "BSA + PEG" structures were μ-3D printed from a solution of 275 mg/mL BSA, 15% (v/v) PEDGA, and 7.5 mM Rose Bengal. "BSA" structures were μ-3D printed from a solution of 400 mg/mL BSA and 10 mM Rose Bengal. "BSA + Gelatin" structures were μ-3D printed from a solution of 55 mg/mL BSA, 171 mg/mL Gelatin Type A, and 10 mM Rose Bengal.

BSA structures were μ-3D printed within a flow chamber on a polyimide film and a second flow chamber was attached as described in Chapter 2. This configuration allowed the structures to be selectively exposed to solutions of different pH using an ablated pore between the two flow chambers (Figure 4.9). When BSA pads were μ-3D printed from a solution of 400 mg/mL BSA and 10 mM Rose Bengal, a 40% reduction in observed area was achieved by dosing with 0.1 M citrate (pH 5). Furthermore, this de-swelling effect appeared rapidly after the solution was applied and was maintained for as long as the acidic stream was flowing across the structures (Figure 4.10).

The flow chamber in which the BSA pads were printed was flowing deionized water titrated to pH 9 with sodium hydroxide. This larger source of basic solution provided a bulk flow against which the smaller, acidic stream emitted from the pore was able to neutralize within the diffusion zone. The response of the μ-3D printed hydrogel was related to the strength of each buffer and appeared to decrease in size and strength when the buffer strength of the bulk flow was increased (Figure 4.11). That is, the amount of de-swelling observed by the BSA pads was decreased when the bulk flow of deionized water was replaced with 0.1 M Tris (pH 9). Furthermore, when the bulk solution was replaced with 1.8 mM L-15 (pH 7.2) the smallest change in swelling ratio was observed. This effect appeared to be due to increased initial swelling by the neutral solution before a stream of 0.1 M citrate (pH 5) was applied.

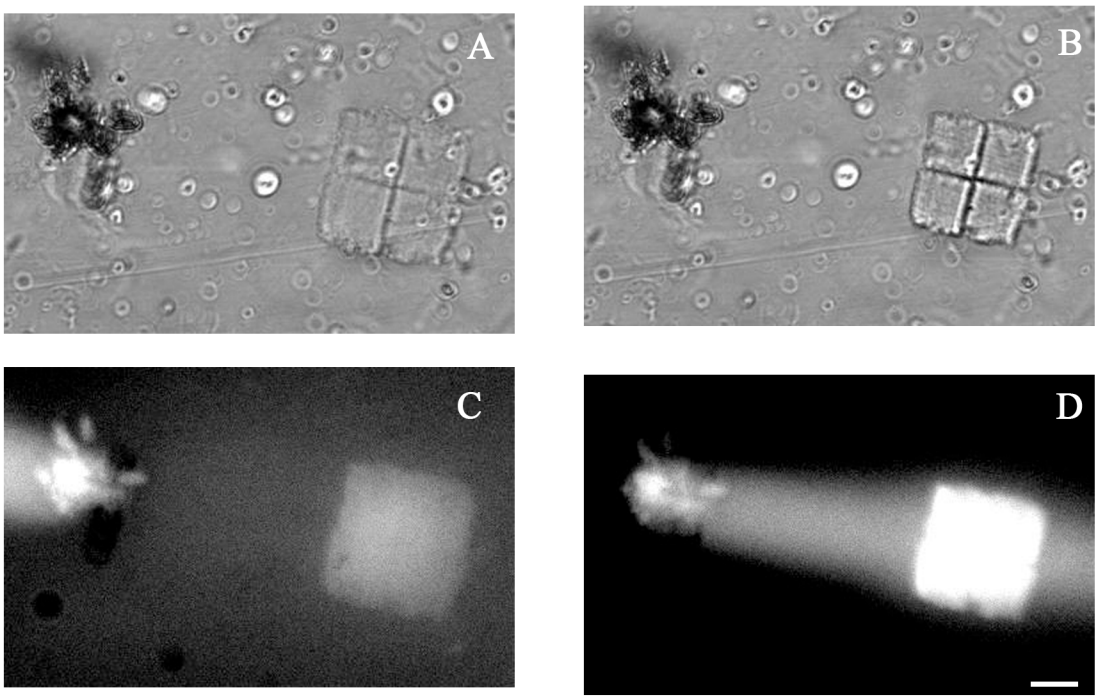

Figure 4.9: BSA structure pH response. The swelling response of pads μ-3D printed from a solution of 400 mg/mL BSA and 10 mM Rose Bengal was tested within a flow chamber. A solution of 10 μM fluorescein and 100 mM citrate (pH 5) was emitted from a pore into a chamber flowing a deionized water titrated with NaOH (pH 9). (a) A bright field image was acquired before the BSA pad was exposed to an acidic stream. (b) A bright field image was acquired during flow of citrate buffer (pH 5) over the pad. (c) A fluorescence image was acquired before the BSA pad was exposed to acidic buffer. (d) A fluorescence image was acquired during exposure to acidic buffer. Scale bar, 10 μm.

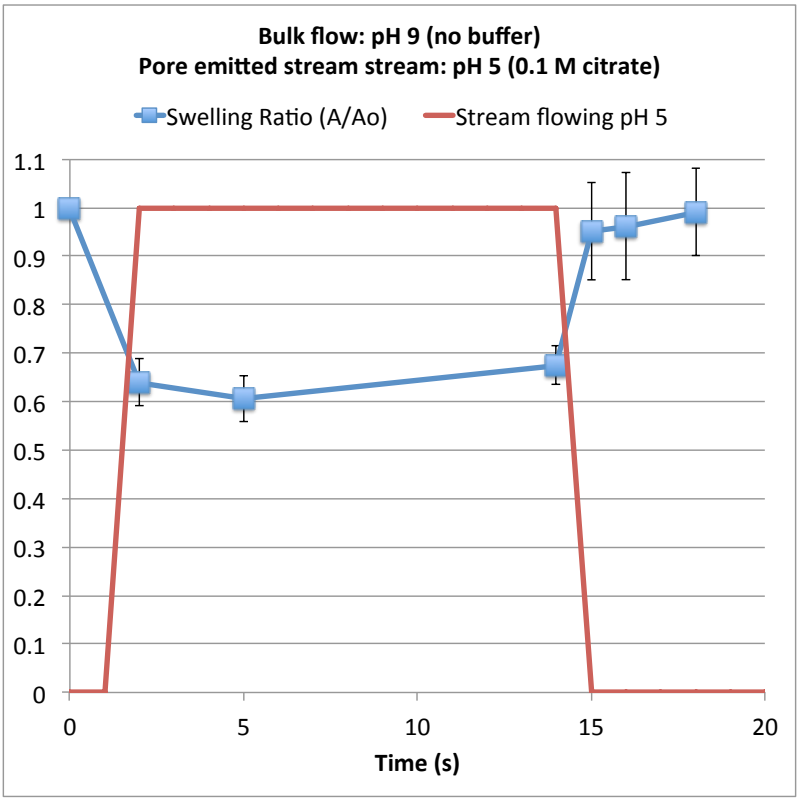

Figure 4.10: Kinetics of BSA structure swelling in a flow chamber. Pads were μ-3D printed from a solution of 400 mg/mL BSA and 10 mM Rose Bengal. The swelling ratio (area/initial area) is plotted during the time course in which a stream of 0.1 M citrate buffer (pH 5) was emitted from a pore. At the initial time no citrate buffer was flowing, as represented by a value of "0" on the y-axis. During times that citrate buffer appeared to flow out of the pore, the stream flowing value is displayed as "1". Error bars represent standard deviation for the four pads exposed to the acidic stream.

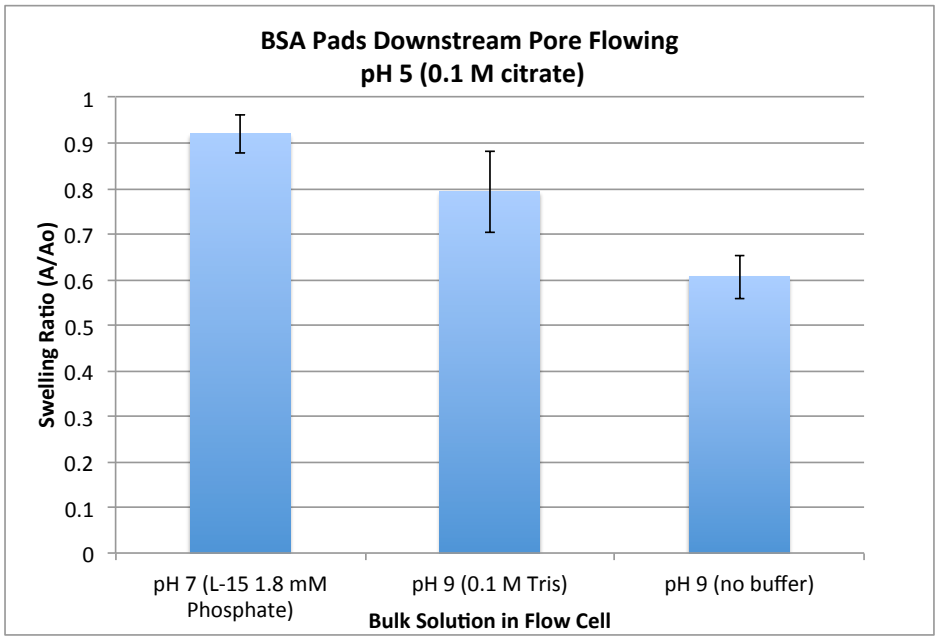

Figure 4.11: Effect of flow chamber pH on BSA swelling. The swelling ratio (area/initial area) was determined for BSA pads μ-3D printed from a solution of 400 mg/mL BSA and 10 mM Rose Bengal. A stream of 0.1 M citrate (pH 5) was emitted from a pore into a chamber containing one of three solutions: L-15 (pH 7), 0.1 M Tris (pH 9), or deionized water (pH 9). Error bars represent the standard deviation for four pads.

In order to determine if pH-responsive BSA structures could be used for on-the-fly control of chimney size and height, confocal microscopy was used to analyze structure height. BSA funnels were μ-3D printed to be 20 μm in height with the same geometry exhibited in Chapter 2, section 2.3.4. In comparison to pH 7.2, a solution of 0.1M Tris, 0.1 M citrate (pH 5) resulted in a 13 ± 8% reduction in height (Figure 4.12). A solution of 0.1 M Tris, 0.1 M citrate (pH 9) resulted in a 37 ± 22% increase in height for the three μ-3D printed chimneys analyzed. This demonstrates that μ-3D printed BSA chimneys could be used to modulate the dosing height or serves as valves in a microfluidic chamber.

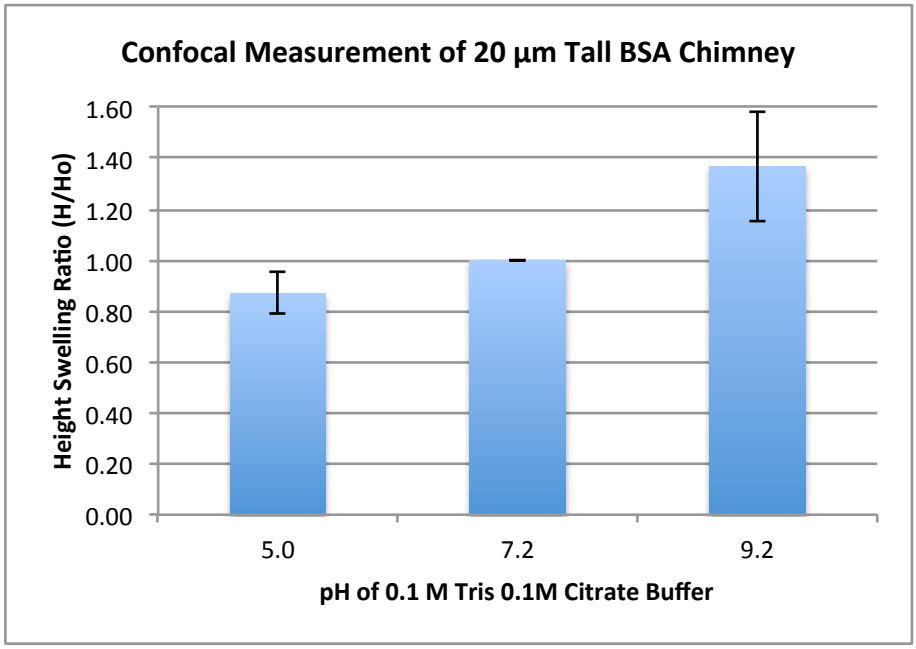

Figure 4.12: Vertical swelling ratio for chimneys. Confocal fluorescence microscopy was used to determine the swelling ratio for the vertical axis (height/initial height). The height at pH 7.2 was used to normalize the values. A buffer solution was titrated to each pH value (0.1 M Tris, 0.1 M citrate). Error bars represent the standard deviation for three chimneys at each pH value.

4.4 Conclusion

The ability of μ-3D printed NIPPAm/PEGDA hydrogel microstructures to swell in size due to temperature changes was studied. Cyclic, thermoresponsive swelling properties were apparent with a 45% reduction in area at 60 °C and 25% reduction at 37 °C, compared to initial area at 19 °C. In future studies, thermoresponsive materials could be combined with chromophores to create microstructures that respond to light with swelling/de-swelling behavior while delivering flow with 3D precision. This property could be exploited to drive microstructure valves with light produced from broad-spectrum sources or monochromatic lasers. Combined with the unique 3D capabilities of μ-3D printing, these thermoresponsive materials may be capable of

delivering reagent streams with 3D spatial resolution and on-the-fly valve control using laser light or ambient heat.

Structures μ-3D printed from proteins with low cytotoxicity displayed both temperature and pH-responsive properties. For applications including trapping bacteria or mammalians cells, swelling temperatures within physiological ranges (20 – 37 °C) allow these hydrogels to serve as micro-actuators. However this swelling appeared to be irreversible or non-cyclic. BSA and gelatin displayed cyclic swelling behavior only in response to changes in pH. These proteins were μ-3D printed and actuated within a microfluidic device. For applications that require cyclic swelling properties, pH-responsive BSA or gelatin may be useful for positioning dosing chimneys or controlling valves.

4.5 REFERENCES

1. Bajpai, A. K., Shukla, S. K., Bhanu, S. & Kankane, S. Responsive polymers in controlled drug delivery. *Progress in Polymer Science*. **33**, 1088–1118 (2008).
2. Beebe, D. J. *et al*. Functional hydrogel structures for autonomous flow control inside microfluidic channels. *Nature* **404**, 588–590 (2000).
3. Yu, Q., Bauer, J. M., Moore, J. S. & Beebe, D. J. Responsive biomimetic hydrogel valve for microfluidics. *Applied Physical Letters* **78**, 2589 –2591 (2001).
4. Jiang, L. & Erickson, D. Light-Governed Capillary Flow in Microfluidic Systems. *Small* **9**, 107–114 (2013).
5. Sugiura, S. *et al*. Photoresponsive polymer gel microvalves controlled by local light irradiation. *Sensors and Actuators Physics* **140**, 176–184 (2007).
6. Kaehr, B., Allen, R., Javier, D. J., Currie, J. & Shear, J. B. Guiding neuronal development with in situ microfabrication. *Proceedings of the National Academy of Sciences* **101**, 16104–16108 (2004).
7. Connell, J. L. *Characterization and microfabrication of environmentally sensitive materials for studying bacterial group behaviors*. Dissertation, University of Texas at Austin. (2012).

8. Shirasaki, Y. *et al*. On-Chip Cell Sorting System Using Laser-Induced Heating of a Thermoreversible Gelation Polymer to Control Flow. *Analytical Chemistry* **78**, 695–701 (2006).

9. Cunliffe, D. *et al*. Bacterial adsorption to thermoresponsive polymer surfaces. *Biotechnology Letters*. **22**, 141–145 (2000).

10. Zhuo, R.-X. & Li, W. Preparation and characterization of macroporous poly(N-isopropylacrylamide) hydrogels for the controlled release of proteins. *Journal Polymer Science Part A: Polymer Chemistry* **41**, 152–159 (2003).

11. Dong, L., Agarwal, A. K., Beebe, D. J. & Jiang, H. Adaptive liquid microlenses activated by stimuli-responsive hydrogels. *Nature* **442**, 551–554 (2006).

12. Suzuki, A. & Tanaka, T. Phase transition in polymer gels induced by visible light. *Nature* **346**, 345–347 (1990).

13. Mamada, A., Tanaka, T., Kungwatchakun, D. & Irie, M. Photoinduced phase transition of gels. *Macromolecules* **23**, 1517–1519 (1990).

14. Jhaveri, S. J. *et al*. Direct Three-Dimensional Microfabrication of Hydrogels via Two-Photon Lithography in Aqueous Solution. *Chemistry of Materials* **21**, 2003–2006 (2009).

15. Schmaljohann, D. *et al*. Thermo-Responsive PNiPAAm-g-PEG Films for Controlled Cell Detachment. *Biomacromolecules* **4**, 1733–1739 (2003).

16. Connell, J. L. *et al*. Probing prokaryotic social behaviors with bacterial 'lobster traps'. *MBio* **1**, e00202–10 (2010).

17. Kaehr, B. & Shear, J. B. Multiphoton fabrication of chemically responsive protein hydrogels for microactuation. *Proceedings of the National Academy of Sciences* **105**, 8850–8854 (2008).

18. Ge, S., Kojio, K., Takahara, A. & Kajiyama, T. Bovine serum albumin adsorption onto immobilized organotrichlorosilane surface: influence of the phase separation on protein adsorption patterns. *Journal of Biomaterial Science Polymer Edition* **9**, 131–150 (1998).

19. Digenis, G. A., Gold, T. B. & Shah, V. P. Cross-linking of gelatin capsules and its relevance to their in vitro-in vivo performance. *Journal of Pharmaceutical Science* **83**, 915–921 (1994).

Chapter 5: Cell Dosing with Rapid Reagent Exchanging

5.1 INTRODUCTION

Various cellular processes, including synaptic signaling, differentiation, and chemotaxis, are controlled to varying degrees by microscopic diffusible chemical gradients [1]. For neurons the time between a stimulus and an action potential, known as the latency, has been measured to be 5-10 ms [2]. However, in one study neutrophil polarization required over one minute after exposure to a chemoattractant gradient [3]. Because the temporal scale over which chemical gradients exist *in vivo* is believed to vary widely, elucidation of the mechanisms by which external chemical cues mediate polarized cellular behaviors requires tools that can not only recast chemical landscapes with subcellular resolution, but can also reposition gradients within milliseconds or sustain them for hours.

As summarized in Chapters 1 and 2, several microfluidic techniques exist for cell dosing. Techniques for reagent switching during cell dosing are also broad and varied. Neurobiologists studying action potentials have relied on capillary glass tubes for cell dosing and reagent switching. For example, one technique relies on the use of a motor controlled four-lumen capillary tube [4]. Although this technique allows fast exchanges between four different solutions, the diameter of the capillary glass limits the spatial resolution and number of dosing sites. Spitzer and Bridge created a technique for switching dosing solutions for cardiac cells in as little as 7 ms using double-barreled glass tubing and a solenoid [5]. However, neither system provides the sub-cellular spatial resolution and multiple dosing sites that are possible with the dosing platform described in this dissertation.

Using soft photolithography techniques, researchers have created air driven valves within a microfluidic device with reagent exchange times as low as 20 ms [6]. These valves are actuated by commercially available high speed solenoid valves controlling the supply of pressurized air to the device. Another technique relied on a stepper motor to change the relative flow rates of two reagents within a microfluidic dosing chamber, achieving response times as low as 189 ms [7]. However, neither of these techniques allow for a small diameter dosing stream, they only create a boundary between two reagents that can be moved rapidly.

Former Shear group member Todd Hoppe developed a reagent switching system for the microfluidic dosing platform that relied on changes to the syringe pump flow rates, resulting in reagent exchange times up to 10 s [8]. In addition to the slow response time, this system could not cycle quickly between reagents due to the limitations of the syringe pumps. Samira Moorjani, also a former Shear group member, developed a system of reorienting flow directions within the microfluidic dosing chamber. This allowed for sub-second changes to the direction of the reagent stream [9]. Although this technique could effectively start and stop cell dosing, the system was unable to quickly cycle through different reagents while dosing a cell.

This chapter describes a technique for cycling between reagents with millisecond exchange times. This technique is designed to be applied in conjunction with a previously developed microfluidic dosing platform (Chapter 2), so that gradients may be applied with sub-cellular spatial resolution and millisecond temporal resolution.

5.2 EXPERIMENTAL METHODS

5.2.1 Chemicals and Reagents

Methylene blue (M9140) and N-Formyl-Met-Leu-Phe (fMLP, F3506) were purchased from Sigma-Aldrich (St. Louis, MO). Poly(dimethylsiloxane) and curing agent (RTV615A, RTV615B) were purchased from GE Advanced Materials (Niskayuna, NY). Human plasma fibronectin (341635) was purchased from Calbiochem (San Diego, CA).

5.2.2 Device

The cell dosing device was assembled as described in Chapter 2, with the addition of a Y-junction formed from PDMS that was placed upstream of the reagent reservoir chamber. Poly(dimethylsiloxane) was cured from a solution of 10:1 (w/w) polymer to curing agent. After inversion mixing, the solution was degassed, poured over the master, and cured at 60 °C for 1 hour. The Y-junction master was created from 0.9 mm diameter polyurethane coated aluminum wire glued to a polystyrene Petri dish.

When two reagents were pumped into the device from syringes driven by electromechanical pumps (Braintree Scientific, BS-9000) a stable boundary was formed and maintained due to laminar flow (Figure 5.1). The boundary was maintained in both the platinum-cured silicone tubing (Cole-Parmer, 95802-01) and cell dosing chamber (Grace Bio-Laboratories, 440889B), as laminar flow was unperturbed throughout the device. The boundary position was externally controlled by a DC motor driven by a 6 V power supply (Figure 5.2). A pulse-width modulation circuit (K166A; Carl's Electronics; Oakland, CA) mediated the power and directionality supplied to the motor, as determined by a custom designed LabView (National Instruments; Austin, TX) virtual instrument program. This allowed the user to specify the motor speed, direction, and resting timing in order to create a variety of dosing patterns.

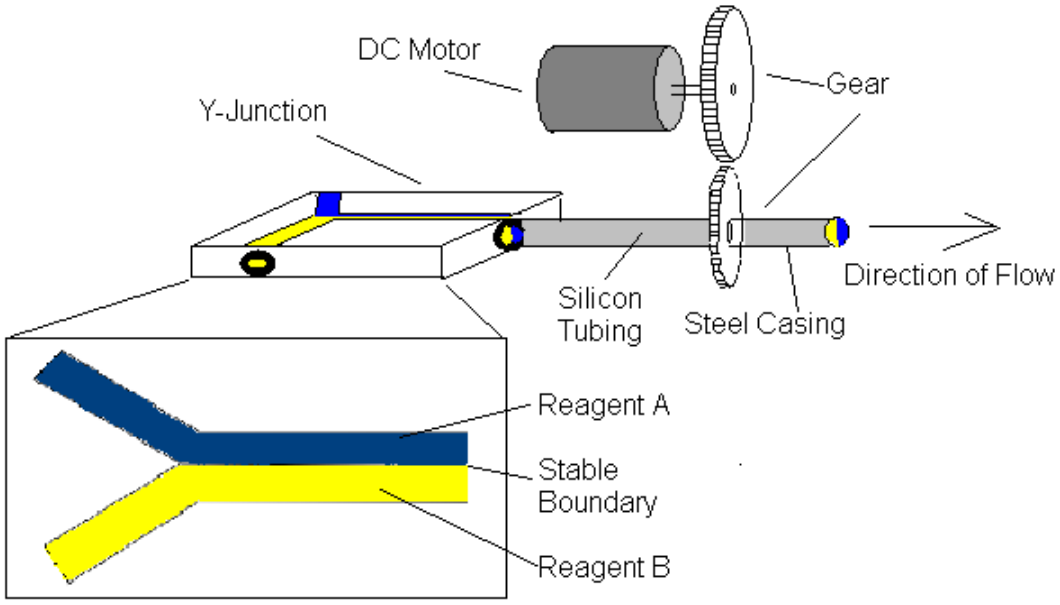

Figure 5.1 Reagent switching device. The reagent switching device was created from a PDMS Y-junction that established a stable boundary between two reagents. Silicon tubing threaded through steel casing provided a means for rotational control over the tubing during flow. A DC motor and set of gears allowed the tubing to be controlled remotely and automatically with LabView software.

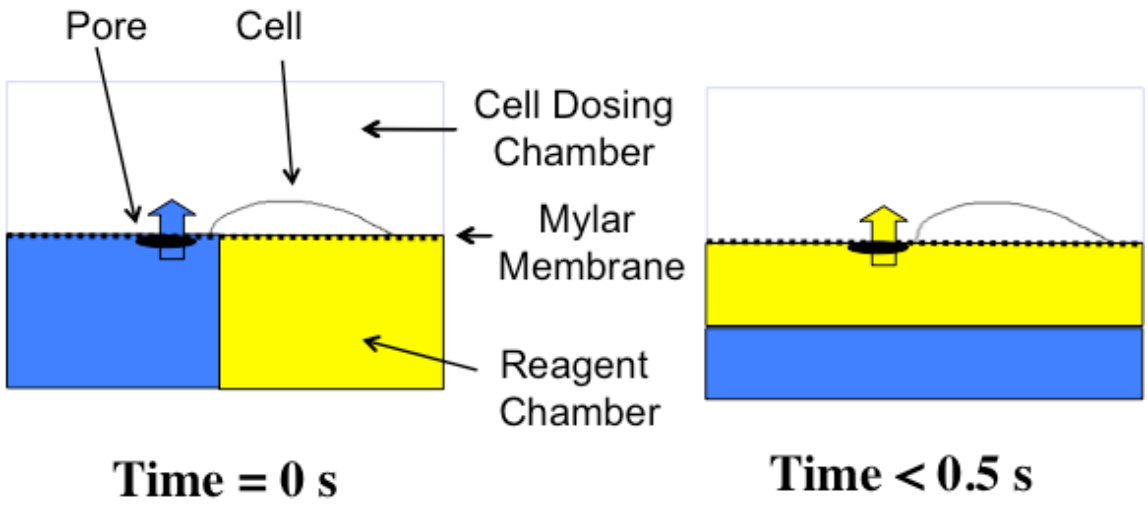

Figure 5.2: Reagent switching illustration. The orientation of the reagent determines whether reagent A (blue) or reagent B (yellow) enters the cell dosing chamber and bathes a cultured cell via an ablated pore. The orientation, and by extension the reagent dosing the cell, can be changed from A to B in less than 0.5 seconds.

5.2.3 Cell Culture

HL-60 cells were cultured in RPMI-1640 media (22400) supplemented with 10% (v/v) fetal bovine serum (FBS, 10082), both purchased from Invitrogen. Flasks were maintained at 37 °C in a 5% CO_2 atmosphere and diluted 1:10 in fresh media once per week. HL-60 cells are not adherent to polystyrene flasks and have a doubling time of 36-48 hours. All HL-60 cells used in this dissertation were provided by Dr. O. D. Weiner (Department of Biochemistry, University of California at San Francisco).

For cell dosing experiments, HL-60 cells were incubated in 1.3% (v/v) dimethylsulfoxide (DMSO) for 3-4 days to induce differentiation into a neutrophil-like

state. Several hours before cell dosing, the differentiated cells were centrifuged and resuspended in Gey's medium (6 mM KCl, 138 mM NaCl, 5 mM glucose, 1 mM Na_2HPO_4, 20 mM HEPES, 1 mM $MgCl_2$ and 1 mM $CaCl_2$, pH 7.4). The cells were plated within the flow chamber at a density of ~1 x 10^6 cells/mL and incubated for 30 minutes prior to the flow of reagents into the chamber. The flow chamber was mounted on acid-washed glass treated with 0.1 mg/mL fibronectin in Dulbecco's phosphate-buffered saline for 1.5 hours. The flow chamber was equilibrated with Gey's medium before cell plating.

5.2.4 Stream Creation and Imaging

Pores were created using focused light from a frequency-doubled (532 nm), microchip Q-switched Nd:YAG laser with a pulse width of ~600 ps and repetition rate of 7.65 kHz. The laser output was attenuated with a half-wave plate and polarizing beam splitter to 10 - 20 mW at the back aperture of a 20x, 0.5 NA objective in a Zeiss Axiovert inverted microscope. Each pore was created with a pulse train of 10 exposure periods of 10 ms in length (~77 pulses) with a 50 ms delay between pulses controlled by a Uniblitz UHS1 shutter (Vincent Associates, VMMT1).

Wide-field fluorescence images were acquired using a Zeiss Axiovert 135 inverted microscope and Hamamatsu Orca II charge-coupled device (CCD) camera (C4742-98) controlled by MetaMorph imaging software (Molecular Devices) using a Zeiss 20x, 0.5 NA objective or Zeiss 5x, 0.12 NA objective. Switching events were acquired with a Sony CCD Video Camera (XC-73) at a 1/125 s shutter speed.

5.3 Results and Discussion

In order to dose cells with multiple reagents and to achieve switching times of less than one second, a novel reagent switching device was created. In combination with the cell dosing platform, effector streams can be localized to arbitrary positions in culture

environments using laser-mediated ablation of polymer films. A lateral adjustment to the boundary position resulted in a change in reagent composition entering a pore, and thus a change in the reagent dosing a cell cultured on the polymer film downstream of the pore (Figure 5.2).

In order to determine the effectiveness of the system, HL-60 cells were dosed with a two-reagent boundary after plating within a microfluidic flow chamber. Only a single chamber was used for this demonstration, therefore no pore ablation was necessary. A solution containing a bacterially derived peptide known to induce neutrophil migration (100 nM fMLP) was flowed into a single dosing chamber to induce migration of differentiated HL-60 cells. A second solution of 1 mM methylene blue and Gey's medium was flowed into the Y-junction and delivered in parallel into the device. This format allowed the user to specify the placement of the boundary between the two solutions, and therefore the position of the chemotactic fMLP gradient (Figure 5.3). After ten minutes of exposure to this gradient, an HL-60 cell migrated towards the stream containing fMLP, while cells within a stream of 100 nM fMLP did not appear to migrate in any direction.

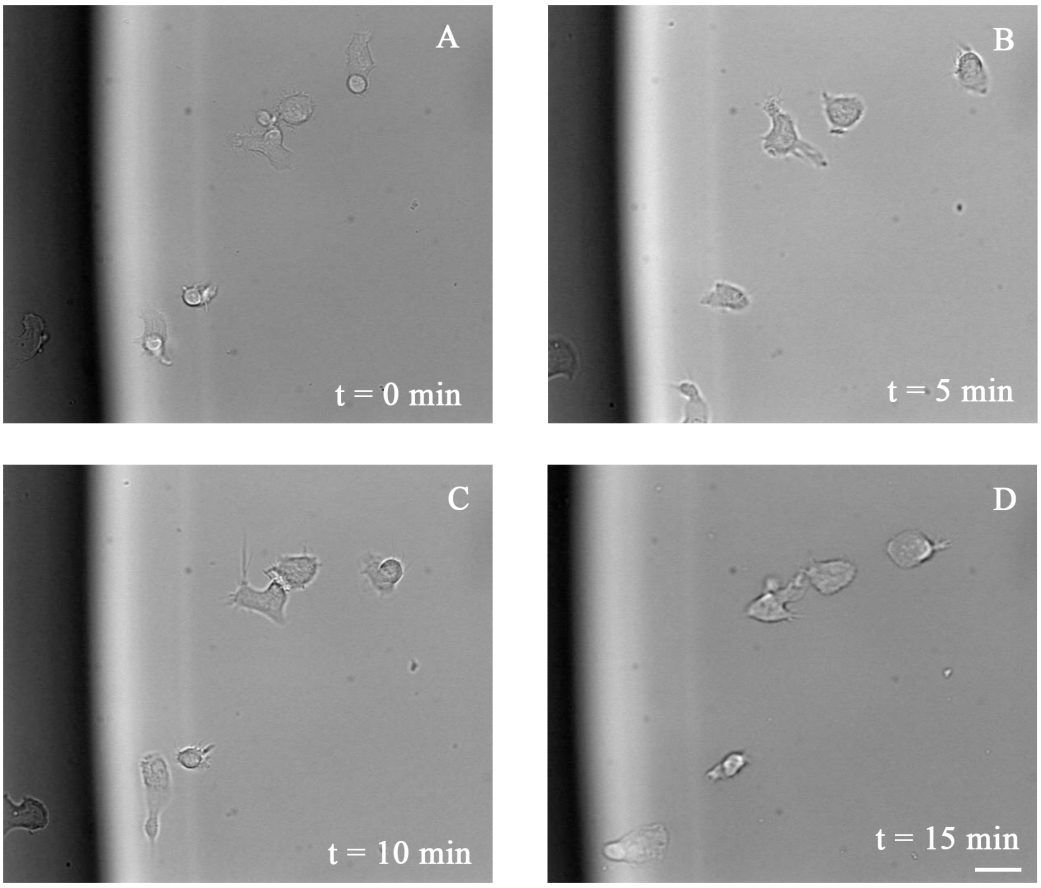

Figure 5.3: Reagent boundary control for dosing HL-60 cells. HL-60 cells were plated on glass treated with fibronectin in a flow chamber. (a) A stream of 1 mM methylene blue Gey's medium (left, dark stream) and 100 nM fMLP Gey's medium (right) were delivered confluently into a flow chamber. (b) After five minutes a gradient of fMLP appeared to induce pseudopod formation in a cell in the lower left corner of the image. (c) After ten minutes one cell begins to migrate toward the boundary in the direction of greater fMLP concentration. (d) After fifteen minutes the HL-60 cell has migrated completely to the region of greatest fMLP concentration. A scale bar equal to 25 μm applies to all images.

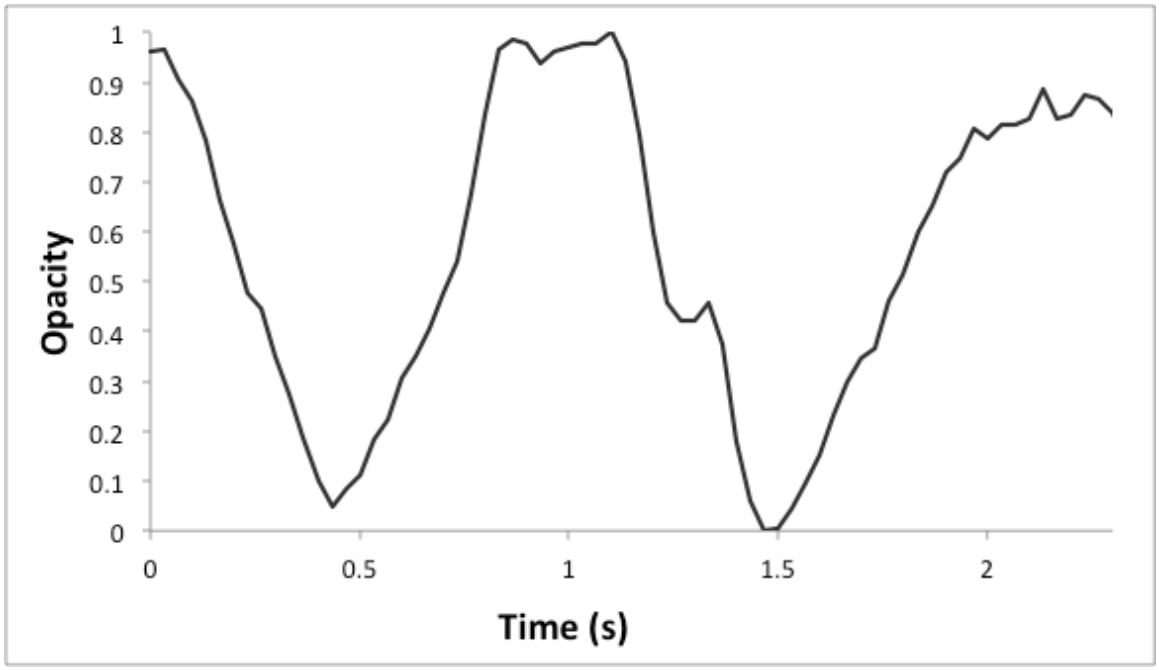

Figure 5.4: Sine wave reagent switching. A temporal sine wave of methylene blue and deionized water was created using the reagent switching system. The signal at a single location within the flow chamber is displayed over a time course. The signal was normalized to a maximum value within the flow chamber and background signal was subtracted.

Using automated control software, average switching times of 348 ms were achieved reproducibly, with a standard deviation of 38 ms (n = 11). The switching speed and period of the dosing pattern can be adjusted to achieve desired dosing parameters. For example, a sine wave was achieved with a period of 982 ms and a period standard deviation of 97 ms (Figure 5.4). These data were obtained from bright field images captured by CCD video at 30 frames per second.

By switching the reagent orientation, the cell can experience a temporal gradient dependent on the switching speed. The reagent switching speed was determined to be a

function of the voltage supplied to the DC motor. By increasing the voltage supplied, the switching speed increased (Figure 5.5).

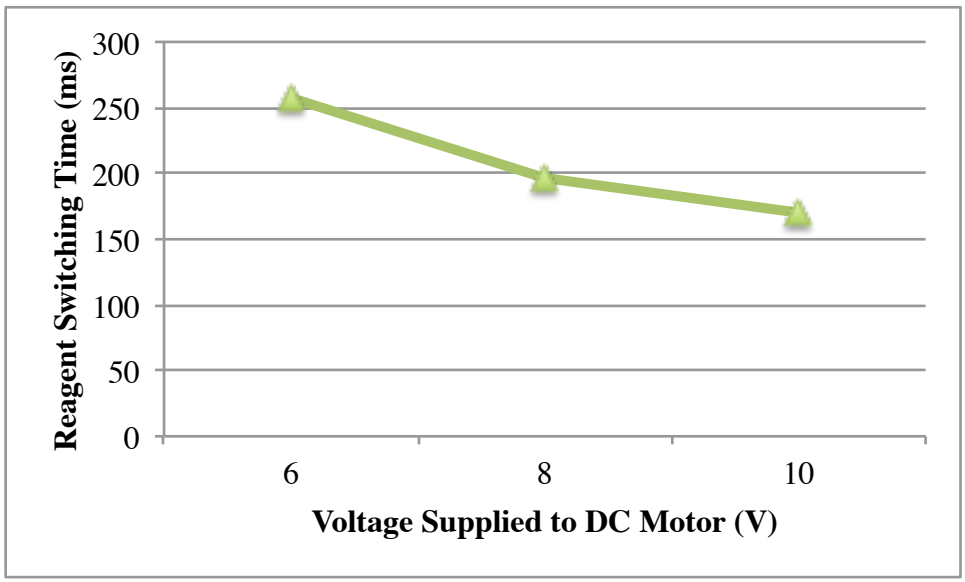

Figure 5.5: Effect of motor voltage on reagent switching time. Increasing the voltage supplied to the DC motor resulted in faster switching of reagents. The reagent switching time was measured as one half of a full cycle obtained by rotating the tubing 360 degrees about its axis.

5.4 Conclusion

This chapter describes a reagent switching technique capable of creating time-varying gradients with cycling times below one second. In combination with a microfluidic cell dosing platform (Chapter 2), this fast reagent switching technique can maintain reagent gradients with sub-cellular resolution and sustain the gradients for hours. This technique could be applied to the study of chemotaxis in a neutrophil model cell line or the latency of synapses in neurons.

This technique should prove useful in future studies of neutrophil chemotaxis and migration mechanisms. Using the model neutrophil cell line HL-60, temporal

characteristic of chemotaxis such as pseudopod formation and cell spreading can be analyzed. This device could illuminate whether these processes are affected by subsecond changes in their micro-environment. Additionally, this technique may be useful in studying a range of human cell types, including mechanisms of axonal pathfinding in neuronal cell lines.

Several components of this system could be modified or upgraded to improve performance. For example, to reduce switching times and variability, a high precision servomotor could be incorporated into the mechanical design in place of the DC motor. Alternatively, solenoids with fast response times could be used to valve streams before the Y-junction in order to control the reagent flow rates and achieve faster reagent exchange times.

5.5 REFERENCES

1. Alberts, B. *et al*. *Essential Cell Biology, Fourth Edition*. (Garland Science, 2013).
2. Nauen, D. W. & Bi, G.-Q. Measuring action potential-evoked transmission at individual synaptic contacts. *Journal Neural Engineering* **9**, 036014 (2012).
3. Weiner, O. D. *et al*. Spatial control of actin polymerization during neutrophil chemotaxis. *Nature Cell Biology* **1**, 75–81 (1999).
4. Matthews, H. R. A rotary solution changer for effecting multiple solution changes on isolated cells. *Medical Biology* **14**, 2396–2397 (1994).
5. Spitzer, K. W. & Bridge, J. H. A simple device for rapidly exchanging solution surrounding a single cardiac cell. *American Journal Physiology* **256**, C441–C447 (1989).
6. Dahan, E., Bize, V., Lehnert, T., Horisberger, J.-D. & Gijs, M. A. M. Rapid fluidic exchange microsystem for recording of fast ion channel kinetics in Xenopus oocytes. *Lab on a Chip* **8**, 1809 (2008).
7. Yamada, A., Katanosaka, Y., Mohri, S. & Naruse, K. A rapid microfluidic switching system for analysis at the single cellular level. *NanoBioscience, IEEE Transactions on* **8**, 306–311 (2009).

8. Hoppe, T. J., Moorjani, S. G. & Shear, J. B. Generating Arbitrary Chemical Patterns for Multi-Point Dosing of Single Cells. *Analytical chemistry* (2013).

9. Moorjani, S., Nielson, R., Chang, X. A. & Shear, J. B. Dynamic remodeling of subcellular chemical gradients using a multi-directional flow device. *Lab on a Chip* **10**, 2139–2146 (2010).

Bibliography

Agresti, J. J. *et al*. Ultrahigh-throughput screening in drop-based microfluidics for directed evolution. *Proc. Natl. Acad. Sci.* **107**, 4004–4009 (2010).

Alberts, B. *et al*. *Essential Cell Biology, Fourth Edition*. (Garland Science, 2013).

Ateya, D. A. *et al*. The good, the bad, and the tiny: a review of microflow cytometry. *Anal. Bioanal. Chem.* **391**, 1485–1498 (2008).

Atkinson-Leadbeater, K. *et al*. Dynamic expression of axon guidance cues required for optic tract development is controlled by fibroblast growth factor signaling. *J. Neurosci.* **30**, 685–693 (2010).

Bajpai, A. K., Shukla, S. K., Bhanu, S. & Kankane, S. Responsive polymers in controlled drug delivery. *Prog. Polym. Sci.* **33**, 1088–1118 (2008).

Baron-Van Evercooren, A., Kleinman, H. K., Seppä, H. E., Rentier, B. & Dubois-Dalcq, M. Fibronectin promotes rat Schwann cell growth and motility. *J. Cell Biol.* **93**, 211–216 (1982).

Beebe, D. J. *et al*. Functional hydrogel structures for autonomous flow control inside microfluidic channels. *Nature* **404**, 588–590 (2000).

Bloembergen, N. Laser-induced electric breakdown in solids. *Quantum Electron. IEEE J. Of* **10**, 375–386 (1974).

Boyan, B. D., Hummert, T. W., Dean, D. D. & Schwartz, Z. Role of material surfaces in regulating bone and cartilage cell response. *Biomaterials* **17**, 137–146 (1996).

Boyer, C., Schikorski, T. & Stevens, C. F. Comparison of Hippocampal Dendritic Spines in Culture and in Brain. *J. Neurosci.* **18**, 5294–5300 (1998).

Celedon, A. *et al*. A distinctive role for focal adhesion proteins in three-dimensional cell motility. *Nat. Cell Biol.* **12**, 598+ (2010).

Chaudhari, A. *et al*. Formation of sub-7 nm feature size PS-b-P4VP block copolymer structures by solvent vapour process. in *SPIE Adv. Lithogr.* 905110–905110 (International Society for Optics and Photonics, 2014).

Cheng, H. H., Huang, D.-S. & Lin, M.-T. Heat dissipation design and analysis of high power LED array using the finite element method. *Microelectron. Reliab.* **52**, 905–911 (2012).

Cherry, R. J., Cogoli, A., Oppliger, M., Schneider, G. & Semenza, G. A spectroscopic technique for measuring slow rotational diffusion of macromolecules. 1: Preparation and properties of a triplet probe. *Biochemistry (Mosc.)* **15**, 3653–3656 (1976).

Choi, N. W. *et al*. Microfluidic scaffolds for tissue engineering. *Nat. Mater.* **6**, 908–915 (2007).

Connell, J. L. Characterization and microfabrication of environmentally sensitive materials for studying bacterial group behaviors. (2012).

Connell, J. L. *et al*. Probing prokaryotic social behaviors with bacterial 'lobster traps'. *MBio* **1**, e00202–10 (2010).

Connell, J. L., Ritschdorff, E. T., Whiteley, M. & Shear, J. B. 3D printing of microscopic bacterial communities. *Proc. Natl. Acad. Sci.* (2013).

Coulomb, J.-L. A methodology for the determination of global electromechanical quantities from a finite element analysis and its application to the evaluation of magnetic forces, torques and stiffness. *IEEE Trans. Magn.* **19**, 2514–2519 (1983).

Cukierman, E., Pankov, R., Stevens, D. R. & Yamada, K. M. Taking Cell-Matrix Adhesions to the Third Dimension. *Science* **294**, 1708–1712 (2001).

Cunliffe, D. *et al*. Bacterial adsorption to thermoresponsive polymer surfaces. *Biotechnol. Lett.* **22**, 141–145 (2000).

Dahan, E., Bize, V., Lehnert, T., Horisberger, J.-D. & Gijs, M. A. M. Rapid fluidic exchange microsystem for recording of fast ion channel kinetics in Xenopus oocytes. *Lab. Chip* **8**, 1809 (2008).

Denk, W. *et al*. Anatomical and functional imaging of neurons using 2-photon laser scanning microscopy. *J. Neurosci. Methods* **54**, 151–162 (1994).

Denk, W. Two-photon scanning photochemical microscopy: mapping ligand-gated ion channel distributions. *Proc. Natl. Acad. Sci.* **91**, 6629–6633 (1994).

Digenis, G. A., Gold, T. B. & Shah, V. P. Cross-linking of gelatin capsules and its relevance to their in vitro-in vivo performance. *J. Pharm. Sci.* **83**, 915–921 (1994).

Dobell, C. *Antony van Leeuwenhoek and his 'Little animals'; being some account of the father of protozoology and bacteriology and his multifarious discoveries in these disciplines*. (Harcourt, Brace and company, 1932).

Dong, L., Agarwal, A. K., Beebe, D. J. & Jiang, H. Adaptive liquid microlenses activated by stimuli-responsive hydrogels. *Nature* **442**, 551–554 (2006).

Erlanger, B. F., Borek, F., Beiser, S. M. & Lieberman, S. Steroid-protein conjugates I. Preparation and characterization of conjugates of bovine serum albumin with testosterone and with cortisone. *J. Biol. Chem.* **228**, 713–728 (1957).

Fairbanks, B. D., Schwartz, M. P., Bowman, C. N. & Anseth, K. S. Photoinitiated polymerization of PEG-diacrylate with lithium phenyl-2,4,6-trimethylbenzoylphosphinate: polymerization rate and cytocompatibility. *Biomaterials* **30**, 6702–6707 (2009).

Galambos, P. & Forster, F. K. in *Micro Total Anal. Syst.* (Harrison, D. J. & Berg, A. van den) 189–192 (Springer Netherlands, 1998).

Gao, D. *et al.* Investigation on the pH-dependent binding of Eosin Y and bovine serum albumin by spectral methods. *J. Lumin.* **127**, 515–522 (2007).

Ge, S., Kojio, K., Takahara, A. & Kajiyama, T. Bovine serum albumin adsorption onto immobilized organotrichlorosilane surface: influence of the phase separation on protein adsorption patterns. *J. Biomater. Sci. Polym. Ed.* **9**, 131–150 (1998).

Gerlach, G. & Arndt, K.-F. *Hydrogel Sensors and Actuators: Engineering and Technology*. (Springer Science & Business Media, 2009).

Gómez-Moutón, C. *et al.* Dynamic redistribution of raft domains as an organizing platform for signaling during cell chemotaxis. *J. Cell Biol.* **164**, 759–768 (2004).

Goranovic, G. *et al.* Three-dimensional single step flow sheathing in micro cell sorters. in *Model. Simul. Microsyst.* (2001).

Gucker, F. T., O'Konski, C. T., Pickard, H. B. & Pitts, J. N. A Photoelectronic Counter for Colloidal Particles1. *J. Am. Chem. Soc.* **69**, 2422–2431 (1947).

Hermanson, G. T. *Bioconjugate Techniques*. (Academic Press, 2013).

Hogg, J. *The microscope: its history, construction, and applications*. (Illustrated London Library, 1854).

Hoppe, T. J. Laser-Based Techniques for Manipulating the Single-Cell Environment. (2013).

Hoppe, T. J., Moorjani, S. G. & Shear, J. B. Generating Arbitrary Chemical Patterns for Multi-Point Dosing of Single Cells. *Anal. Chem.* (2013).

Horio, M. *et al.* Apoptosis induced by hypertonicity in Madin Darley canine kidney cells: protective effect of betaine. *Nephrol. Dial. Transplant.* **16**, 483–490 (2001).

Huang, B. X., Kim, H.-Y. & Dass, C. Probing three-dimensional structure of bovine serum albumin by chemical cross-linking and mass spectrometry. *J. Am. Soc. Mass Spectrom.* **15**, 1237–1247 (2004).

Huxley, H. E. Electron microscope studies on the structure of natural and synthetic protein filaments from striated muscle. *J. Mol. Biol.* **7**, 281–IN30 (1963).

Ingber, D. E. Mechanical signaling and the cellular response to extracellular matrix in angiogenesis and cardiovascular physiology. *Circ. Res.* **91**, 877–887 (2002).

Jackson, M. J. *Microfabrication and Nanomanufacturing*. (CRC Press, 2005).

Li Jeon, N. *et al.* Neutrophil chemotaxis in linear and complex gradients of interleukin-8 formed in a microfabricated device. *Nat. Biotechnol.* **20**, 826–830 (2002).

Jeong, W. *et al*. Hydrodynamic microfabrication via 'on the fly' photopolymerization of microscale fibers and tubes. *Lab. Chip* **4**, 576 (2004).

Jhaveri, S. J. *et al*. Direct Three-Dimensional Microfabrication of Hydrogels via Two-Photon Lithography in Aqueous Solution. *Chem. Mater.* **21**, 2003–2006 (2009).

Jiang, L. & Erickson, D. Light-Governed Capillary Flow in Microfluidic Systems. *Small* **9**, 107–114 (2013).

Juncker, D., Schmid, H. & Delamarche, E. Multipurpose microfluidic probe. *Nat. Mater.* **4**, 622–628 (2005).

Kaehr, B. *et al*. Direct-write fabrication of functional protein matrixes using a low-cost Q-switched laser. *Anal. Chem.* **78**, 3198–3202 (2006).

Kaehr, B., Allen, R., Javier, D. J., Currie, J. & Shear, J. B. Guiding neuronal development with in situ microfabrication. *Proc. Natl. Acad. Sci. U. S. A.* **101**, 16104–16108 (2004).

Kaehr, B. & Shear, J. B. Multiphoton fabrication of chemically responsive protein hydrogels for microactuation. *Proc. Natl. Acad. Sci.* **105**, 8850–8854 (2008).

Kaiser, W. & Garrett, C. G. B. Two-Photon Excitation in CaF2: Eu2+. *Phys. Rev. Lett.* **7**, 229–231 (1961).

Kenis, P. J. A., Ismagilov, R. F. & Whitesides, G. M. Microfabrication inside capillaries using multiphase laminar flow patterning. *Science* **285**, 83–85 (1999).

Kim, P. *et al*. Soft lithography for microfluidics: a review. (2008).

Klauke, N., Smith, G. & Cooper, J. M. Microfluidic systems to examine intercellular coupling of pairs of cardiac myocytes. *Lab. Chip* **7**, 731–739 (2007).

Kleitman, N., Wood, P. M. & Bunge, R. P. Tissue culture methods for the study of myelination. *Cult. Nerve Cells* 337–377 (1991).

Kratchmarova, I., Blagoev, B., Haack-Sorensen, M., Kassem, M. & Mann, M. Mechanism of Divergent Growth Factor Effects in Mesenchymal Stem Cell Differentiation. *Science* **308**, 1472–1477 (2005).

Kumar, A. *et al*. CXCR4 Physically Associates with the T Cell Receptor to Signal in T Cells. *Immunity* **25**, 213–224 (2006).

Lee, G.-B., Chang, C.-C., Huang, S.-B. & Yang, R.-J. The hydrodynamic focusing effect inside rectangular microchannels. *J. Micromechanics Microengineering* **16**, 1024 (2006).

Lin, S. C., Yen, P. W., Peng, C. C. & Tung, Y. C. Single channel layer, single sheath-flow inlet microfluidic flow cytometer with three-dimensional hydrodynamic focusing. *Lab. Chip* (2012).

Mamada, A., Tanaka, T., Kungwatchakun, D. & Irie, M. Photoinduced phase transition of gels. *Macromolecules* **23**, 1517–1519 (1990).

Manz, A. *et al*. Design of an open-tubular column liquid chromatograph using silicon chip technology. *Sens. Actuators B Chem.* **1**, 249–255 (1990).

Manz, A., Graber, N. & Widmer, H. Miniaturized total chemical analysis systems: a novel concept for chemical sensing. *Sens. Actuators B Chem.* **1**, 244–248 (1990).

Martin, M. M. & Lindqvist, L. The pH dependence of fluorescein fluorescence. *J. Lumin.* **10**, 381–390 (1975).

Matthews, H. R. A rotary solution changer for effecting multiple solution changes on isolated cells. *Med Biol* **14**, 2396–2397 (1994).

Moorjani, S., Nielson, R., Chang, X. A. & Shear, J. B. Dynamic remodeling of subcellular chemical gradients using a multi-directional flow device. *Lab Chip* **10**, 2139–2146 (2010).

Nauen, D. W. & Bi, G.-Q. Measuring action potential-evoked transmission at individual synaptic contacts. *J. Neural Eng.* **9**, 036014 (2012).

Nguyen, N.-T. *Fundamentals and applications of microfluidics*. (Artech House, 2002).

Nguyen, N.-T., Huang, X. & Chuan, T. K. MEMS-micropumps: a review. *J. Fluids Eng.* **124**, 384–392 (2002).

Nielson, R., Kaehr, B. & Shear, J. B. Microreplication and Design of Biological Architectures Using Dynamic-Mask Multiphoton Lithography. *Small* **5**, 120–125 (2009).

Nielson, R. & Shear, J. B. Parallel chemical dosing of subcellular targets. *Anal. Chem.* **78**, 5987–5993 (2006).

Peret, B. J. & Murphy, W. L. Controllable soluble protein concentration gradients in hydrogel networks. *Adv. Funct. Mater.* **18**, 3410–3417 (2008).

Petersen, K. E. Silicon as a mechanical material. *Proc. IEEE* **70**, 420–457 (1982).

Phipps, C. *Laser Ablation and Its Applications*. (Springer, 2007).

Podczeck, F. & Jones, B. E. *Pharmaceutical Capsules*. (Pharmaceutical Press, 2004).

Pronko, P. P. *et al*. Avalanche ionization and dielectric breakdown in silicon with ultrafast laser pulses. *Phys. Rev. B* **58**, 2387 (1998).

Qin, D., Xia, Y. & Whitesides, G. M. Soft lithography for micro-and nanoscale patterning. *Nat. Protoc.* **5**, 491–502 (2010).

Ramamurty, G. *Applied Finite Element Analysis*. (I. K. International Pvt Ltd, 2010).

Sanchez-Freire, V., Ebert, A. D., Kalisky, T., Quake, S. R. & Wu, J. C. Microfluidic single-cell real-time PCR for comparative analysis of gene expression patterns. *Nat. Protoc.* **7**, 829–838 (2012).

Scheggi, A. M. V. *Biomedical Optical Instrumentation and Laser-Assisted Biotechnology*. (Springer Science & Business Media, 1996).

Schmaljohann, D. *et al.* Thermo-Responsive PNiPAAm-g-PEG Films for Controlled Cell Detachment. *Biomacromolecules* **4**, 1733–1739 (2003).

Schrieber, R. & Gareis, H. *Gelatine Handbook: Theory and Industrial Practice*. (John Wiley & Sons, 2007).

Seidlits, S. K., Schmidt, C. E. & Shear, J. B. High-Resolution Patterning of Hydrogels in Three Dimensions using Direct-Write Photofabrication for Cell Guidance. *Adv. Funct. Mater.* **19**, 3543–3551 (2009).

Shavezipur, M. *et al.* A finite element technique for accurate determination of interfacial adhesion force in MEMS using electrostatic actuation. *J. Micromechanics Microengineering* **21**, 115025 (2011).

Shirasaki, Y. *et al.* On-Chip Cell Sorting System Using Laser-Induced Heating of a Thermoreversible Gelation Polymer to Control Flow. *Anal. Chem.* **78**, 695–701 (2006).

Simonnet, C. & Groisman, A. Two-dimensional hydrodynamic focusing in a simple microfluidic device. *Appl. Phys. Lett.* **87**, 104–114 (2005).

Skoog, D., West, D., Holler, F. & Crouch, S. *Fundamentals of Analytical Chemistry*. (Cengage Learning, 2013).

Skovsen, E., Snyder, J. W., Lambert, J. D. C. & Ogilby, P. R. Lifetime and Diffusion of Singlet Oxygen in a Cell. *J. Phys. Chem. B* **109**, 8570–8573 (2005).

Soeller, C. & Cannell, M. B. Two-photon microscopy: imaging in scattering samples and three-dimensionally resolved flash photolysis. *Microsc. Res. Tech.* **47**, 182–195 (1999).

Somorjai, G. A. & Li, Y. *Introduction to Surface Chemistry and Catalysis*. (John Wiley & Sons, 2010).

Spikes, J. D., Shen, H.-R., Kopečková, P. & Kopeček, J. Photodynamic Crosslinking of Proteins. III. Kinetics of the FMN- and Rose Bengal-sensitized Photooxidation and Intermolecular Crosslinking of Model Tyrosine-containing N-(2-Hydroxypropyl)methacrylamide Copolymers. *Photochem. Photobiol.* **70**, 130–137 (1999).

Spitzer, K. W. & Bridge, J. H. A simple device for rapidly exchanging solution surrounding a single cardiac cell. *Am J Physiol* **256**, C441–C447 (1989).

Stone, H. A., Stroock, A. D. & Ajdari, A. Engineering flows in small devices: microfluidics toward a lab-on-a-chip. *Annu Rev Fluid Mech* **36**, 381–411 (2004).

Stone, H. A., Stroock, A. D. & Ajdari, A. Engineering flows in small devices: Microfluidics toward a lab-on-a-chip. *Annu Rev Fluid Mech* **36**, 381–411 (2004).

Stroock, A. D. & Whitesides, G. M. Components for integrated poly (dimethylsiloxane) microfluidic systems. *Electrophoresis* **23**, 3461–73 (2002).

Sugiura, S. *et al*. Photoresponsive polymer gel microvalves controlled by local light irradiation. *Sens. Actuators Phys.* **140**, 176–184 (2007).

Sun, S., Titushkin, I. & Cho, M. Regulation of mesenchymal stem cell adhesion and orientation in 3D collagen scaffold by electrical stimulus. *Bioelectrochemistry* **69**, 133–141 (2006).

Suri, S. & Schmidt, C. E. Cell-Laden Hydrogel Constructs of Hyaluronic Acid, Collagen, and Laminin for Neural Tissue Engineering. *Tissue Eng. Part A* **16**, 1703–1716 (2010).

Suzuki, A. & Tanaka, T. Phase transition in polymer gels induced by visible light. *Nature* **346**, 345–347 (1990).

Takayama, S. *et al*. Subcellular positioning of small molecules. *Nature* **411**, 1016 (2001).

Takayama, S. *et al*. Selective chemical treatment of cellular microdomains using multiple laminar streams. *Chem. Biol.* **10**, 123–130 (2003).

Takizawa, K., Moorman, C., Wright, S., Christopher, J. & Tezduyar, T. E. Wall shear stress calculations in space–time finite element computation of arterial fluid–structure interactions. *Comput. Mech.* **46**, 31–41 (2010).

Tibbitt, M. W. & Anseth, K. S. Hydrogels as extracellular matrix mimics for 3D cell culture. *Biotechnol. Bioeng.* **103**, 655–663 (2009).

Ugaz, V. M., Elms, R. D., Lo, R. C., Shaikh, F. A. & Burns, M. A. Microfabricated electrophoresis systems for DNA sequencing and genotyping applications: current technology and future directions. *Philos. Trans. R. Soc. Lond. Ser. Math. Phys. Eng. Sci.* **362**, 1105–1129 (2004).

Wallace, D. C. Mitochondrial DNA sequence variation in human evolution and disease. *Proc. Natl. Acad. Sci.* **91**, 8739–8746 (1994).

Wang, G. X. & Poo, M. Requirement of TRPC channels in netrin-1-induced chemotropic turning of nerve growth cones. *Nature* **434**, 898–904 (2005).

Weiner, O. D. *et al*. Spatial control of actin polymerization during neutrophil chemotaxis. *Nat. Cell Biol.* **1**, 75–81 (1999).

Weishaupt, K. R., Gomer, C. J. & Dougherty, T. J. Identification of singlet oxygen as the cytotoxic agent in photo-inactivation of a murine tumor. *Cancer Res*. **36**, 2326–2329 (1976).

Wolff, A. *et al*. Integrating advanced functionality in a microfabricated high-throughput fluorescent-activated cell sorter. *Lab*. *Chip* **3**, 22–27 (2003).

Yamada, A., Katanosaka, Y., Mohri, S. & Naruse, K. A rapid microfluidic switching system for analysis at the single cellular level. *NanoBioscience IEEE Trans*. *On* **8**, 306–311 (2009).

Yao, P., Schneider, G., Prather, D., Wetzel, E. & O'Brien, D. Fabrication of three-dimensional photonic crystals with multilayer photolithography. *Opt*. *Express* **13**, 2370–2376 (2005).

Youtsey, K. J. & Grossweiner, L. I. Optical Excitation of the Eosin-Human Serum Albumin Complex*. *Photochem*. *Photobiol*. **6**, 721–731 (1967).

Yu, Q., Bauer, J. M., Moore, J. S. & Beebe, D. J. Responsive biomimetic hydrogel valve for microfluidics. *Appl*. *Phys*. *Lett*. **78**, 2589 –2591 (2001).

Zarrin, F. & Dovichi, N. J. Sub-picoliter detection with the sheath flow cuvette. *Anal*. *Chem*. **57**, 2690–2692 (1985).

Zhuo, R.-X. & Li, W. Preparation and characterization of macroporous poly(N-isopropylacrylamide) hydrogels for the controlled release of proteins. *J*. *Polym*. *Sci*. *Part Polym*. *Chem*. **41**, 152–159 (2003).

Zienkiewicz, O. C. The Stress-Distribution in Gravity Dams. *J*. *ICE* **27**, 244–271 (1947).

Zienkiewicz, O. C. & Morice, P. B. *The finite element method in engineering science*. (McGraw-hill London, 1971).

COMSOL Multiphysics: Version 3.5a. *User's guide*. (Comsol, 2008).

Vita

Michael Mayes Robinson received his Bachelor of Science in Chemical Engineering in 2007 from the University of Virginia. In 2009 he enrolled in the Biomedical Engineering graduate program at the University of Texas at Austin. He earned a Master of Science in Biomedical Engineering in 2011.

Permanent address: Michael.Robinson@utexas.edu

This dissertation was typed by the author.